Solar Activation of Molecular Water Oxidation Catalysts Using Semiconductors

by

Benjamin M. Klepser

A dissertation submitted in partial fulfillment
of the requirements for the degree of
Doctor of Philosophy
(Chemistry)
in the University of Michigan
2015

Doctoral Committee
  Associate Professor Bart M. Bartlett
  Professor Melanie S. Sanford
  Associate Professor Nicolai Lehnert
  Associate Professor Kevin P. Pipe

To Amy Marie, you are my love and my rock.

Acknowledgements

I would like to acknowledge several individuals who have helped me reach the pinnacle of formal education. I am excited to continue my education through building on practical experiences in industry. First and foremost, I would like to acknowledge the dedication and support that my beautiful wife, Amy, has provided for the last five years. I cannot express how deeply thankful I am for your constant encouragement and understanding. I know that these past few years have been by no means easy, but I could not have reached this point without your love and patience through this season of our lives.

Second, I would not be here without the continuing love and support from my family. Mom and Dad, you have always been excellent examples of the person I want to be. I admire how hard you have worked throughout the years to always provide your children with every opportunity possible. It’s not always easy to see how the sacrifices you made many years ago have come to fruition, but I think this is a clear marker of the path you have helped me find. You are a great inspiration to your family and I am forever thankful for the blessing you are on my life. Jennifer, I see the passion that drives you to succeed as similar to mine. I know I have been hard on you in the past, but I am always on your team, and I will always do whatever it takes to help you achieve your dreams. Annamarie, Mark, and Daniel, I am so thankful to have you as a part of this adventure with Amy and I. Thank you for your encouragement and support for both Amy and I through this long and tiresome process. I look forward to the adventures we will all share in the next chapter of our lives.

Third, I would like to thank my educational mentors through the years. My passion for science stems directly from the passion you have displayed through teaching and mentoring. I would be remiss if I did not start by acknowledging John Boerkoel, John Christians, and Mark Vogel. Through your work with Science Olympiad, you fostered my burgeoning desire to understand the world through the lens of science. It was my education

from you that taught me to ask questions and seek truth.

Additionally, Carolyn Anderson, you pointed me in the direction of chemistry research. You not only taught me how to ask questions and helped my shape about my future goals, you taught me what questions to ask and taught me the basic skills for being a synthetic chemist. Your passion for God and chemistry is the reason I am a chemist today and many of our discussion have shaped the way I reconcile faith and science today.

I also want to acknowledge Bart Bartlett for his guidance and mentorship through the last five years. I thank you for all of the helpful suggestions and conversations that have lead me to this point. I am excited to see how your lab and research continues to grow in the coming years, and I will always appreciate the lessons I learned from you.

To my lab mates, I thank you for the comradery we have developed during my time with you all. I want to thank the lab members who have already moved on in their careers. Tanya, Xiaoguang, and Joe, you showed us the ropes in lab, and set the tone for building strong collaboration in our lab community. I thank you for all of your advice and encouragement throughout our time together. Emily, on top of contributing in the same way as Tanya, Xiaoguang, and Joe, you are a fantastic mentor, and I will always remember your willingness to teach me the first few years in lab. It is an honor to have worked so closely with you and our lab could not have survived without your constant support. Kayla, we have shared many experiences together in lab, and I thank you for always lending an empathetic ear and engaging in so many scientific discussions. Of course soccer has been a blast, and I will miss our team. Charles and Jimmy, thanks for always challenging my way of thinking about science and your contributions to our lab. Sam, Frances, and Adam thank you for your suggestions and ideas. You are all great friends, and I am blessed by the impact you have all made on Amy and I.

Lastly, I would like to thank the rest of my family and friends for your dedication and support during the last few years. You have all been very important in helping Amy and I enjoy our time in Ann Arbor. Thank you all for your roles in our lives. We’re excited to share many more adventures together.

Table of Contents

List of Schemes

List of Figures

List of Tables

List of Appendices

Abstract

Water splitting has been proposed as a viable route toward the renewable production of hydrogen. However, this approach is limited by the water oxidation half-reaction due to the large energy input needed the reaction is sluggish. Sunlight has been used to create excited state electron/hole pairs that are thermodynamically capable of generating H_2 and O_2. Molecular (homogeneous) and heterogeneous catalysts have been developed to oxidize water efficiently under illumination. The focus of this dissertation is to anchor molecular catalysts onto heterogeneous light absorbers (semiconductors) to more efficiently oxidize water using sunlight.

The most significant discovery is that when a molecular Fe water oxidation catalyst is anchored to WO_3, a 60% increase in the rate of oxygen evolution and a 40% increase in selectivity towards water oxidation is achieved. Additionally, when different tsemiconductors are used, the reaction rate is dependent on the energy of the conduction band edge and the band gap. For instance, when the conduction band potential energy is held constant and the band gap is decreased from 2.7 eV (WO_3) to 2.1 eV (Fe_2O_3) the rate enhancement with the Fe catalyst increases from 60% to 273%.

In addition to the role of the semiconductor on the photoelectrochemical performance, the molecular species also plays an important role in the photoelectrochemical rate enhancement. The most significant development using various molecular species is that replacing iron with other first-row transition metals (Mn-Zn) results in complexes that are only active toward water oxidation when anchored to WO_3. And, the corresponding nickel and copper complexes increase the selectivity towards water oxidation up to 99% compared to bare WO_3 (56%). Unfortunately, when the best-performing ruthenium catalyst is anchored to various semiconductors, the rate enhancement for solar water oxidation is negligible compared to the other molecular species used in this work.

This work demonstrates for the first time that photoelectrochemically generated minority carriers (holes) from semiconductors can be used directly as oxidants to activate molecular oxidation complexes under solar irradiation. Furthermore, this work is the first to quantify the increase in selectivity towards water oxidation directly for WO_3 when modified with molecular species.

Chapter 1

Introduction

1.1 A Case for Solar Energy Conversion

Energy availability in the form of electricity or transportation fuel is one of the most important challenges facing the growth of the global economy. Especially in developing regions of the world, electricity is a major source of conflict and often dictates regional access to clean water, food storage, health, and education, which are all major areas of concern for social justice and equality in developing countries. Fossil fuels offer a number of promising properties that enables the global economy to continually grow in the areas of energy distribution and transportation. However, fossil fuel distribution is still limited by its relative affordability (in developing regions) and poor transportation infrastructure to remote regions of developing countries.

With energy distribution being a major concern in developing countries, the expectation is that as the developing countries continue to grow, their demand on the global fuel economy will begin to substantially impact the cost and distribution worldwide. As such, numerous alternative energy sources are being targeted worldwide for many reasons. The major driving force for many countries is creating an energy independent state. It is often suggested in global economics that many international conflicts stem from countries seeking to secure affordable energy or protecting foreign investments. In addition to energy independence, another driving force is also to ensure social and environmental responsibility throughout the world.

Currently, energy consumption is roughly 20 TJ of energy per second (20 TW of power) worldwide.[1] It is predicted that by 2050 the global energy demand will almost triple (up to 50 TW). Based on current fossil fuel consumption and production, the amount of energy could feasibly be achieved, however, many are concerned about the environmental cost of this possible solution. Many cite the exponential increase in atmospheric CO_2

concentration that correlates to the onset of the industrial revolution where the consumption of fossil fuels became increasingly popular.[2] However, at the current rate of CO_2 production, the world will exceed the highest known CO_2 concentrations by an order of magnitude. Atmospheric CO_2 concentration has demonstrated close correlation with average global temperature. Increasing global temperatures would have devastating environmental impacts, but it's still very difficult to accurately model the true impacts on the environment.[3]

Solar energy conversion and storage are paramount to achieving energy independence, social equality, and environmental responsibility because the sun delivers enough power to the earth's surface (~120,000 TW) to meet all of the projected global energy demands (50 TW) even at very low conversion/storage efficiencies. Therefore, numerous technologies have been developed to efficiently store and convert solar energy to electrical or chemical energy.[4] The most common mode for solar energy conversion is converting solar energy directly to electricity using Si solar panels[5] or dye sanitized solar cells (DSSCs).[6] Both of these technologies exhibit excellent efficiencies and are generally affordable on household scales. There is some concern about material/energy cost associated with these technologies and the nature of energy production is limited to daytime production, but recent expansions in production capabilities and processes and increasing demand have pushed the costs down to all-time lows.[7]

Particularly in response to the diurnal nature of solar irradiation on the solar cells, it is paramount to store or convert the energy for use during periods of little/no illumination. Again, many solutions have been proposed for this purpose. Two of the more common solutions are energy storage through the use of high capacity batteries[8] or through chemical fuel formation.[9] Both of these methods have various impacts on the energy economy throughout the world. For instance, batteries have high impact for the storage of electricity, but they often lack the high energy density associated with powering transportation vehicles compared to combustible fuels.[8] In addition to energy storage materials, chemical fuels offer better transportability and often high energy densities. But, the chemical fuels are often more difficult to prepare since they possess higher energy densities and often require mechanistically complex chemical reactions.

In relation to solar energy conversion into chemical bonds, many strategies have been developed to create high energy fuels to convert solar energy including biomass conversion, photovoltaic electrolysis, and solar water splitting.[9] Although all of these strategies will be utilized for solar energy conversion, solar water splitting offers the promise of abundant resources, more direct processes, and higher theoretical efficiencies. In addition to chemical fuel formation through the production of hydrogen, hydrogen currently has numerous alternative applications such as metal-ore refinement, the Haber-Bosch process, the Fischer-Tropsch synthesis, and CO_2 sequestration (as a potential alternative fuel).

To adequately understand water splitting, the overall reaction can be separated into two electrochemical half reactions summarized in Equation 1.1. The amount of solar energy stored through splitting one mole of water is 237 kJ. However, particularly in the case of the water oxidation half reaction (**1**), there are additional kinetic limitations associated with each half reaction. Therefore, the potential required for the overall reaction is generally significantly higher than 237 kJ/mol.

$$\mathrm{H_2O} \rightarrow \frac{1}{2}\,\mathrm{O_2} + 2\,\mathrm{H^+} + 2\,\mathrm{e^-} \qquad \mathrm{E^{\circ}} = 1.23\ \mathrm{V} \qquad (\mathbf{1})$$

$$2\,\mathrm{H^+} + 2\,\mathrm{e^-} \rightarrow \mathrm{H_2} \qquad \mathrm{E^{\circ}} = 0.00\ \mathrm{V} \qquad (\mathbf{2})$$

$$\mathrm{H_2O} \rightarrow \frac{1}{2}\mathrm{O_2} + \mathrm{H_2} \qquad \mathrm{E^{\circ}} = -1.23\ \mathrm{V\ vs.\ RHE} \qquad \Delta\mathrm{G^{\circ}} = 237\,\frac{\mathrm{kJ}}{\mathrm{mol}} \qquad (\mathbf{3})$$

Equation 1.1 Half reactions for overall water splitting

Water oxidation presents specific challenges for solar water splitting because of the 4 e^-'s that must be transferred and the high kinetic barriers associated with 4 single electron transfer processes common for many metal catalysts.[10] In attempt to circumvent the limitations associated with solar water oxidation, numerous catalysts have been developed. Both heterogeneous and homogeneous photocatalysts catalysts have been explored for solar water oxidation and both offer pros and cons for more efficiently oxidizing water.

1.2 Solar Activation of Molecular Water Oxidation Catalysts

Alongside heterogeneous photocatalysts for water oxidation (e.g. semiconductors) numerous molecular water oxidation catalysts (WOCs) have been developed. Molecular water oxidation catalysts (WOCs) were first reported by Meyer and coworkers with the discovery of the so-called ruthenium "blue dimer."[11] The ruthenium blue dimer stood alone for many years as the only truly molecular water oxidation catalyst. Over the next 10 years, Elizarova and co-workers reported several water oxidation complexes, such as metallophthalocyanines (Cr-Co), cobalt and copper bipyridine, that have since been shown to decompose to simple heterogeneous catalysts under reaction conditions.[12,13] The next report of a new molecular WOC was a manganese dimer developed by Crabtree, Brudvig, and coworkers.[14] In this instance the manganese dimer requires an oxygen atom donor from the sacrificial oxidant in order to produce oxygen from water. To support this mechanistic proposal, ^{18}O isotope labeling experiments were used to probe the oxygen atom source for water oxidation.

Over the last several years, molecular WOCs have garnered renewed interest with the development of molecular catalysts capable of oxidizing water as fast as enzymes.[13,14,15] In addition to the fastest catalysts, there have been numerous ruthenium and iridium rare-earth catalysts developed for water oxidation. However, there has also been several examples of non-rare-earth iron[16,17], cobalt[18,19,20], and copper[13,21] WOCs. Molecular catalysts are attractive because they are easily modified[22] and reaction kinetics are measured straightforwardly.[23] However, many molecular water oxidation catalysts are not inherently photoactive.

In order to successfully oxidize water, molecular catalysts rely primarily on sacrificial oxidants.[11-21] Sacrificial, chemical oxidants (like $Ce(NH_4)_2(NO_3)_6$ (CAN) or

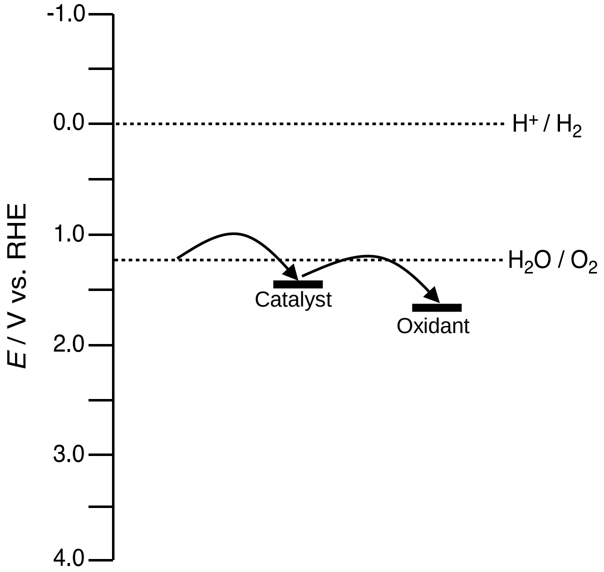

Figure 1.1 Electrochemical potential energy diagram of homogeneous catalysts compared to chemical sacrificial oxidants

$Na_2S_2O_8$) make the overall reaction thermodynamically favorable, as depicted in Figure 1.1. Electrochemical potential energy also serves as a sacrificial oxidant to make the reaction thermodynamically favorable.[13,21] In both cases, the molecular catalyst transfers electrons to the sacrificial oxidant instead of splitting water completely. Although these methods allow the different half-reactions to be probed independently, at some point the two half reactions must be reconnected, and solar energy provides the energy input necessary to couple the two water splitting half-reactions.

Since molecular WOCs are not inherently photoactive, three alternative strategies have been developed to achieve solar water oxidation. It should be noted that all of these strategies have pros and cons, and they are all important for further improving solar activation of molecular WOCs. The first strategy is a multi-component, solution-based approach towards solar activation of molecular catalysts. In this strategy, the freely diffusing molecular catalyst is in solution with a photosensitizer, such as ruthenium tris-bipyridine [$Ru(bipy)_3Cl_2$], and a sacrificial agent having $E° < 1.23$ V vs. RHE. This strategy relies upon fast electron transfer between each component in solution, and it uses the long excited-state lifetime of the photosensitizer under illumination to ensure electron transfer between the molecular WOC and the photosensitizer as well as between the photosensitizer to the sacrificial oxidant. The logical extension of this approach has resulted in the molecular catalyst being combined with the photosensitizer in supramolecular complexes that functions as the light absorber *and* the catalyst.

The other two approaches replace sacrificial chemical oxidants with semiconductor electrodes. In both cases, instead of transferring electrons to a chemical oxidant in solution, the electrons are transferred from a molecular species covalently attached to the surface of the semiconducting electrode. The stark contrast between the two strategies is the identity of the light absorber, which ultimately impacts the overall energy of electron transfer between the catalyst and the semiconductor. This difference will be highlighted in more detail in the corresponding section for each strategy.

1.2.1 Solution-based Molecular Photocatalysis

As mentioned above, the quickest strategy for photosensitizing molecular water oxidation catalysts involves addition of an electron transfer mediator that absorbs visible light. It will become evident throughout this discussion that the rate of electron transfer plays a pivotal role in determining the efficacy of each catalyst in the presence of the light absorbing agent. In this instance, the long lived state of the excited electron on the light absorbing molecule in solution is paramount for success. As such, ruthenium tris-bipyridyl $[Ru(bipy)_3X_2]$ complexes are most commonly used for this approach. $Ru(bipy)_3Cl_2$ is one of the most common light absorbing complexes.[24] Therefore, $Ru(bipy)_3Cl_2$'s excited state lifetimes and redox potentials are well known for catalytic purposes. Furthermore, the bipyridine can be readily modified to fine tune the electronic potentials for the highest occupied molecular orbital (HOMO) and the lowest unoccupied molecular orbital (LUMO). This design allows different catalysts to be used in order to oxidize molecular catalysts in solution. Furthermore, the excited-state electron is also capable of reducing other sacrificial oxidants in solution. A general scheme for the solution-based approach is summarized in Figure 1.2. In this instance, the electrons transfer from water to the catalyst (water oxidation) after the catalyst has been oxidized by the sensitizer ($Ru(bipy)_3Cl_2$) in solution. The sensitizer is able to accept electrons from the catalyst after excitation from the light source promotes an electron from the HOMO to the LUMO. The excited state electron then transfers to the terminal electron acceptor, which in many cases is $Na_2S_2O_8$. Unless otherwise noted, $Ru(bipy)_3X_2$ and $Na_2S_2O_8$ are the photosensitizer and sacrificial oxidant respectively for all reported systems.

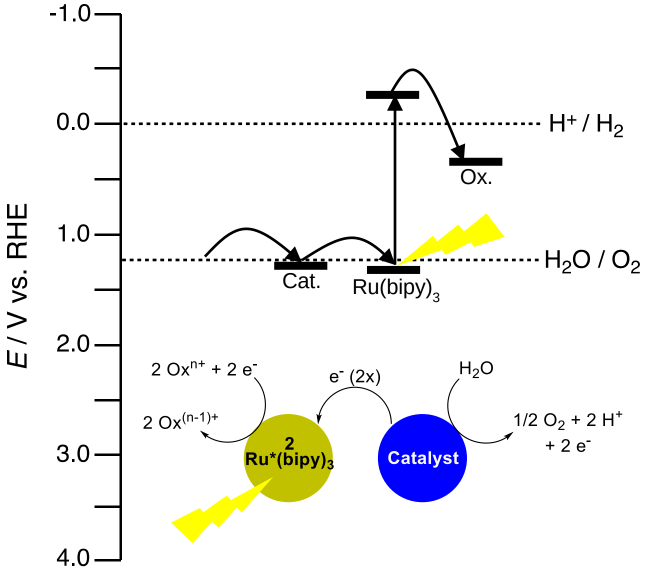

Figure 1.2 Electrochemical potential energies of solution-based photocatalyzed water oxidation

The application of this approach was reported shortly after the discovery of the ruthenium blue dimer from Meyer and co-workers[11] by Grätzel and co-workers in 1987.[25] In this instance, a modified ruthenium bis-bipyridyl oxo-bridged dimer (**1**), depicted in Scheme 1.1, was reported for solar water oxidation. The dark reaction with CAN yielded O_2 at an initial rate of 40 µL hr^{-1} in the presence of 0.2 µmol Ru-O-Ru. The stability of the corresponding complexes was indefinite in the presence of CAN, but when an equimolar mixture of $Co(SO_4)$ and $Co_2(SO_4)_3$ are added to the catalyst in solution they obtained up to 75 turnover for water oxidation without signs of degradation. Under illumination, using the photosensitizer Ru(4,4'-dicarbethoxy-2,2'-bipyrdine)$_3$Cl$_2$ the catalyst was indefinitely stable, and oxidized water with an initial rate of 330 µL h^{-1} per 1.5×10^{-5} M catalyst. The rate decreases after several minutes due to bleaching of the photosensitizer in solution.

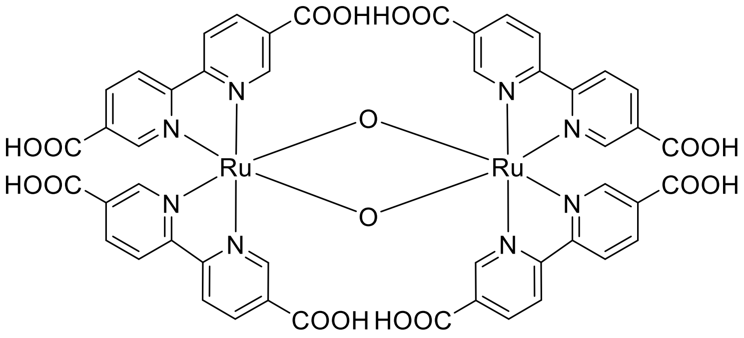

1

Scheme 1.1 Ruthenium catalyst first reported for solar water oxidation in solution

Solar water oxidation using molecular catalysts remained largely dormant until Cape and Hurst revisited the idea presented by Grätzel and co-workers in 2008.[26] In this report, the ruthenium blue dimer (**2**) was oxidized using Ru(bipy)$_3$Cl$_2$ as the solution-based photosensitizer with $Na_2S_2O_8$. The rate of water oxidation under illumination was not

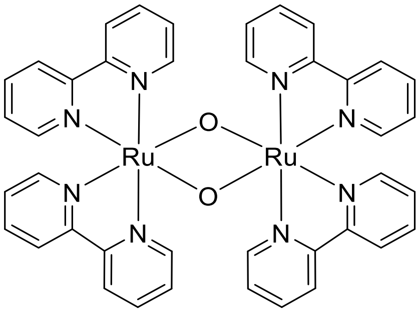

2

Scheme 1.2 Ruthenium "blue dimer" used for solar water oxidation in solution reported, but was “5-fold higher” when Ru(4,4’-dicarbethoxy-bipyridine)$_2$(bipy)Cl$_2$ was used as the photosensitizer. Because the reaction was run under neutral conditions, the catalyst exhibited higher stability relative to **2** under illumination. In addition to this report, it was demonstrated that the increase in rate observed in this system is due to Ru(bipy)$_3$Cl$_2$ acting partially as an electron transfer mediator between the catalyst and the sacrificial oxidant.[27]

A series of several other ruthenium catalysts have been reported for solar water oxidation using this approach.[28,29,30] The unifying thread between these complexes is the mononuclear (even though some possess multiple ruthenium centers) reactivity of each

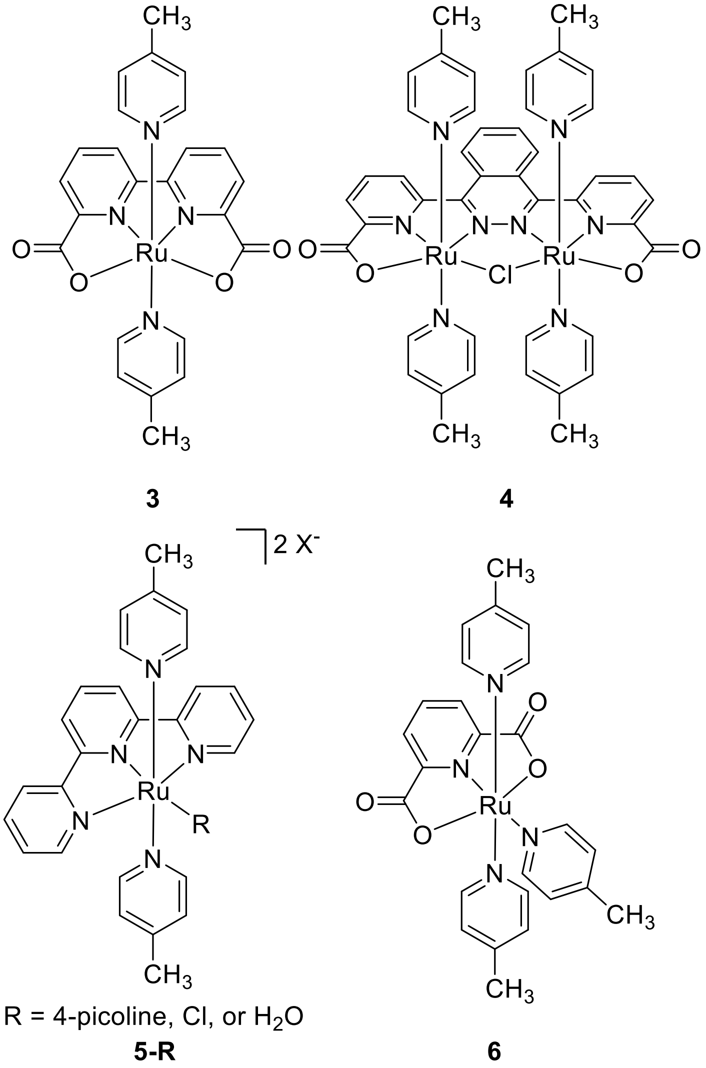

3

4

R = 4-picoline, Cl, or H_2O

5-R

6

Scheme 1.3 Ruthenium catalysts used for solar water oxidation in solution developed by Sun and co-workers catalyst as depicted in Scheme 1.3. The results of these various catalysts are summarized in Table 1.1. These reports highlight the importance of aligning the catalysts electrocatalytic onset with the redox potential of the photosensitizer since similar complexes outside the appropriate potential regions are inactive under illumination. Furthermore, it goes to show the excellent reactivity and stability of molecular ruthenium catalysts towards water oxidation.

Catalyst	**TON (mol O_2 mol^{-1} cat)**	**TOF (mol O_2 mol^{-1} cat s^{-1})**
4	580	0.83
5-picoline	2	0.0006[a]
5-Cl	43	0.03[a]
5-H_2O	84	0.1[a]
6	62	0.05[a]

Table 1.1 Solar water oxidation using ruthenium catalysts reported by Sun and co-workers; [a] TOF estimated by the initial slope of oxygen evolution from data provided in original report

In addition to ruthenium containing catalysts, the only other truly molecular complex that has demonstrated solar water oxidation with a solution-based photosensitizer is the Fe(TAML)(H_2O) complexes reported by Panda et al. as depicted in Scheme 1.4.[31] Fe(TAML) is the fastest first-row transition metal catalyst reported to date with a turnover frequency of 1.3 mol O_2 mol^{-1} catalyst s^{-1}.[16] However, the catalyst exhibits poor stability (13 mol O_2 mol^{-1} catalyst) under dark reaction conditions using CAN as the sacrificial oxidant. Under visible light illumination using a Ru(bipy)$_3$Cl$_2$ photosensitizer at pH 8.5, the catalyst exhibited significantly higher stability (up to 220 mol O_2 mol^{-1} catalyst) while maintaining a relatively high rate of catalysis (up to 0.67 mol O_2 mol^{-1} catalyst s^{-1}).

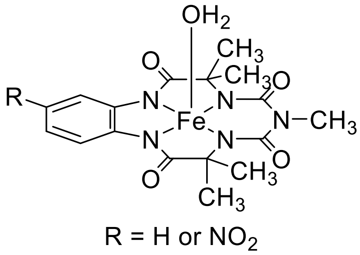

7-R

Scheme 1.4 Fe(TAML)(H_2O) complex used for solution-based solar water oxidation

Mechanistic experiments revealed that the catalyst most likely still undergoes a similar mechanism to the catalyst under acidic condition through the $Fe^{5+}=O$.

Although these catalysts represent accepted molecular water oxidation catalysts, many multi-nuclear metal complexes have demonstrated solar water oxidation in the presence of a photosensitizer and sacrificial oxidant in solution. One of the smallest class of multi-nuclear catalysts using this approach is the cobalt cubane structure originally reported by Chakrabarty et al. for oxidizing organic molecules depicted in Figure 1.3.[32] In the presence of $Ru(bipy)_3Cl_2$ under illumination, solar water oxidation was achieved, producing >40 mol O_2 mol^{-1} catalyst and $2.0x10^{-2}$ mol O_2 mol^{-1} catalyst s^{-1}.[33] At this time, the dependence of this catalyst's performance was also monitored. It was concluded that the catalyst operated maximally at pH 7.0 in a bicarbonate buffer ranging from pH 4.8-7.0. In addition to this report, it was later demonstrated that without the cobalt cubane structure, no water oxidation is observed for similar cobalt-oxo clusters.[34]

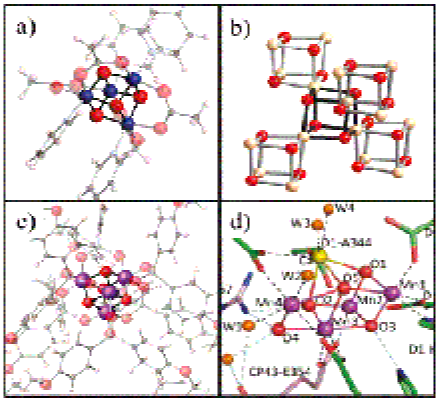

Figure 1.3 Crystal structures of active water oxidation catalysts (a) is the cobalt cubane structure reported by McCool et al. $[Co_4O_4(OAc)_4(pyr)_4]$ (**8**) compared to the active site for PSII (d); reprinted (adapted) with permission from McCool, N. S.; Robinson, D. M.; Sheats, J. E. *J. Am. Chem. Soc.* **2011**, *133*, 11446-11449. Copyright 2011 American Chemical Society.

Furthermore, in the presence of $Ru(bipy)_3Cl_2$ and under illumination, an increased quantum yield up to 34% was reported.[35] The quantum yield was pH dependent and demonstrated greater sensitivity to catalyst concentration at pH 8 than pH 7. In addition to the increased quantum yield, the rate of hole scavenging (that should limit reaction rates) was determined to be up to $1.6x10^7$ M^{-1} s^{-1} according to transient absorption spectroscopy. This experimental observation is important for future catalyst design because the rate of hole scavenging is important to maximize the stability of the excited photosensitizer.

The exciting comparison for the cobalt cubane clusters is the similarity between the cubane core and photosystem II (PSII). The excitement likely stems from the argument that since the two inorganic clusters are structurally similar, there is possibly some connection between their mechanisms. In PSII, the manganese centers are highly flexible within the manganese cluster. In contrast, the cobalt cubane clusters mentioned above all rely rigidly structured reactive sites. In 2013, there was a Co^{2+} cubane synthesized using hydroxymethyl pyridines in place of pyridine ligands to stabilize the cubane cluster as depicted by its crystal structure shown in Figure 1.4.[36] As a result, higher reactivity rates were observed under illumination compared to the Co^{3+} cubane clusters most likely due to the increased flexibility of the complex. This new complex was able to catalyze water oxidation under illumination up to 35 times at an initial rate of 4.4 mol O_2 mol^{-1} catalyst s^{-1}. The increase in rate is three orders of magnitude better than obtained for the Co^{3+} cubane previously reported. Although the stability is comparable to previously reported cubane clusters, the Co^{2+} cluster most likely benefits from faster kinetics due to higher structural flexibility.

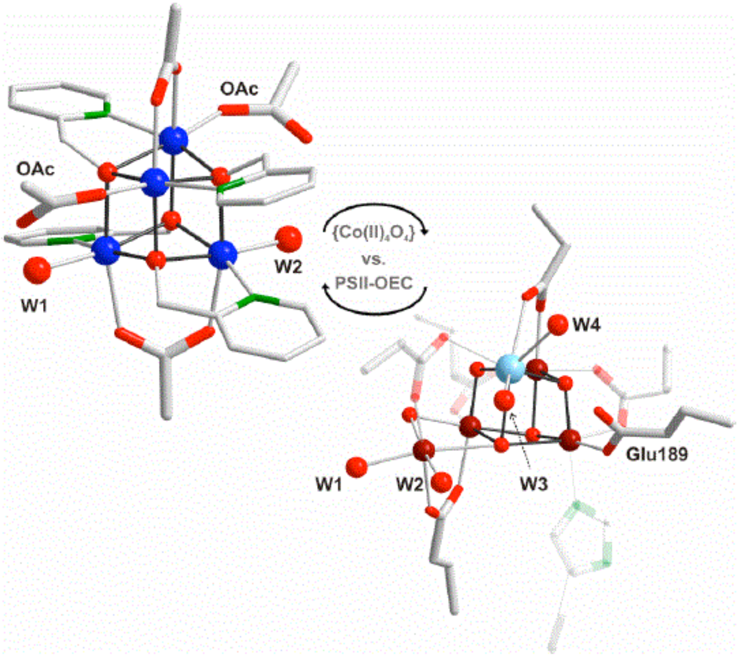

Figure 1.4 "Flexible" Co^{2+} cubane catalyst for solar water oxidation in solution where Co is blue, N is green, O is red, and C is white; reprinted with permission from Evangelesti, F.; Güttinger, R.; Moré, R. et al. *J. Am. Chem. Soc.* **2013**, *135*, 18734-18737. Copyright 2013 American Chemical Society.

Although the similarities to PSII are generally highlighted for cobalt cubane clusters including the organic ligands (mimicking a protein environment), the other type of "molecular" species that has been used for solar water oxidation in solution is the ruthenium and cobalt poly-oxo metallates.[37,38] $[\{Ru_4O_4(OH)_2(H_2O)_4\}(SiW_{10}O_{36})_2]^{10-}$ and $[Co_4(H_2O)_2(PW_9O_{34})_2]^{10-}$, have both demonstrated high reactivity in the presence of $Ru(bipy)_3Cl_2$ photosensitizer with high rates of catalysis up to 0.25 mol O_2 mol^{-1} catalyst s^{-1} for $[Co_4(H_2O)_2(PW_9O_{34})_2]^{10-}$ at pH 8.0. These catalysts demonstrated indefinite stability in the presence of a tetrameric $Ru(bipy)_3$ analog or $Ru(bipy)_3X_2$, and they are a promising new avenue for the field of molecular catalysts because they lack organic ligands that are often susceptible to detrimental oxidation.

Although intermolecular electron transfer is feasible in solution, it is naturally expected that intramolecular electron transfer is much faster and more probable. As a result, supramolecular ruthenium complexes depicted in Scheme 1.5 have been synthesized that

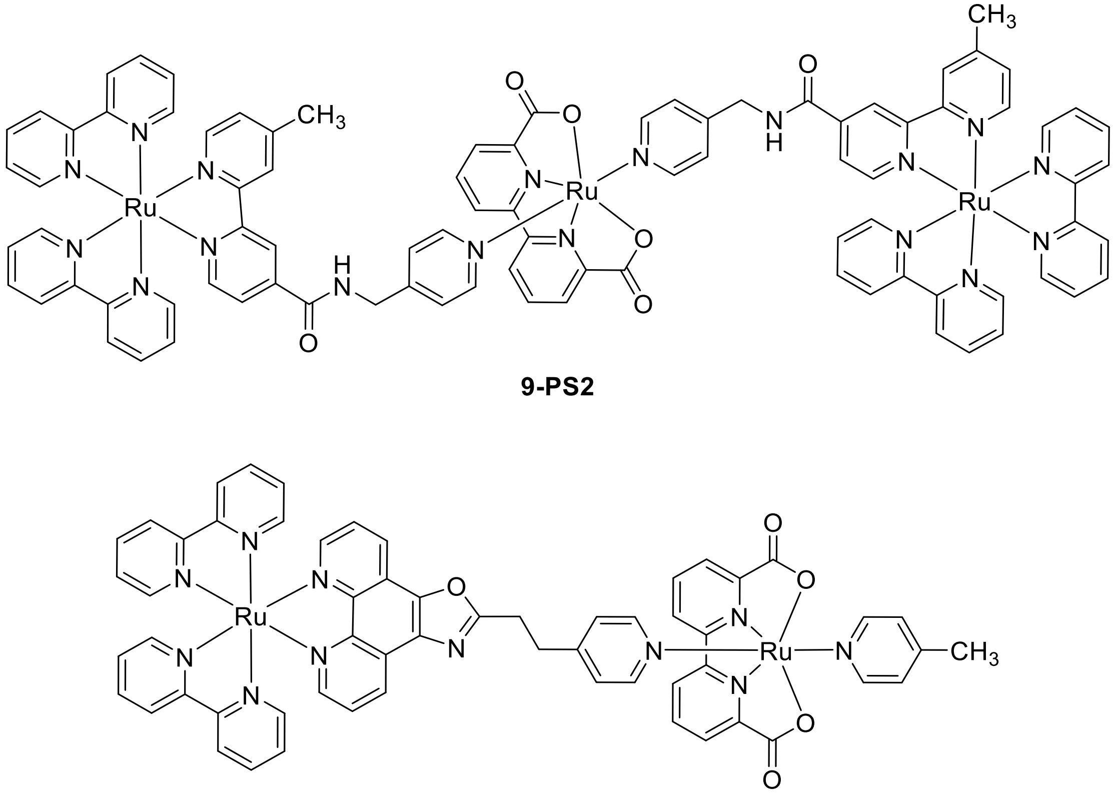

9-PS2

10-PS1

Scheme 1.5 Supramolecular complexes for solution-based solar water oxidation

include transfer electrons between the reaction center and the photosensitizer(s).[39,40] In both known instances, water oxidation is observed under illumination. In the case of **9-PS2** sensitizers, the reactivity of the complex was improved relative to the multi-component system as expected. Furthermore, it was observed that the amido-linkage was imperative for functionality. This observation suggests that electron transfer through the ligand may be less rapid than outer-sphere electron transfer between the reaction center and the photosensitizer. This phenomenon is apparent in the first report because when the sensitizers where linearly connected via a phenylene spacer to the reaction center, no reactivity was observed. However, when flexibility was imparted, then reactivity was observed. Although there may be some other explanation for this observation, it serves as a likely possibility for this catalytic system.

The second instance of supramolecular complexes for solar water oxidation examined a series of photosensitizers with different linkers between the catalyst and the light absorber. It was also demonstrated here that the unconjugated system possesses the highest stability for solar water oxidation, and the authors concluded that catalyst **10-PS1** was the best catalyst in their series as a result. This result was consistent with their previous report that the unconjugated linker possessed higher reactivity due to higher flexibility. In both cases, the stability of these catalysts were relatively low. However, this result could have been due to degradation/bleaching of the light absorber as has been observed for the multi-component systems.

1.2.2 Photocatalysis with Molecular Catalysts on Dye Sensitized Solar Cells

The use of molecular multi-component or supramolecular complexes to catalyze water oxidation under illumination is an important step forward for molecular WOCs. This process allows molecular WOCs to be rapidly screened under standardized reaction conditions for their ability to oxidize water in the presence of a molecular light absorber. However, the stability of these multi-component systems are limited because of the inherent photo-bleaching and subsequent degradation of the molecular light absorber. A major contributor to the degradation of the light absorber is the relatively slow electron transfer from the excited light absorber to the sacrificial electron acceptor.

Dye sensitized solar cells (DSSCs) circumvent the problem with electron transfer between the light absorber and the sacrificial electron acceptor, because the electrons are rapidly transferred to a semiconductor's (like TiO_2) conduction band that prevents the light absorber from degrading especially in the presence of an easily oxidized solution-based electron donor (like I^-). Because of $Ru(bipy)_3X_2$'s favorable electron transfer kinetics and electronic structure, this molecular light absorber has found extensive use in DSSCs as illustrated in Figure 1.5.

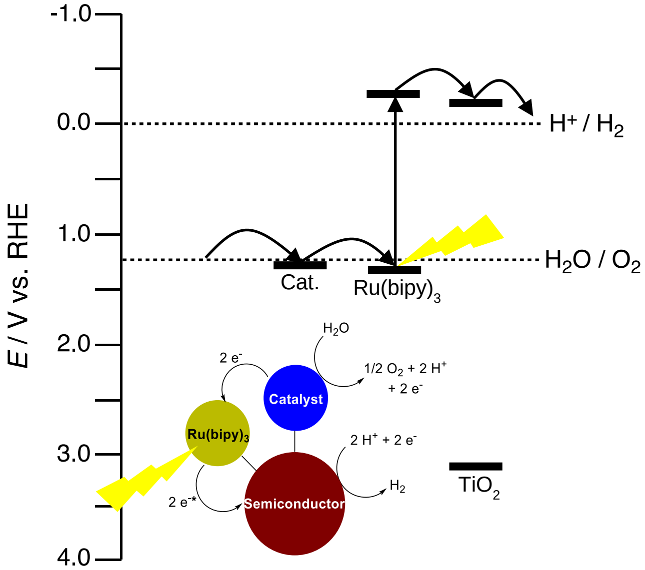

Figure 1.5 Electrochemical potential energy diagram of DSSC-molecular WOC construct

However, it took several years before the first photocatalytic water oxidation was achieved using DSSCs. In 2008, Mallouk and co-workers designed a photocatalytic cell that used an iridium oxide water oxidation catalyst attached to the DSSC surface to "photosensitize" the heterogeneous electrocatalyst iridium oxide.[41] Although the initial system directly coupled the catalyst to the $Ru(bipy)_3$ dye as pictured in Figure 1.6, they later reported an improvement in catalysis by separating the water oxidation catalyst and dye on the semiconductor and facilitating electron transfer through a co-additive.[42] As a result, the rate of catalysis was significantly improved along with the photocurrent density of the modified DSSC in the presence of water.

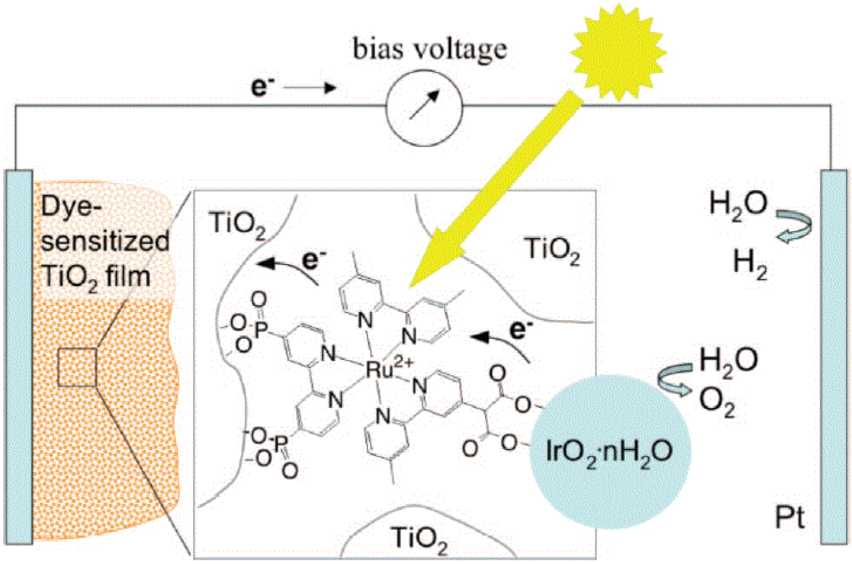

Figure 1.6 Schematic of iridium oxide electrocatalyst photosensitized by a Ru(bipy)$_3$ | TiO$_2$ DSSC; Reprinted with permission from Youngblood, J. W.; Lee, S-H. A.; Kobayashi, Y. et al. *J. Am. Chem. Soc.* **2009**, *131*, 926-927. Copyright 2009 American Chemical Society.

The primary difference between this approach towards photosensitizing molecular water oxidation catalysts and the solution-based approach is the destination of the excited state electron. In the solution-based approach, the electron must still be collected by a sacrificial oxidant. But, in this new approach, the electron is transferred to the conduction band of the TiO$_2$ and can be used to reduce protons at a separate electrode. As a result, a useful chemical reaction is being carried out as opposed to the byproduct of sacrificial oxidant reduction.

The initial discovery of this system resulted in several new examples of using DSSCs to activate molecular WOCs towards solar water oxidation. However, modifying molecular catalysts to attach them on semiconductors is not often trivial. A faster way to attach a molecular catalyst to a DSSC is through the use of Nafion membranes. Nafion is a positively charge proton exchange membrane that can be doped with molecular complexes and allows easy diffusion of water throughout the membrane.[43] Sun and co-workers used the method of doping Nafion membranes with the ruthenium catalyst (**3**) on a TiO$_2$ DSSC to activate the molecular catalyst for solar water oxidation.[44] If the Nafion was used as prepared (typically under acidic conditions) on the DSSC, the catalyst system exhibited no increase in photocurrent density because the catalyst primarily operates at higher pH. However, when the initial pH of the Nafion was adjusted to 7.0 and then 9.8, the photocurrent obtained in the presence of the catalyst was significantly improved.

When the Nafion was prepared at pH 7.0, the rapid evolution of oxygen and protons greatly increased the local acidity in the membrane, and resulted in rapid decay of the catalyst and subsequently the photocurrent. But, in the pH 9.8 Nafion membrane, the catalyst exhibited stability under illumination for 1 hour and had a 5-fold increase in photocurrent compared to the DSSC with Nafion excluding the catalyst. The oxygen production could be monitored for this system and produced oxygen at an initial rate of 0.0075 mol O_2 mol^{-1} cat s^{-1}. After 1 hour of illumination, 16 complete turnovers (mol O_2 mol^{-1} catalyst) were achieved. This result represented the first example of using a DSSC to activate a molecular catalyst for solar water oxidation.

Although Nafion is a faster way to ensure catalyst attachment on the surface of the DSSC, the electron transfer could be sluggish due to the poor conductivity of the membrane, and not all active catalysts may be activated by the DSSC. As such, other advances in this technology have resulted through the use of co-adsorption of a light absorbing dye and the molecular catalyst. In this instance, it is important that the catalyst and dye are directly attached to the electrode surface. However, if the catalysts can be modified successfully to include an anchoring group that is stable under aqueous conditions, then a multicomponent system is feasible. This approach also uses the observation originally gleaned by Mallouk and co-workers that suggests the components are most efficient when they are not directly attached to one another.[42]

The first example of a co-adsorbed water oxidizing DSSC was by Moore et al.[45] In this example, an iridium water oxidation catalyst and a zinc porphyrin dye were co-deposited on TiO_2. Time-resolved terahertz spectroscopy was utilized to probe the impact of co-adsorption on electron injection into TiO_2's conduction band. It was concluded from this experiment that the co-adsorbed molecules work in tandem on the surface as opposed to individual components because the co-adsorbed film exhibits a lower injection amplitude relative to films with only one of the components.

Furthermore, the photocurrent showed a 6-fold increase when coupled with both the dye and catalyst, but exhibited minimal improvement in photocurrent with the separate components under 200 mW cm^{-2} solar illumination. The products from prolonged illumination are not reported in this instance, but that was most likely due to the inherent instability of carboxylic acid anchoring groups on TiO_2 in aqueous environments.[46] In addition to demonstrating an increased initial rate of solar water oxidation, this system was also the first example of a non-ruthenium-based dye as the light absorber.

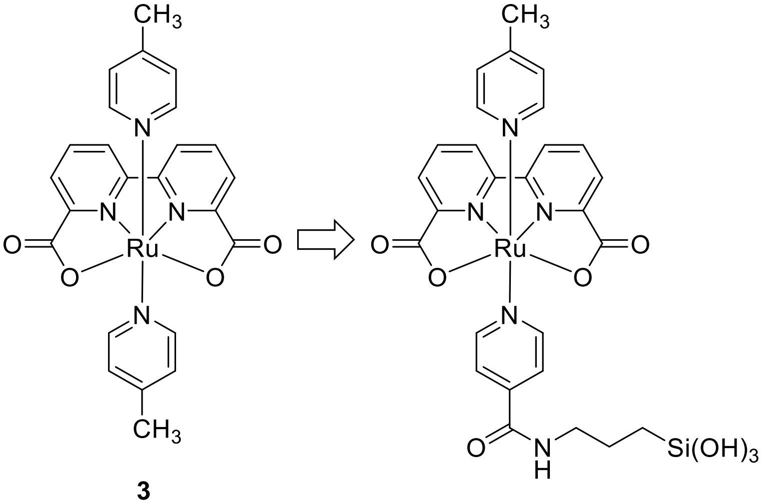

3

Scheme 1.6 Modified ruthenium catalyst **3** used for solar water oxidation on a DSSC developed by Sun and co-workers

Although the previous example demonstrated the feasibility of the multicomponent approach using a unique dye coupled to TiO_2, the only other successful report of the multicomponent report comes as an extension of the Nafion example mentioned above. Using a modified version of the catalyst **3** depicted in Scheme 1.6, and anchoring that complex to a $Ru(bipy)_3$ | TiO_2 DSSC, Sun and co-workers demonstrated an unprecedented increase in photocurrent under 300 mW cm^{-2} illumination from negligible photocurrent up to ~2.0 mA cm^{-2} over 10 seconds at pH 8.[47] The current decayed relatively quickly (<50 seconds) to ~0.8 mA cm^{-2}, which appeared relatively stable. After 500 seconds of illumination, the co-adsorbed catalyst achieved 498 mol O_2 mol^{-1} catalyst at a rate of 1.0 mol O_2 mol^{-1} catalyst s^{-1}. Additionally, the Faradaic efficiency for this electrode for O_2 and H_2 were 83% and 74%, respectively. This result equated to a significant improvement in incident photon-to-current efficiency (IPCE). For the DSSC itself, an IPCE of ~1% was achieved at 450 nm. However, the co-adsorbed electrode exhibited an IPCE of ~14%. This report represents a huge leap forward for using this approach towards efficient solar water oxidation.

The results reported from this section allude to the idea that a multicomponent catalytic system is necessary for successful and efficient charge transfer. In further support of this idea, many molecular assemblies containing dyes and molecular catalysts (i.e. supramolecular catalysts) have been reported on ITO or ITO-TiO_2 electrodes.[48,49,50] However, these reports focus primarily on the charge transfer kinetics between the assembly and the electrode or semiconductor and the electrocatalytic capabilities of the assembly when anchored to the electrodes. Therefore, while this approach could be useful for solar water oxidation devices, it has not demonstrated better photoelectrochemical properties at this point.

1.2.3 Photocatalysis by Anchoring Molecular Catalysts to Semiconductors

In the previous two sections, discreet molecules are relied on as the light absorbing component to activate the molecular WOCs. However, as has been mentioned previously, the molecular dyes often degrade due to unstable oxidation states after excitation. Furthermore, the dye acts as a mediator between the catalyst and the final electron acceptor (in the DSSC case the semiconductor is the "final" electron acceptor for all intents and purposes). To simplify this whole approach, it would be ideal to replace the molecular dye with a more stable light absorber that can also act as the final electron acceptor. Therefore, semiconductors have been targeted as the light absorber and electron acceptor to activate molecular catalysts anchored to the surface.

There is an important distinction between this approach and the DSSC approach mentioned above. Namely, the electron from the catalyst is being transferred into the conduction or valence band of the material (Figure 1.7). Because the conduction band is primarily devoid of electrons, the electrons transferred into the conduction band can move rapidly through the material. However, the valence band is already primarily filled with electrons. As a result, the minority carriers (photo-generated holes) must reach the surface, collect the electron, and move the electron away from the surface. The concentration of the minority carriers are significantly lower in the valence band, and that could inhibit the ability to transfer electrons between the catalyst and the semiconductor.

Although this aspect serves as a potential limitation of this approach, the major

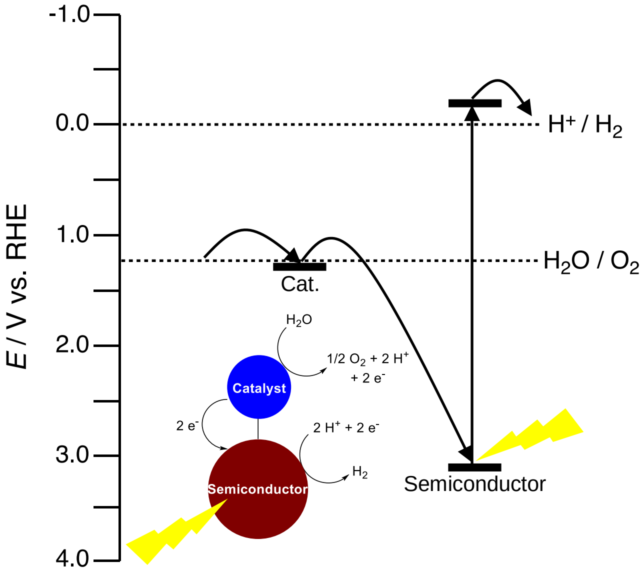

Figure 1.7 Electrochemical potential energy diagram of catalyst-semiconductor construct

advantage that is gained relative to molecular light absorbers is the significantly larger oxidative potential energy that can be accessed by the semiconductor. For instance, the molecular light absorber $Ru(bipy)_3X_2$ has redox potential of 1.26 V vs. RHE. Therefore, the onset of electrocatalysis for the molecular catalyst must fall between that potential and the potential for water oxidation (1.23 V vs. RHE). The only way molecular catalysts can achieve that is because $Ru(bipy)_3X_2$'s potential is *not* pH dependent. As a result, as the pH increases, the potential energy difference between water oxidation (pH dependent) and the light absorbing dye increases leaving space for the catalyst to be thermodynamically oxidized by the dye and still be capable of oxidizing water.

On the other hand, the valence band of a metal oxide semiconductor is typically comprised of fill O 2p orbitals. The energy of the valence band is therefore generally ~3 eV vs. RHE. This energy is a significantly wider potential energy range to activate a molecular catalyst than 1.26 V for the $Ru(bipy)_3X_2$ molecular dye. As will be discussed later, this property has many implications for applying enough extra potential energy to activate molecular complexes that are otherwise incapable of oxidizing water under standard homogeneous condition.[51]

The first example of this approach successfully improving the rate of catalysis on a semiconductor surface is through anchoring the ruthenium polypyridyl complexes (see Scheme 1.7) onto hematite Fe_2O_3.[52] In this example, linear sweep voltammetry (LSV) was the only method used to probe the impact of the catalyst on the semiconductor surface. The stated reason for only using this experiment is, again, due to the instability of carboxylic acid anchoring groups in aqueous solutions. However, the authors were still capable of probing the improvement in catalytic rate by LSV under illumination. The photocurrent of the semiconductor increased up to 2-fold through modification with catalyst **13**. Furthermore, catalyst **12** that did not contain an anchoring group showed oxidation of the complex under illumination was possible, but the complex did not enhance the rate of water oxidation on the Fe_2O_3 at higher potentials. These results suggest that the covalent linkage is likely important for improving the rate of water oxidation on the semiconductor surface.

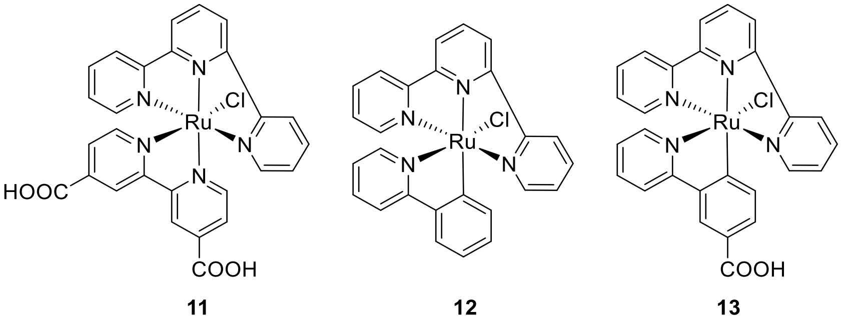

Scheme 1.7 Ruthenium catalysts anchored to Fe_2O_3 for solar water oxidation

Comparing catalysts **11** and **13**, they concluded that the strong C-Ru sigma bond resulted in a more efficient electron transfer between the catalyst and the semiconductor for solar water oxidation. However, the difference in homogeneous reactivity was not compared. Therefore, it’s hard to know whether the catalyst is simply faster at oxidizing water or if the electron transfer was truly faster.

Using a similar ruthenium complex depicted in Scheme 1.8, Fujita and co-workers saw a 60 mV shift in the onset of water oxidation for the ruthenium catalyst X on WO_3.[53] However, the main conclusion from their work was that competitive light absorption from the ruthenium complex on the WO_3 surface prevent improvement of the saturated photocurrent for the modified electrodes. Furthermore, they still observed instability of the catalyst on the electrode surface that resulted in photoelectrochemical performance

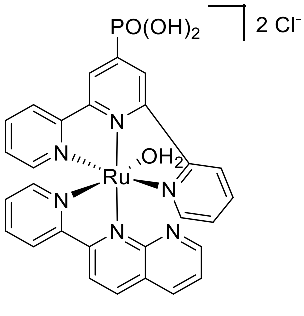

14

Scheme 1.8 Ruthenium catalyst anchored to WO_3 for solar water oxidation

reverting back to that of unmodified WO_3.

In both of the previous instances, ruthenium catalysts were used as the molecular catalyst. However, ruthenium has strong visible light absorption characteristics. Ruthenium WOCs also tend to have reversible redox potentials between inactive complexes and the resting catalyst. Through modification of the most stable iron WOC to catalyst **15** (see Scheme 1.9), we were able to successfully demonstrate an increase in rate of water oxidation up to 60% on WO_3.[54] Furthermore, although the iron catalyst does detach from the electrode surface to some extent during illumination, enough catalyst remains bound to improve the rate over a prolonged period of time.

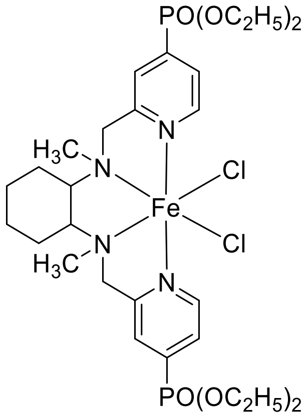

15

Scheme 1.9. Targeted phosphonate modified molecular Fe WOCs

Along with improving the rate of catalysis, we were able to quantify the products of the reaction under 3 hours of illumination. Tungsten oxide was ideal for examining this catalyst because it performs multiple side-reactions in the presence of various anions.[55,56] Therefore, if the catalyst is the primarily active species on the semiconductor surface under illumination, then the selectivity of the modified semiconductor should be drastically improved. In fact, the selectivity of WO_3 improved from 56% to 79% for the modified electrode in the presence of sulfate anions at pH 3. The catalyst exhibited higher stability and higher reactivity on the surface. Assuming 100% catalyst retention on the electrode, then the catalyst performs 700-1,000 turnovers during 3 hours of illumination at a rate of 0.07-0.09 mol O_2 mol^{-1} catalyst s^{-1}. The catalyst activity was retained on the surface up to ~6 hours of illumination. This report represented the first example of this system being used to quantify the amount of O_2 produced using the semiconductor only as the light absorber.

In addition to improving the photocatalytic performance of WO_3, iron catalyst **15** also improved the rate of water oxidation when anchored to $CuWO_4$.[57] $CuWO_4$ was explored because the band gap of the material is smaller despite having a conduction band energy similar to WO_3. When the iron catalyst was anchored to $CuWO_4$ prepared via various synthetic methods, the enhancement in photocurrent ranged from 35-100%. This observation suggests that the semiconductor not only plays an important role in activating the molecular catalyst, but the physical properties of the prepared electrode also plays an important role in the amount of photocurrent enhancement observed.

Following reports of other molecular WOCs using other first-row transition metal catalysts, the complex **15**'s ligand scaffold seemed like an excellent model system for activating other first-row transition metal complexes of the same structure. Although the series of complexes from Co-Zn did not demonstrate any homogeneous reactivity for water oxidation using chemical or electrochemical oxidants, the complexes containing Ni, Cu, and Zn all caused the photocurrent and selectivity of WO_3 to increase under 100 mW cm^{-2} illumination.[51] These results suggest that the additional potential energy from the valence band of a semiconductor can be employed to oxidize/activate complexes that have previously been unable to oxidize water.

As discussed in the previous section, another way to successfully adhere a molecular catalyst to an electrode surface is through the use of a Nafion membrane. Sun and co-workers demonstrated that doping a Nafion membrane with the cobalt cubane cluster from Figure 1.3 and attaching the membrane to hematite Fe_2O_3, the rate of solar water oxidation and the onset for solar water oxidation improved significantly.[58] The photocurrent increased by 3-fold under illumination at 300 mW cm^{-2} and the onset potential shifted ~400 mV negative. Under prolonged illumination, the cobalt cubane structure quantitatively produced O_2, and was stable indefinitely within the Nafion membrane once oxygen bubbles were removed after prolonged illumination.

Although all of these approaches for activating molecular WOCs towards solar water oxidation play important roles in designing better molecular water oxidation catalysts, this approach seems to have the greatest implications in terms of catalyst scope and the inherent stability of metal oxides in aqueous environments because of the wide electrochemical potential window accessible for activating molecular catalysts. For this approach to truly blossom, it is important to find more stable anchoring groups for attaching the molecular catalysts to the semiconductor surfaces under basic conditions since numerous catalysts operate only at high pH. Furthermore, to date there has been little rationale provided for the selection of the light absorbing semiconductor. It would be prudent to understand the role the electronic structure of the semiconductor plays in activating the molecular catalysts.

1.3 Scope of this Thesis

The goal of this thesis is to recollect and summarize the contributions this research has made towards improving our understanding of anchoring molecular catalysts to semiconductor surfaces and the attempted application to the fastest known ruthenium water oxidation catalysts in Chapter 2. It also serves as the first example where solar activation and quantification of products of an earth-abundant first-row transition metal catalyst is achieved in Chapter 3. Chapter 4 is intended to delve deeper into the application of the earth-abundant iron WOC developed in Chapter 3 on different semiconductors as initially examined in Chapter 2. A major implication of this work is the ability to use much higher oxidative potential energies from the semiconductors to activate molecular species. As such, Chapter 5 summarizes the work that has been done to activate complexes that are unable to oxidize water under standard homogeneous reaction conditions. Finally, the general conclusions from this research and the outlook for future research in this field are summarized in Chapter 6. Additional figures pertinent to supporting arguments made in Chapters 2-5 are included in Appendices A-D respectively and they are referenced accordingly throughout this document.

References

1 Lewis, N. S.; Nocera, D. G. *Pro. Nat. Sci. Acad.* **2006**, *103*, 15729.

2 O'Neill, B. C.; Dalton, M.; Fuchs, F.; Jiang, L.; Pachaun, S.; Zigova, K. *Pro. Nat. Sci. Acad.* **2010**, *107*, 17521.

3 Flato, G.; Marotzke, J. Evaluation of Climate Models. In *Climate Change 2013: The Physical Science Basis for the Intergovernmental Panel on Climate Change*; Stocker, T. F.; Qin, D. Eds. Cambridge University Press: New York, NY, 2013; p741-866.

4 Kousksou, T.; Bruel, P.; Jamil, A.; Rhafiki, T. E.; Zeraouli, Y. *Sol. Energ. Mat. Sol. C.* **2014**, *120*, 59.

5 Ferrazza, F. Crystalline Silicon: Manufacture and Properties. Jäger-Waldau, A. *Solar Cells: Materials, Manufacturing, and Operation*, 2nd ed.; McEvoy, A.; Castaner, L.; Markvart, T. Eds. Academic Press: Waltham, MA, 2013; 69-85.

6 Hagfeldt, A.; Cappel, E. B.; Boschloo, G.; Sun, L.; Kloo, L.; Pettersson, H.; Gibson, E. A. Dye-Sensitized Photoelectrochemical Cells. In *Solar Cells: Materials, Manufacturing, and Operation*, 2nd ed.; McEvoy, A.; Castaner, L.; Markvart, T. Eds. Academic Press: Waltham, MA, 2013; 385-441.

7 Jäger-Waldau, A. The Photovoltaic Industry. In *Solar Cells: Materials, Manufacturing, and Operation*, 2nd ed.; McEvoy, A.; Castaner, L.; Markvart, T. Eds. Academic Press: Waltham, MA, 2013; 565-583.

8 Chen, H.; Cong, T. N.; Yang, W.; Tan, C.; Li, Y.; Ding, Y. *Prog. Nat. Sci.* **2009**, *19*, 291.

9 Turner, J.; Sverdrup, G.; Mann, M. K.; Maness, P-C.; Kroposki, B.; Ghirardi, M.; Evans, R. J.; Blake, D. *Int. J. Energy Res.* **2008**, *32*, 379.

10 Bard, A. J.; Fox, M. A. *Acc. Chem. Res.* **1995**, *28*, 141.

11 Gersten, S. W.; Samuels, G. J.; Meyer, T. J. *J. Am. Chem. Soc.* **1982**, *104*, 4029.

12 a) Elizarova, G. L.; Matvienko, L. G.; Lozhkina, N. V.; Parmon, V. N.; Zamaraev, K. I. *React. Kinet. Catal. Lett.* **1981**, *16*, 191; b) Elizarova, G. L.; Matvienko, L. G.; Lozhkina, N. V.; Maizlish, V. E.; Parmon, V. N. *React. Kinet. Catal. Lett.* **1981**, *16*, 285; c) Elizarova, G. L.; Matvienko, L. G.; Lozhkina, N. V.; Parmon, V. N. *React. Kinet. Catal. Lett.* **1983**, *22*, 49; d) Elizarova, G. L.; Matvienko, L. G.; Lozhkina, N. V.; Parmon, V. N. *React. Kinet. Catal. Lett.* **1984**, *26*, 67.

13 Barnett, S. M.; Goldberg, K. I.; Mayer, J. M. *Nat. Chem.* **2012**, *4*, 498.

14 Limburg, J.; Vrettos, J. S.; Liable-Sands, L. M.; Rheingold, A. L.; Crabtree, R. H.; Brudvig, G. W. *Science* **1999**, *283*, 1524.

15 Duan, L.; Bozoglian, F.; Mandal, S.; Stewart, B.; Privalov, T.; Llobet, A.; Sun, L. *Nat. Chem.* **2012**, *4*, 418.

16 Ellis, W. C.; McDaniel, N. D.; Bernhard, S.; Collins, T. J. *J. Am. Chem. Soc.* **2010**, *132*, 10990.

17 Fillol, J. L.; Codolá Z.; Garcia-Bosch, I.; Gómez, L.; Pla, J. J.; Costas, M. *Nat. Chem.* **2011**, *3*, 807.

18 McCool, N. S.; Robinson, D. M.; Sheats, J. E.; Dismukes, G. C. *J. Am. Chem. Soc.* **2011**, *133*, 11446.

19 Wasylenko, D. J.; Palmer, R. D.; Schott, E.; Berlinguette, C. P. *Chem. Commun.* **2011**, *47*, 4249.

20 Hong, D.; Jung, J.; Park, J.; Yamada, Y.; Suenobu, T.; Lee, Y.; Nam, W.; Fukuzumi, S. *Energy Environ. Sci.* **2012**, *5*, 7607.

21 Zhang, M-T.; Chen, Z.; Kang, P.; Meyer, T. J. *J. Am. Chem. Soc.* **2013**, *135*, 2048.

22 Zong, R.; Thummel, R. P. *J. Am. Chem. Soc.* **2005**, *127*, 12802-12803.

23 Representative examples: a) Wasylenko, D. J.; Ganesamoorthy, C.; Koivisto, B. D.; Henderson, M. A.; Berlinguette, C. P. *Inorg. Chem.* **2010**, *49*, 2202. b) Concepcion, J. J.; Jurss, J. W.; Templeton, J. L.; Meyer, T. J. *J. Am. Chem. Soc.* **2008**, *130*, 16462. c) Duan, L.; Xu, Y.; Tong, L.; Sun, L. *Chem. Sus. Chem.* **2011**, *4*, 238.

24 a) Kalyanasundaram, K. *Coord. Chem. Rev.* **1982**, *46*, 159; b) Montalti, M.; Cedi, A.; Prodi, L.; Gandolfini, M. T. In *Handbook of Photochemistry*, 3rd ed.; CRC Press Taylor & Francis Group: Boca Raton, FL, 2006; 379–404.

25 Rotzinger, F. P.; Munavalli, S.; Comte, P.; Hurst, J. K.; Grätzel, M.; Pern, F-J.; Frank, A. J. *J. Am. Chem. Soc.* **1987**, *109*, 6619.

26 Cape, J. L.; Hurst, J. K. *J. Am. Chem. Soc.* **2008**, *130*, 827-829.

27 Concepcion, J. J.; Jurss, J. W.; Templeton, J. L.; Meyer, T. J. *Pro. Nat. Sci. Acad.* **2008**, *105*, 17632.

28 Xu, Y.; Fischer, A.; Duan, L.; Tong, L.; Gabrielsson, E.; Akermark, B.; Sun, L. *Angew. Chem. Int. Ed.* **2010**, *49*, 8934.

29 Duan, L.; Xu, Y.; Gorlov, M.; Tong, L.; Andersson, S.; Sun, L. *Chem. Eur. J.* **2010**, *16*, 4659.

30 Duan, L.; Xu, Y.; Tong, L.; Sun, L. *Chem. Sus. Chem.* **2011**, *4*, 238.

31 Panda, C.; Debgupta, J.; Díaz, D. D.; Singh, K. K.; Gupta, S. S.; Dhar, B. B. *J. Am. Chem. Soc.* **2014**, *136*, 12273.

32 Chakrabarty, R.; Bora, S. J.; Das, B. K. *Inorg. Chem.* **2007**, *46*, 9450.

33 McCool, N. S.; Robinson, D. M.; Sheats, J. E.; Dismukes, G. C. *J. Am. Chem. Soc.* **2011**, *133*, 11446.

34 Smith, P. F.; Kaplan, C.; Sheats, J. E.; Robinson, D. M.; McCool, N. S.; Mezle, N.; Dismukes, G. C. *Inorg. Chem.* **2014**, *53*, 2113.

35 Ganga, G. L.; Puntoriero, F.; Campagna, S.; Bazzan, I.; Berardi, S.; Bonchio, M.; Sartorel, A.; Natali, M.; Scandola, F. *Faraday Discuss.* **2012**, *155*, 177.

36 Evangelisti, F.; Güttinger, R.; Moré, R.; Luber, S.; Patzke, G. R. *J. Am. Chem. Soc.* **2013**, *135*, 18734.

37 Geletii, Y. V.; Bota, B.; Kögerler, P.; Hillesheim, D. A.; Musaev, D. G.; Hill, C. L. *Angew. Chem. Int. Ed.* **2008**, *47*, 3896.

38 Huang, Z.; Luo, Zz.; Geletii, Y. V.; Vickers, J. W.; Yin, Q.; Wu, D.; Hou, Y.; Ding, Y.; Song, J.; Musaev, D. G.; Hill, C. L.; Lian, T. *J. Am. Chem. Soc.* **2011**, *133*, 2068.

39 Li, F.; Jiang, Y.; Zhang, B.; Huang, F.; Gao, Y.; Sun, L. *Angew. Chem. Int. Ed.* **2012**, *51*, 2417.

40 Gao, Y.; Duan, L.; Yu, Z.; Ding, X.; Sun, L. *Faraday Discuss.* **2014**, DOI: 10.1039/c4fd00127c.

41 Youngblood, W. J.; Lee, S-H. A.; Kobayashi, Y.; Hernandez-Pagan, E. A.; Hoertz, P. G.; Moore, T. A.; Moore, A. L.; Gust, D.; Mallouk, T. E. *J. Am. Chem. Soc.* **2009**, *131*, 926.

42 Zhao, Y.; Swierk, J. R.; Megiatto, J. D. Jr.; Sherman, B.; Youngblood, W. J.; Qin, D.; Lentz, D. M.; Moore, A. L.; Moore, T. A.; Gust, D.; Mallouk, T. E. *Pro. Nat. Sci. Acad.* **2012**, *109*, 15612.

43 Chae, K, J.; Choi, M.; Ajayi, F. F.; Park, W.; Chang, I. S.; Kim, I. S. *Energy & Fuels* **2008**, *22*, 169.

44 Li, L.; Duan, L.; Xu, Y.; Gorlov, M.; Hagfeldt, A.; Sun, L. *Chem. Comm.* **2010**, *46*, 7265.

45 Moore, G. F.; Blakemore, J. D.; Milot, R. L.; Hull, J. F.; Song, H-e.; Cai, L.; Schmuttenmaer, C. A.; Crabtree, R. H.; Brudvig, G. W. *Energy Environ. Sci.*, **2011**, *4*, 2389.

46 McNamara, W. R.; Milot, R. L.; Song, H-e.; Snoeberger, R. C. III; Batista, V. S.; Schmuttenmaer, C. A.; Brudvig, G. W.; Crabtree, R. H. *Energy Environ. Sci.* **2010**, *3*, 917.

47 Gao, Y.; Ding, X.; Liu, J.; Wang, L.; Lu, Z.; Li, L.; Sun, L. *J. Am. Chem. Soc.* **2013**, *135*, 4219.

48 Concepcion, J. J.; Jurss, J. W.; Brennaman, M. K.; Hoertz, P. G.; Patrocinio, A. O. T.; Iha, N. Y. M.; Templeton, J. L.; Meyer, T. J. *Acc. Chem. Res.* **2009**, *42*, 1954.

49 Song, W.; Glasson, C. R. K.; Luo, H.; Hanson, K.; Brennaman, M. K.; Concepcion, J. J.; Meyer, T. J. *J. Phys. Chem. Lett.* **2011**, *2*, 1808.

50 Ryan, D. M.; Coggins, M. K.; Concepcion, J. J.; Ashford, D. L.; Fang, Z.; Alibabaei, L.; Ma, D.; Meyer, T. J.; Waters, M. L. *Inorg. Chem.* **2014**, *53*, 8120.

51 In preparation M-2 on WO_3 Chapter 5

52 Chen, X.; Ren, X.; Liu, Z.; Zhuang, L.; Lu, J. *Electrochem. Commun.* **2013**, *27*, 148.

53 Zhong, D. K.; Zhao, S.; Polyansky, D. E.; Fujita, E. *J. Catal.* **2013**, *307*, 140.

54 Klepser, B. M.; Bartlett, B. M. *J. Am. Chem. Soc.* **2014**, *136*, 1694-1697.

55 a) Mi, Q.; Zhanaidarova, A.; Brunschwig, B. S.; Gray, H. B.; Lewis, N. S. *Energy Environ. Sci.* **2012**, *5*, 5694; b) Mi, Q.; Coridan, R. H.; Bruschwig, B. S.; Gray, H. B.; Lewis, N. S. *Energy Environ. Sci.* **2013**, DOI 10.1039/C3EE40712H.

56 Hill, J. C.; Choi, K-S. *J. Phys. Chem. C* **2012**, *116*, 7612.

57 In prepartion Fe-2 on $CuWO_4$ Chapter 4.

58 Zhang, B.; Li, F.; Yu, F.; Wang, X.; Zhou, X.; Li, H.; Jiang, Y.; Sun, L. *ACS Catal.* **2014**, *4*, 804.

Chapter 2

Modeling Adsorption Affinity and Aqueous Stability of Anchors

2.1 Introduction

The goal of this thesis is to create a functional photocatalyst that combines molecular WOCs with semiconductor light absorbers. With this goal in mind, the first question that needs to be addressed is how a molecular WOCs can be directly bound to a semiconductor. The second important question is what catalysts should be targeted for this approach. To address the first question, the dye sensitized solar cell (DSSC) literature is examined. DSSCs have been pursued extensively for their ability to convert solar energy to electricity.[1] One of the most important aspects to creating a successful DSSC is the amount of dye that can be loaded onto a semiconductor surface. As a result of this work, numerous experiments have been carried out to examine the impact of various anchoring groups on the surface loading for different dyes.[2] The most common anchoring group used in the DSSC literature is the carboxylic acid moiety followed by the phosphonic acid moiety. Along with the most common anchoring substituents, as depicted in Scheme 2.1, there are numerous other anchoring groups that have found utility in DSSCs.[3]

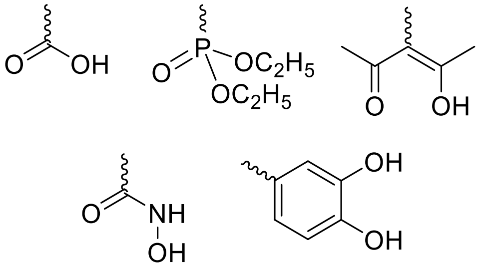

Scheme 2.1 Common anchoring groups for DSSC dyes

Although the primary concerns of DSSCs are surface coverage and rate of charge transfer, DSSCs typically operate under non-aqueous conditions. As a result, most of the anchors employed in DSSCs exhibit excellent stability on the semiconductor surface. However, in a functional solar water splitting cell the catalyst must remain on the

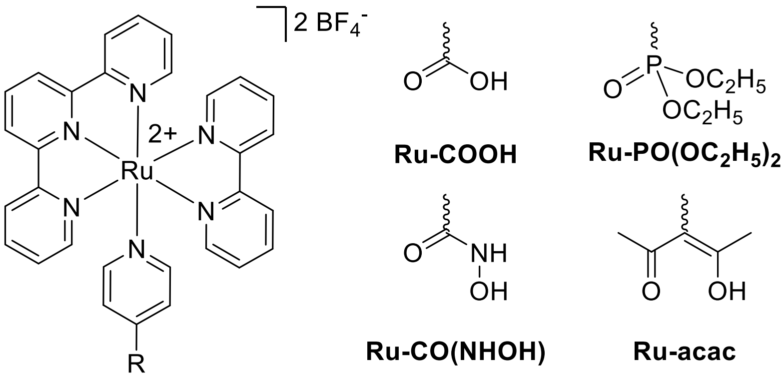

Scheme 2.2 Targeted polypyridyl complexes

semiconductor surface under a variety of aqueous conditions. The most important condition to consider then is the pH stability of various anchors. Although numerous anchoring groups have been developed for DSSCs, there are very few literature examples comparing the stability of the more common anchoring group in aqueous solutions at various pH.[4,5] To have a better understanding of anchoring group stabilities at various pH, a series of polypyridyl ruthenium complexes are prepared containing common anchoring substituents as depicted in Scheme 2.2.

The second major question is which catalyst should be pursued for attachment to a semiconductor. At first glance, it is obvious to pursue the fastest know molecular WOC (**Ru**) depicted in Scheme 2.3.[6,7] However, the catalyst is known to operate through a

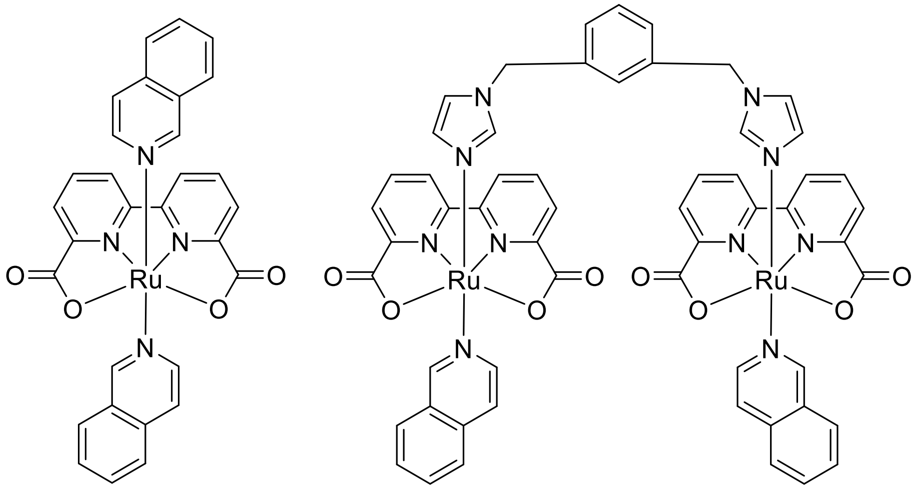

Ru **Ru$_2$**

Scheme 2.3 Fastest ruthenium WOCs

dimeric transition state. As a result, there is some concern that the catalyst will be unable to operate once anchored to semiconductor surface. To circumvent this concern, a bridged binuclear catalyst (**Ru$_2$**) is also targeted for modification with the best pH stable anchor from the model complexes. The bridged catalyst has shown comparable reactivity towards water oxidation with respect to **Ru**.[7]

2.2 Synthesis of Model Complexes

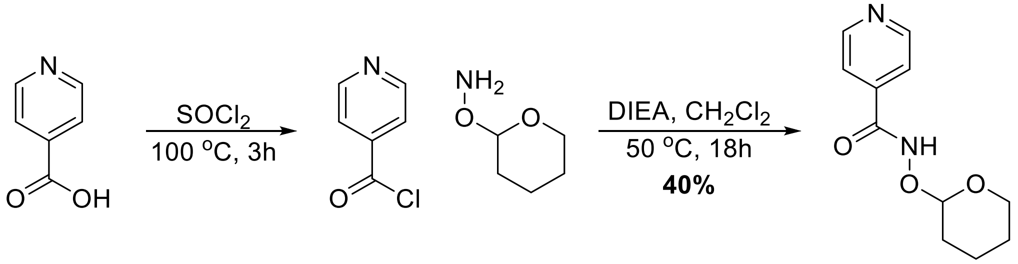

Scheme 2.4 Synthesis of **-CO(NHOTHP)** from **-COOH**

The advantage of selecting the best anchoring group using polypyridyl ruthenium complexes as a model is that the anchoring group can be incorporated easily through the bound pyridine. The modified pyridines are synthesized or targeted via Scheme 2.4 and Scheme 2.5. Intermediate **I** is synthesized from RuCl$_3$*xH$_2$O through addition of terpyridine. Complex **II** is prepared by addition of bipyridine and reduction with NEt$_3$ as illustrated in Scheme 2.6.[8,9] From complex **II**, pyridine could not be coordinated until the chloride ligands are removed. Therefore, the aquo complex **III** is prepared prior to coordinating the desired pyridine to obtain (**Ru-R**), in moderate to good yields. In the case of **Ru-CO(NHOTHP)**, the aqueous acidic workup results in the deprotection of the –THP protecting group resulting in the desired **Ru-CO(NHOH)** complex albeit in very low

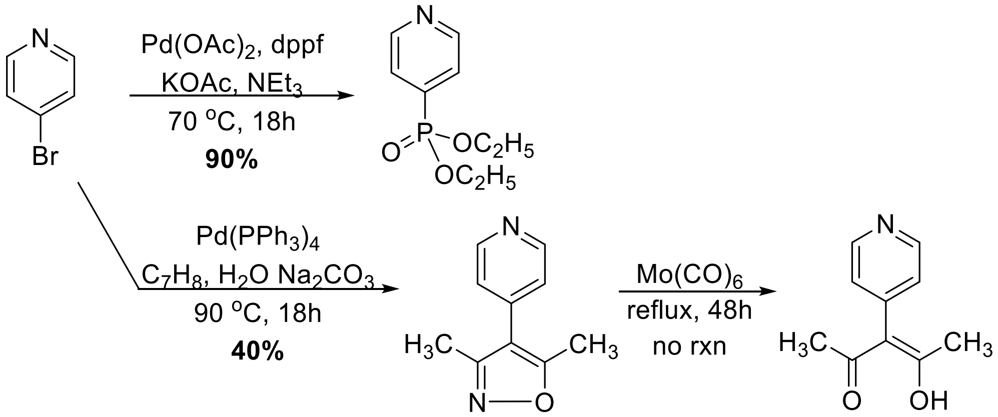

Scheme 2.5 Synthesis of **-PO(OC$_2$H$_5$)$_2$** and **-acac**

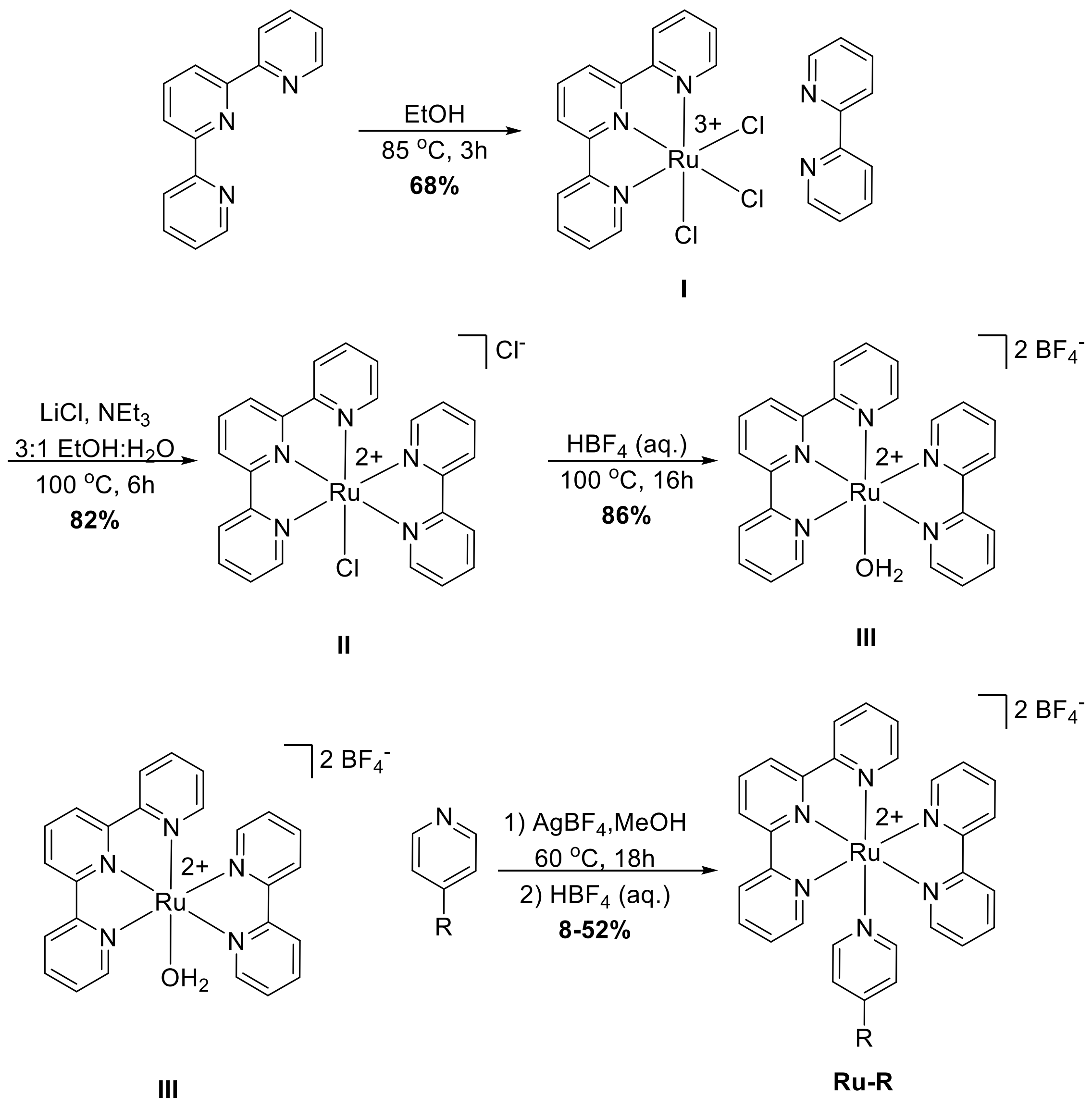

Scheme 2.6 Synthesis of **Ru-R** from commercial materials

yields. Although acetoacetonate (acac) has previously demonstrated good aqueous stability on TiO_2, it is also prone to auto-oxidation to form acetic acid and the corresponding ketone.[10] The acac could not be readily deprotected on the pyridine, and the isoxazole (**isox**) also undergoes decomposition when attempting to synthesize **Ru-acac** from **Ru-isox** as depicted in Scheme 2.7. The decomposition is observed by ^{1}HNMR when the resulting complex has additional sp^3 hydrogens from the resulting methylene group. As such, **Ru-acac** or **Ru-acetone** will not be included in the stability experiments.

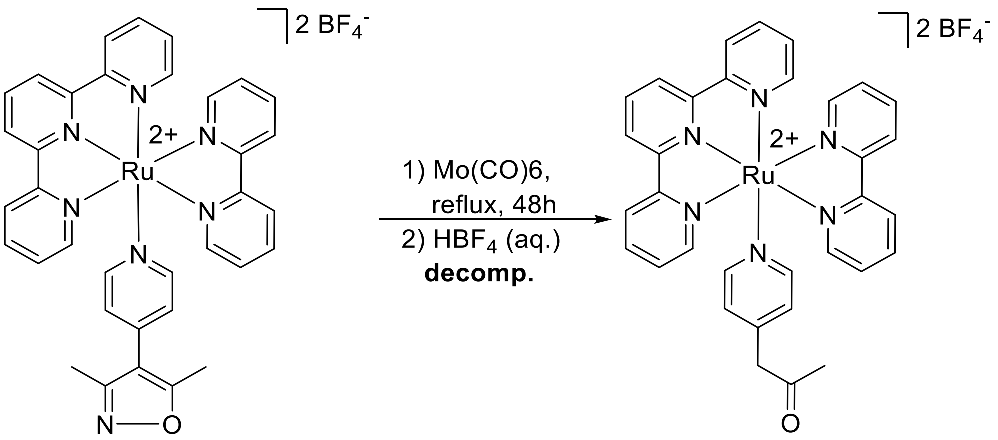

Scheme 2.7 Decomposition of **Ru-isox** to **Ru-acetone**

2.3 Adsorption Affinity and Aqueous Stability of Complexes

Titanium dioxide (TiO_2) is used as the model semiconductor for adsorption affinity and stability experiments with the **Ru-R** complexes. TiO_2 is ideal for these experiments because the semiconductor does not absorb light having $\lambda > 400$ nm. Therefore, strong visible light absorbers like **Ru-R** will not be interfered with by light absorption from TiO_2. As such, this property allows diffuse reflectance spectroscopy of modified films to be used to calculate the relative percentage of catalyst remaining on the electrode surface. TiO_2 is prepared through drop casting a crystalline anatase TiO_2 slurry onto clean fluorine-doped tin oxide (FTO) coated glass substrate that had been masked off with electrical tape. The TiO_2 thickness is controlled through blade coating onto FTO using the tape as the thickness template. Upon annealing, the films are opaque and white. The complexes **Ru-COOH**, **Ru-PO(OC$_2$H$_5$)$_2$**, and **Ru-CO(NHOH)** adsorb onto the TiO_2 by soaking the TiO_2 in a 0.5 mM solution of **Ru-R** at room temperature in the dark for 18 hours.

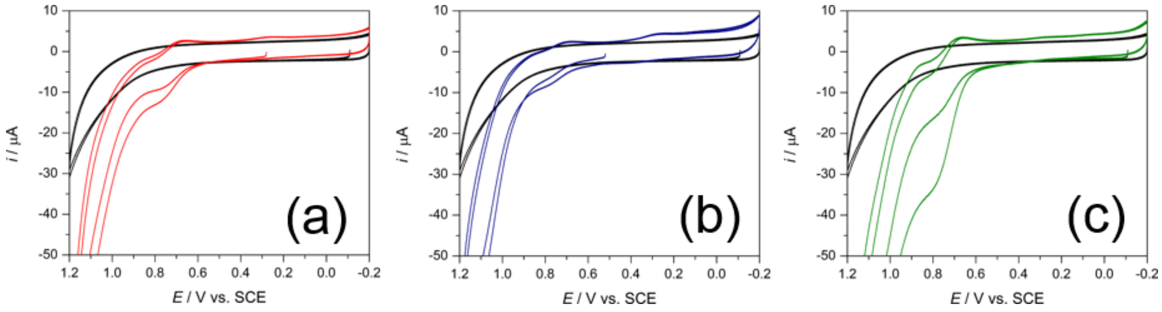

Figure 2.1 Cyclic voltammetry of **Ru-COOH** (a-red), **Ru-PO(OC$_2$H$_5$)$_2$** (b-blue), and **Ru-CO(NHOH)** (c-green) anchored to TiO_2 (bare-black) in 100 mM $TBAPF_6$ with CH_3CN at 20 mV s^{-1} with Pt CE and SCE RE

After 18 hours, the films are deep red relative to the pristine TiO_2. When the films are washed extensively with methanol and acetonitrile, no color change is observed for the modified films. This result suggests that the complexes are not simply physisorbed onto the electrode surface. UV-Vis spectroscopy of the resulting films demonstrates strong absorption of visible light consistent with the MLCT bands of **Ru-R** in solution as illustrated in Figure A.1. Cyclic voltammetry of the electrodes after modification reveals good adsorption to the electrode material (Figure 2.1). In all cases, the $Ru^{2+/3+}$ oxidation is observed at ~0.8 V vs. the saturated calomel electrode (SCE). Because the event is highly reversible for these complexes, bulk electrolysis can be used to closely approximate the surface coverage of the catalysts on the surface. By comparing the charge passed for the same modified and bare TiO_2 electrode, Faraday's equation can be employed to calculate the number of e^-'s required to completely oxidize or reduce the electrochemically active species on the surface. Since $Ru^{2+/3+}$ is a one e^- event, the surface coverage can be calculated according to the equation:

$$n = -\frac{\Delta Q}{F \times z} \tag{1}$$

Where n is the moles of catalyst on the surface, ΔQ is the change in number of electrons passed, F is Faraday's constant, and z is the number of electrons per reaction. The $Ru^{2+/3+}$ couple is thus used as the handle for quantifying the surface coverage of the different complexes. Electrolysis of the films before and after modification reveals the surface coverages summarized in Table 2.1 Surface coverage of **Ru-R** on TiO_2Table 2.1. These results show that **Ru-PO(OC_2H_5)$_2$** and **Ru-CO(NHOH)** are comparable in terms of surface coverage. They also suggest that both anchoring groups achieve higher surface coverages than **Ru-COOH**. This result is consistent with the reports from DSSC literature suggesting these two anchoring groups should bind more readily to TiO_2.[4,11]

Complex	Surface Coverage (nmole cm^{-2})
Ru-COOH	7
Ru-PO(OC_2H_5)$_2$	11
Ru-CO(NHOH)	12

Table 2.1 Surface coverage of **Ru-R** on TiO_2

After looking at the surface coverage, the pH stability of the various complexes are examined in pH 1.1, pH 7.0, and pH 10.0 using potassium phosphate as the "electrolyte" to imitate electrochemical conditions and ensure maximum ionic strength of the counterion. Diffuse reflectance UV-Vis spectra of the modified electrodes are recorded prior to soaking and then after soaking. The % change in reflectance corresponds to the amount of complex that remains on the surface after soaking in the aqueous solutions for 24 hours. The actual diffuse reflectance spectra of these films can be found in Figures Figure A.2, Figure A.3, and Figure A.4. The proportion of catalyst remaining on the TiO_2 surface after soaking is summarized in Table 2.2. There are a few notable results that stem from this experiment. First, **Ru-COOH** immediately diffuses away from the TiO_2 surface in all cases. In other words, no complex is present on the surface after <5 minutes evidenced by the coulometry. Second, **Ru-CO(NHOH)** exhibits significantly lower stability than has been previously reported.[4] The pyridine ligand may be dissociating from the **Ru** to form both pyridine and complex **III**. Despite this possibility, **Ru-PO(OC_2H_5)$_2$** still exhibits the highest stability in pH 1.1 and pH 7. This result corresponds reasonably well with the expected stability of the phosphonate anchors previously reported.[12] Based on the higher initial coverage and moderate stability in aqueous solutions, phosphonate anchoring groups are used as the anchor of choice for future applications.

pH	**% Ru-COOH**	**% Ru-PO(OC_2H_5)$_2$**	**% Ru-CO(NHOH)**
1.1	2	45	2
7.0	0	25	0
10.0	0	0	0

Table 2.2 Remaining **Ru-R** on TiO_2 after soaking at various pH

2.4 Synthesis and Characterization of [Ru] Water Oxidation Catalysts

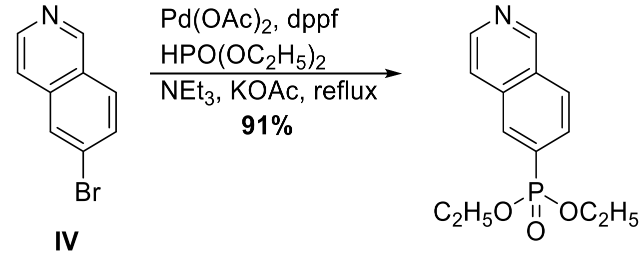

Scheme 2.8 Palladium cross-coupling to incorporate diethyl phosphonate on isoquinoline

After identifying the most stable anchoring group, the challenge then became

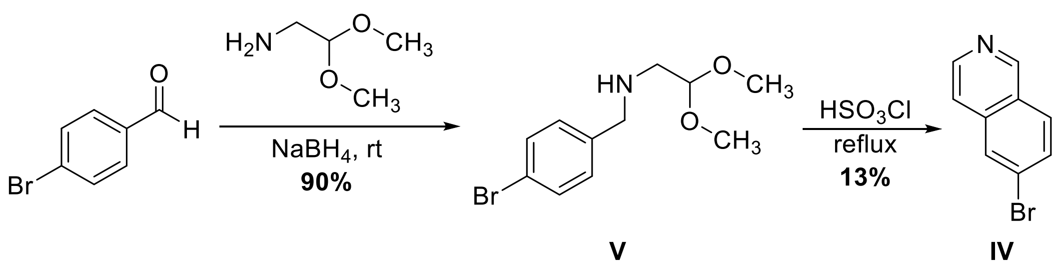

Scheme 2.9 Synthesis of intermediate **IV**

incorporating that functionality onto the best know WOC. In the case of **Ru**, the isoquinoline ligands are ideal sites for modification since the same cross-coupling reaction could be carried out to incorporate the phosphonate anchor (Scheme 2.8). However, 6-bromoisoquinoline (**IV**) is not commercially available. As such, the synthesis described in Scheme 2.9 is carried out to prepare **IV**. The preparation of intermediate **V** is high yielding and reacts quickly. The ring closing and rearomatization of **V** to form compound **IV** is much more challenging. This reaction must be performed under rigorously dry conditions, and chlorosulfonic acid is added to a liquid addition funnel under a positive pressure of N_2 with a glass pipet. Because of chlorosulfonic acid's extremely corrosive nature, it reacts violently with stainless needles and plastic syringes. In addition to being extremely water sensitive, this reaction is sluggish at best and results in very low conversion of the starting

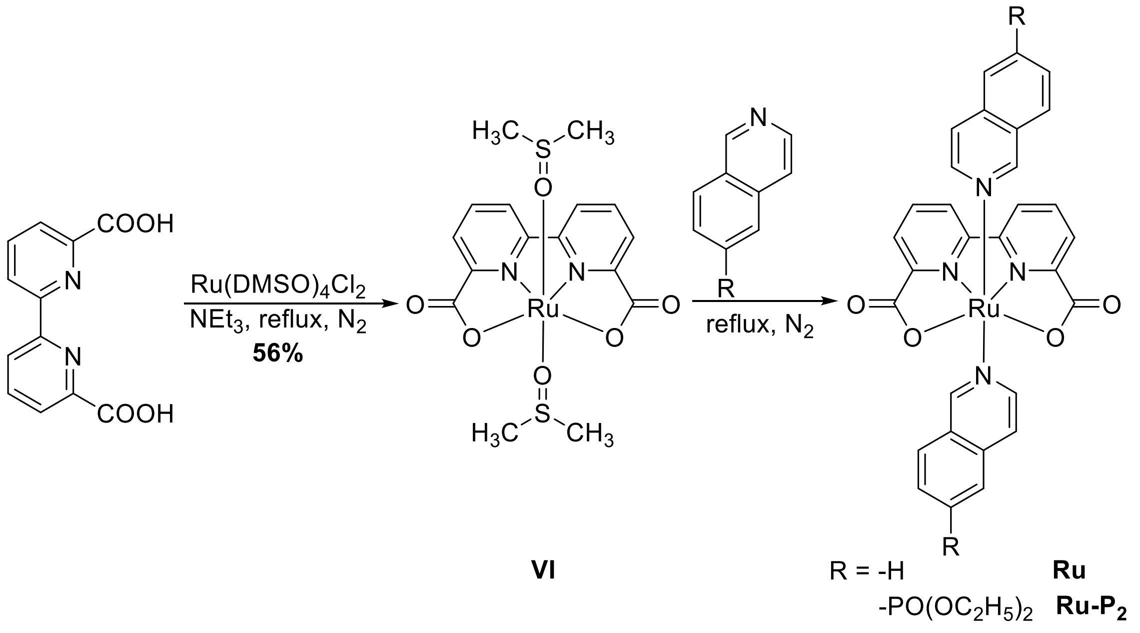

Scheme 2.10 Synthesis of **Ru** and **Ru-P$_2$**

material **V** to **IV**.

With the modified isoquinoline in hand, the attention focuses on preparing the **Ru** complexes. **Ru** and **Ru-P₂** are prepared according to Scheme 2.10.[6] In the first step of the synthesis, 2,2’-bipyridine-6,6’-dicarboxylic acid is deprotonated with two equivalents of NEt_3. Upon dissolution, $Ru(DMSO)_4Cl_2$ is added to the reaction and the yellow solution is degassed to prevent the Ru from becoming reoxidized. The reaction is then heated to reflux under N_2 and turns brown. After ~1 hour at reflux the desired complex **VI** precipitated from the reaction mixture. Refluxing **VI** in degassed methanol with two equivalents of isoquinoline or diethyl 6-isoquinolylphosphonate yields the desired **Ru** and **Ru-P₂** respectively in good yield. The complexes are stable enough that they can be purified by column chromatography using polar solvent mixtures such as 1:1 methanol and dichloromethane.

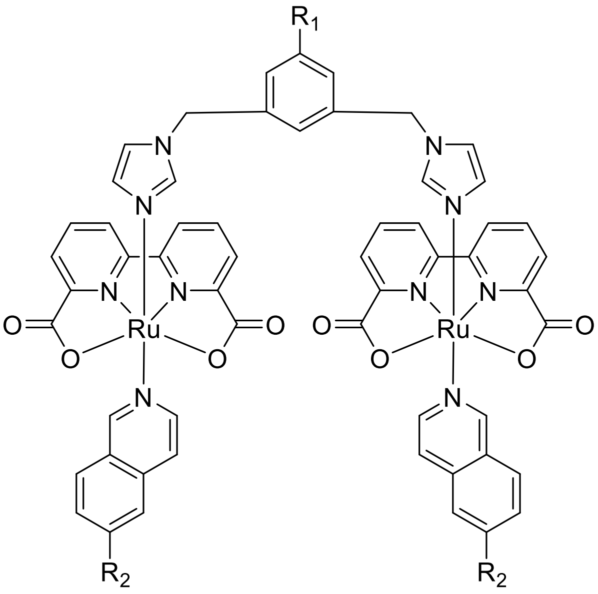

$R_1 = R_2 = -H$ **Ru$_2$**
$R_1 = -H$ $R_2 = -PO(OC_2H_5)_2$ **Ru$_2$-P$_2$**
$R_1 = -PO(OC_2H_5)_2$ $R_2 = -H$ **Ru$_2$-P**

Scheme 2.11 Targeted **Ru$_2$** complexes

In addition to **Ru** and **Ru-P₂**, binuclear analogs are also prepared. The targeted complexes are depicted in Scheme 2.11. The bridging ligands 1,5-bis(*N*-methylimidazolyl)-benzene (**VII**) and diethyl 1,5-bis(*N*-methylimidazolyl)-phenyl-3-phosphonate (**VIII**) are synthesized according to Scheme 2.12 and Scheme 2.13 respectively. The coupling reaction to prepare both **VII** and **VIII** are rapid reactions and result in good yields of the corresponding ligand. For ligand **VIII**, the limiting step proves to be the palladium cross-coupling with diethyl phosphite, likely because the diol and the

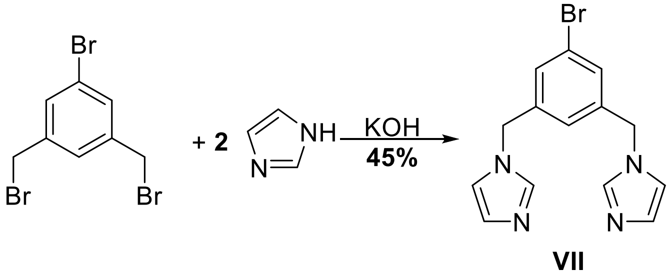
VII

Scheme 2.12 Synthesis of **VII**

bis-imidazole are both capable of coordinating and inhibit the reaction.

Ru2, **Ru2-P2**, and **Ru2-P** are all readily prepared by the synthesis described in Scheme 2.14. In previous examples of this synthesis, the axial ligand is coordinated first. However, when picoline is replaced with isoquinoline, the basicity of the coordinating nitrogen increases, and di-coordination of isoquinoline is the primary product of the reaction. Instead, it is necessary to preform the diruthenium complex through coordination of the desired bridging ligand first. This reaction proceeded in excellent yield, and although

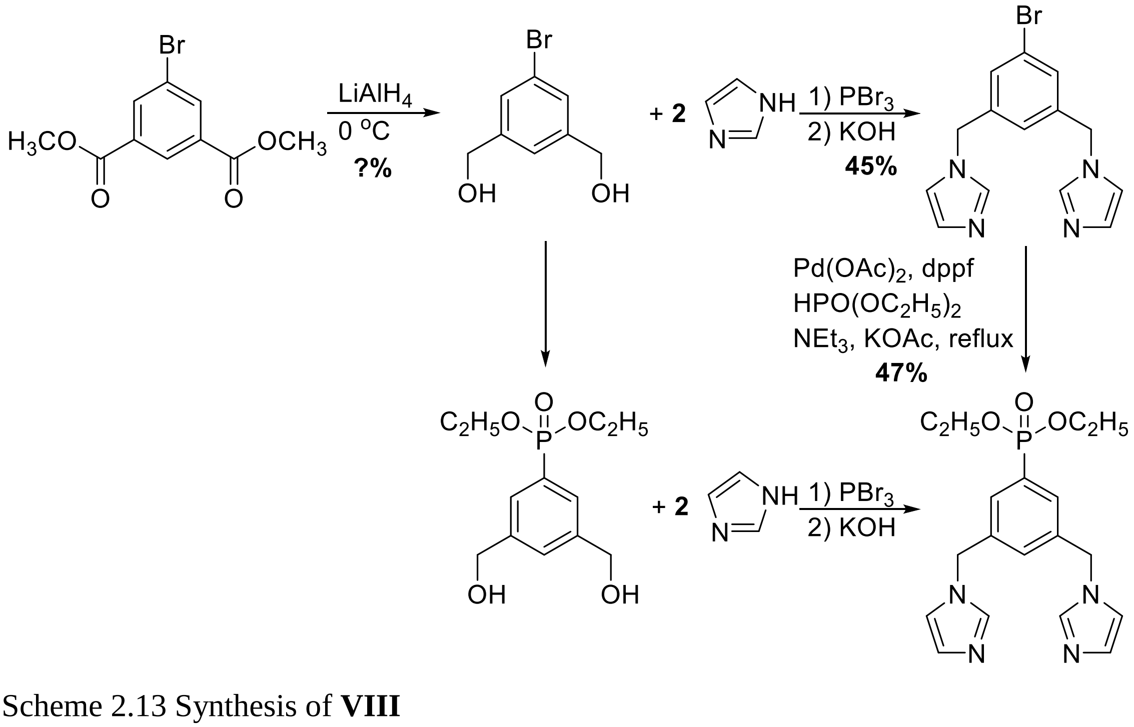

Scheme 2.13 Synthesis of **VIII**

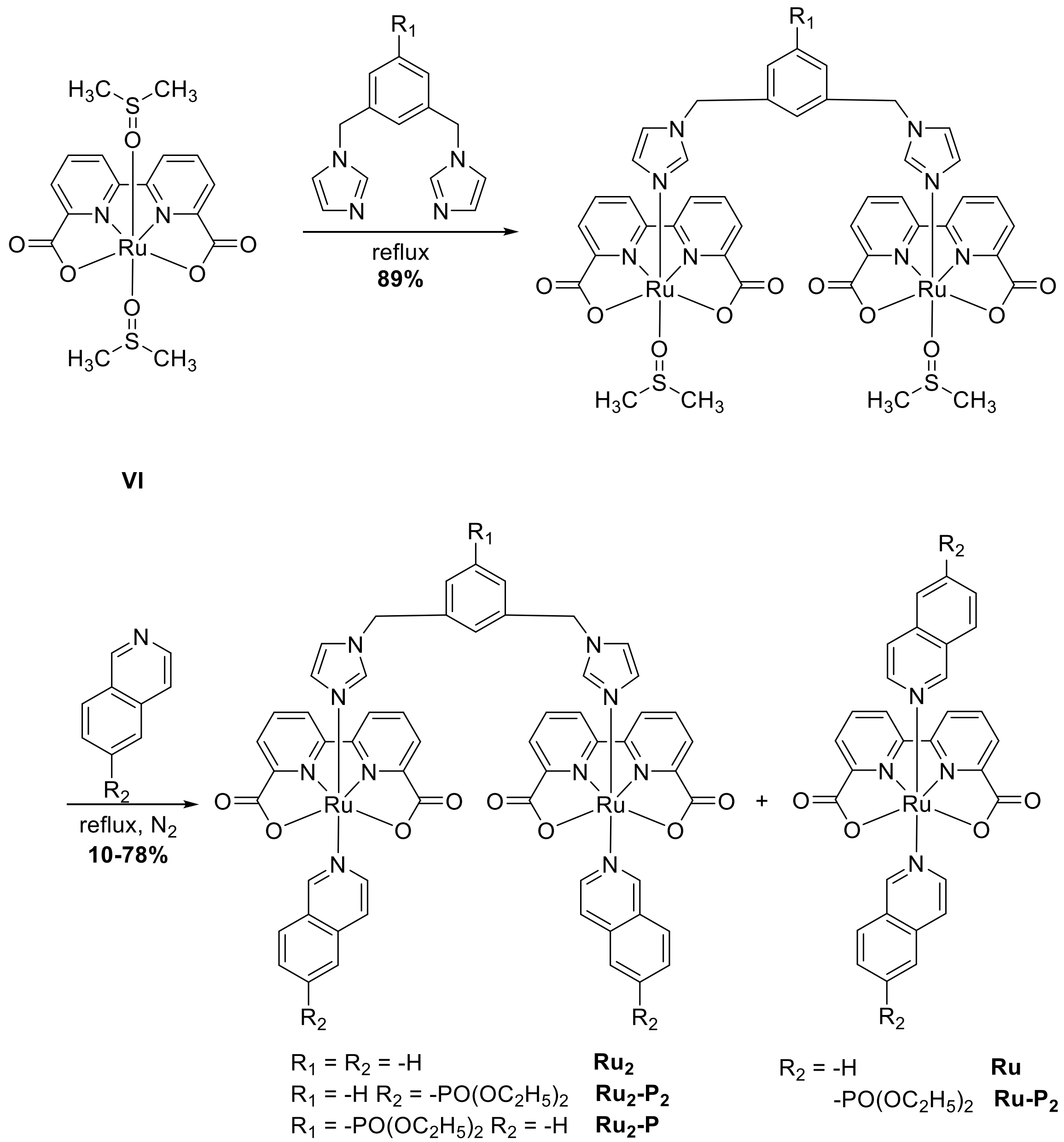

Scheme 2.14 Synthesis of dinuclear **Ru$_2$-R** complexes

some starting material remains in the reaction mixture, there is no good way to purify this complex without jeopardizing the bound solvent ligands on the complex. As a result, when the complex is refluxed in the presence of the desired isoquinoline ligand, the reaction is rapid, and yields a mixture of the desired product and the di-coordinate **Ru** or **Ru-P$_2$** from above. The mixture is easily separated and purified by column chromatography on silica gel since the di-nuclear species is much larger and flexible it has a much lower retention factor than the mono-nuclear complex (R_f = 0.1 vs. 0.5 respectively). In the future, this synthesis could be useful for synthesizing both the mono-nuclear and di-nuclear ruthenium complexes as opposed to two separate syntheses for both complexes.

Since **Ru** is said to undergo a dimeric transition state facilitated by π -π stacking of the isoquinoline, there is some concern the phosphonate substituents might sterically inhibit that interaction. Therefore, homogeneous water oxidation is compared with all of the synthesized complexes as illustrated in Figure 2.2. Under unoptimized conditions, the complexes **Ru-P$_2$** and **Ru$_2$-P$_2$** exhibit diminished rate and duration of reactivity. As expected, **Ru$_2$-P** exhibits little loss of reactivity relative to **Ru$_2$**. This result supports the idea that the phosphonate groups hinder the π -π interaction that facilitates water oxidation. The results from the reactivity screen are summarized in Table 2.3. The maximum turnover number is determined by the moles O_2 produced per mole of catalyt after spiking $Ce(NH_4)_2(NO_3)_6$ results in no additional oxygen evolution (~1 hour). Additionally, the

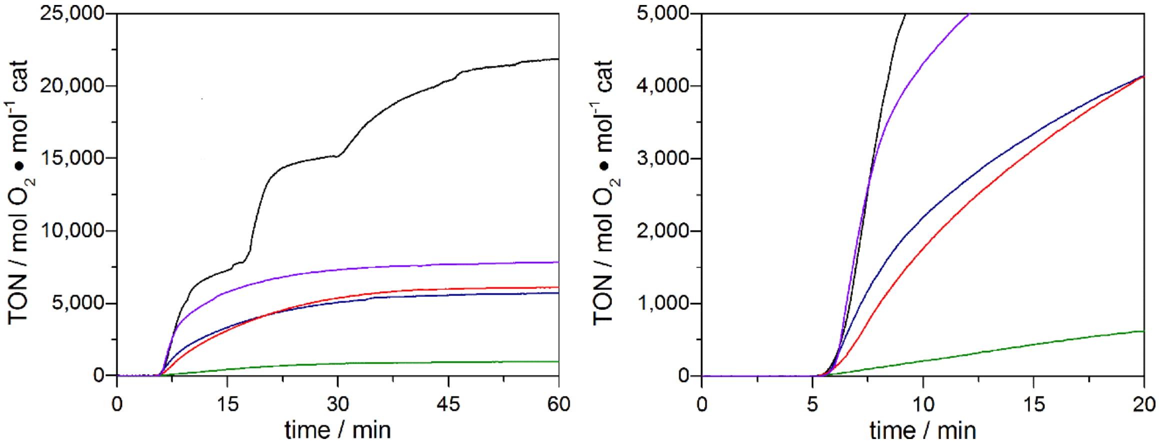

Figure 2.2 Homogeneous water oxidation with **Ru** (black), **Ru-P$_2$** (red), **Ru$_2$** (blue), **Ru$_2$-P$_2$** (green), **Ru$_2$-P** (purple) in the presence of $Ce(NH_4)_2(NO_3)_6$

Catalyst	TON (mol O_2 mol^{-1} cat)	TOF (mol O_2 mol^{-1} cat s^{-1})
Ru	22,500	33.3
Ru-P$_2$	5,100	6.7
Ru$_2$	5,000	8.3
Ru$_2$-P$_2$	800	0.7
Ru$_2$-P	7,400	33.3

Table 2.3 Water oxidation with $Ce(NH_4)_2(NO_3)_6$

initial turnover frequency is determined after the first injection of $Ce(NH_4)_2(NO_3)_6$. Although the decrease in reactivity is worrisome, once anchored to a semiconductor surface, the catalysts should be forced (especially in the case of the dimers) to interact with other surface bound catalysts.

Along with homogeneous reactivity, it is important to determine the electrocatlytic onset potential for water oxidation. In the past, **Ru** has demonstrated strong electrocatlalytic waves at 1.26 V vs. NHE.[6] Adding electron-donating character to the complexes via the phosphonate substituents is expected to decrease the oxidation potentials for the complexes. However, the impact on redox events in non-aqueous solutions are minimal for this series of complexes. The CVs can be found in Figure A.5, but the onset potentials in wet CH_3CN and other redox events are summarized in Table 2.4. The high electrocatalytic current for this series of complexes suggests that the catalysts should be well suited for photoelectrochemical water oxidation once anchored to the light absorbing semiconductor.

Catalyst	**$Ru^{2+/3+}$**	**$Ru^{3+/4+}$**	**E_{on} / V RHE**	**E_{cat} / V RHE**
Ru	0.43	0.86	0.75	1.17
$Ru-P_2$	0.44	0.97	0.82	-
Ru_2	0.09*, 0.43	0.81	0.70	1.16
Ru_2-P_2	0.12, 0.36	0.86	0.60	1.29
Ru_2-P	0.32	0.80	0.72	1.13

Table 2.4 Electrochemical events for **Ru** catalysts (*oxidation overlaps with 0.43 V couple)

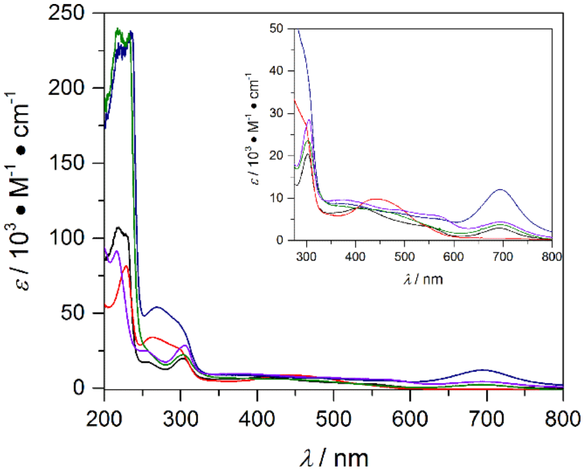

Figure 2.3 UV-Vis of **Ru** (black), **$Ru-P_2$** (red), **Ru_2** (blue), **Ru_2-P_2** (green), and **Ru_2-P** in CH_3CN

As is demonstrated previously with the model complexes, the MLCT bands of these ruthenium complexes have large molar absorptivities. This spectral feature makes UV-Vis spectroscopy a useful handle for characterizing any species present on the electrode surface after photoelectrochemistry for these catalysts. Figure 2.3 shows the UV-Vis spectra of the prepared catalysts. It is interesting to note that, with the exception of **Ru-P$_2$**, all of the catalysts exhibit a ligand field *d-d* transition at approximately 700 nm. At 263 nm and 269 nm, **Ru-P$_2$** and **Ru$_2$** respectively exhibit an additional peak. These peaks are most likely different MLCT transitions that are less intense and are blue-shifted for the other compounds (therefore obscured in the large π -π* transitions).[13] For the dimeric species, **Ru$_2$-P$_2$** and **Ru$_2$-P**, the peak at 700 nm will be useful for ensuring adsorption to the semiconductor electrode. For **Ru-P$_2$**, the peak at 450 nm will be useful for monitoring adsorption to the semiconductor surface.

2.5 Photoelectrochemistry of [Ru] on Various Semiconductors

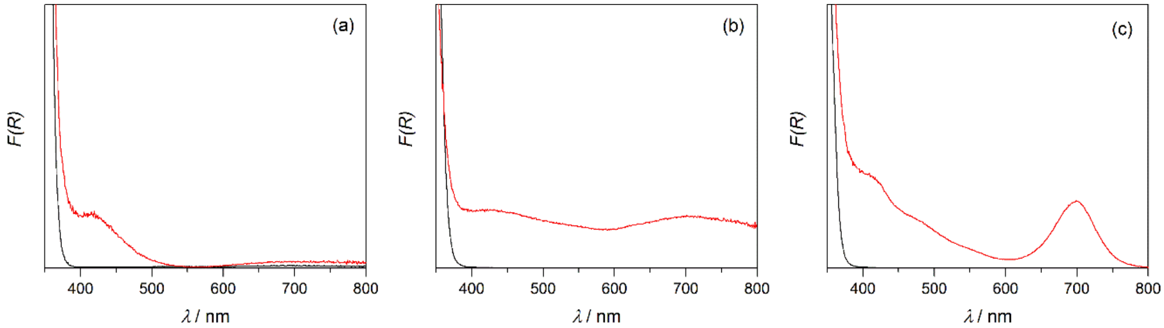

Figure 2.4 Diffuse reflectance UV-Vis of **Ru-P$_2$** (a), **Ru$_2$-P$_2$** (b), and **Ru$_2$-P** (c) on TiO$_2$ (red) compared to bare TiO$_2$

With a good understanding of the catalytic capabilities of the modified ruthenium catalysts, the catalysts are adsorbed onto TiO$_2$ electrodes. The TiO$_2$ electrodes are soaked at room temperature in the dark for 72 hours to ensure maximum surface coverage. Heating the solutions to accelerate adsorption resulted in a stark color change from brown to orange for the dimeric species. It is speculated that under heating the dimeric catalysts equilibrate to the mono-nuclear complex **Ru** or **Ru-P$_2$**. Therefore, it is imperative that these complexes are adsorbed onto the semiconductors of interest at room temperature.

Rinsing the films thoroughly after modification reveals no apparent change in the films coverage (i.e. no coloration of the rinsing solution or change of the film color). This result suggests that the catalysts are not simply physisorbed to the TiO_2 surface. In further support of that, when complexes without anchors are soaked with different semiconductors, the catalyst is easily rinsed from the surface because it is physisorbed. UV-Vis spectroscopy confirms that the desired catalysts are present of the semiconductor surface, as depicted in Figure 2.4. Furthermore, dark linear sweep voltammetry (LSV) confirms the electrochemical presence of the desired complexes on the TiO_2 surface. As illustrated in Figure 2.5, the catalysts exhibit significantly different electrochemical behaviors. For **Ru-P$_2$**, there are two small sharp peaks evident on the TiO_2 electrode in the dark suggesting the $Ru^{2+/3+}$ and $Ru^{3+/4+}$. However, for **Ru$_2$-P$_2$**, there are multiple broad, low current peak. The peak appears to resemble several separate peaks coalescing. In the case of **Ru$_2$-P**, there are two high-current peaks and a large increase in dark current. The unique character of each peak and its correlation to the solution species supports the notion that the desired catalysts are indeed present on the TiO_2 surface. In conjunction with these results, the open circuit voltage of the modified electrodes shift to coincide with the open circuit potentials of the corresponding complexes in solution. This result suggests that the Fermi level (E_f) is equilibrating with the molecular species on the surface instead of the solution's redox potential.

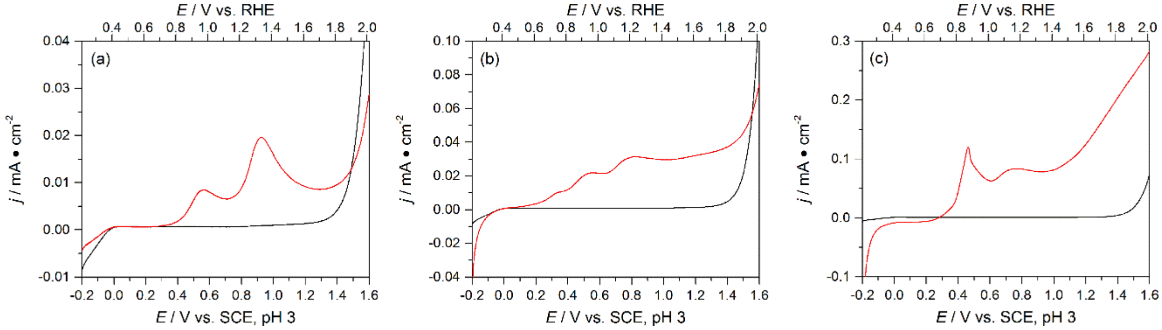

Figure 2.5 Dark LSV of **Ru-P$_2$** (a), **Ru$_2$-P$_2$** (b), **Ru$_2$-P** (c) in red compared to bare TiO_2 (black) in pH 3 Na_2SO_4

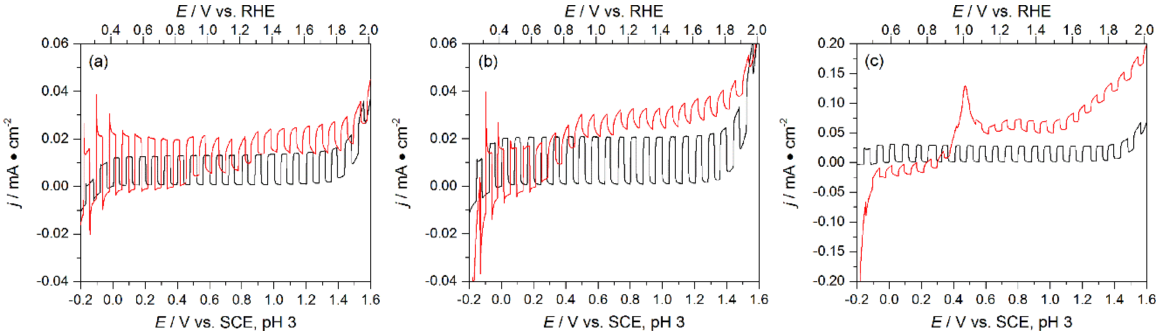

Figure 2.6 Chopped light LSV traces of **Ru-P$_2$** (a), **Ru$_2$-P$_2$** (b), **Ru$_2$-P** (c) in red compared to bare TiO_2 (black) in pH 3 Na_2SO_4

Under back illumination, the LSV traces of the modified electrodes reveal increased photocurrent for **Ru-P$_2$** at lower potentials and diminished photocurrent at higher potentials relative to bare TiO_2 as evidenced in Figure 2.6 (a). This result is surprising because all of the catalysts should increase the rate of electron transfer between the semiconductor and solution (i.e. water oxidation). Furthermore, **Ru-P$_2$** is not expected to be active on the electrode surface because the dimeric transition state should be hard to form when anchored to an electrode surface. A possible explanation for this observation is that the catalyst undergoes an alternative mechanism that is slower catalytically but still faster than the semiconductor electrode. This change in mechanism has precedence in the literature where Sun and co-workers have demonstrated that switching between isoquinoline and picoline as axial ligands results in a change of mechanism that also decreases the rate of catalysis.[6] Sun and co-workers have also demonstrated that when the picoline analog is anchored to a dye-sensitized solar cell, the catalyst is still catalytically active and they speculate a mononuclear mechanism as well.[14]

As for the binuclear catalysts, these results suggest that the binuclear species are preventing the semiconductor surface from catalyzing the reaction faster. One possible explanation for this observation is the catalysts traps holes at the semiconductor surface. Another, possibly better, explanation is that because the catalyst exhibits reversible redox states the electrons in the TiO_2 conduction band could be transferring to the molecular catalysts more quickly than the catalyst can turn over water oxidation. Although the conduction band of TiO_2 is ideal for accepting electrons from photoexcited organic dyes, the potential energy difference between the TiO_2 conduction band and the molecular catalyst's LUMO is quite large. Because the Fermi level of the semiconductor initially equilibrates to the molecular species bound on the surface, as evidenced by the initial open circuit voltage of the modified electrode, the depletion width may not be sufficient to prevent back electron transfer to the molecular catalyst. This possibility is supported by the apparent induction time visible in the chopped light LSVs. For bare TiO_2 the photocurrent is square, such that when the surface is illuminated there is little transient photocurrent and rapid saturation of current. However, for the modified TiO_2, there is a prolonged increase in photocurrent evident at higher potentials. This result suggests that the catalysts are being slowly activated by the TiO_2 as opposed to instantaneously beginning to oxidize water as bare TiO_2 does, and is also evident through slow saturation of photocurrent at 1.23 V vs. RHE for the modified TiO_2 electrodes (see Figure A.6).

In order to examine the impact of electronic structure, other semiconductors are explored to reduce the potential energy different between the semiconductor conduction band and the ruthenium catalysts. WO_3 and $CuWO_4$ are explored as alternative semiconductors because WO_3 has the highest hole mobility[15] and $CuWO_4$ has a similar conduction band potential energy but has an even smaller band gap through a raised valence band potential energy as illustrated in Figure 2.7.[16]

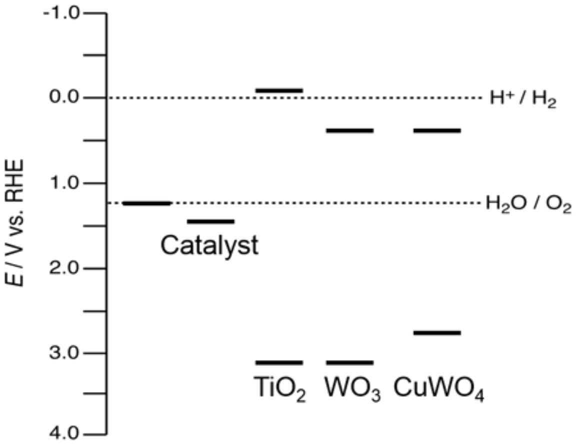

Figure 2.7 Band structure diagram of various semiconductors for photosensitizing **Ru** complexes

When **Ru-P$_2$**, **Ru$_2$-P$_2$**, and **Ru$_2$-P** are anchored to WO_3, the onset of photocurrent appears earlier but is accompanied by increased transient photocurrent as depicted in Figure 2.8. The transient photocurrent occurs over the potentials associated with the corresponding ruthenium redox events. Therefore, the most likely explanation for this observation is rapid solar oxidation of the ruthenium species followed by decay back to the semiconductor's saturated photocurrent density. In addition to the increase in transient photocurrent, there is also a shift in onset potential for **Ru-P$_2$** and **Ru$_2$-P$_2$**. The shift in onset potential indicates that the catalysts are operating at much lower overpotentials relative to WO_3's active surface sites. For **Ru-P$_2$** and **Ru$_2$-P$_2$**, the Faradaic efficiency at low overpotentials could be compared with bare WO_3 to ensure that the earlier onset of photocurrent is related to water oxidation as opposed to photochemical oxidation of the molecular species. Furthermore, the saturated photocurrent is significantly reduced relative to the bare WO_3. The catalysts is clearly operating much more slowly than the bare WO_3 when transferring electrons into solution. The decrease in photocurrent is similar to that reported by Zhong et al. on WO_3.[17] However, the decrease in photocurrent could be a result of increased selectivity towards water oxidation and while the rate of electron transfer to solution is diminished, the overall efficiency is better and the rate of water oxidation could still be faster. To further confirm this possibility, solar water oxidation at the thermodynamic potential for water oxidation should be completed as well for **Ru-P$_2$** and **Ru$_2$-P$_2$**.

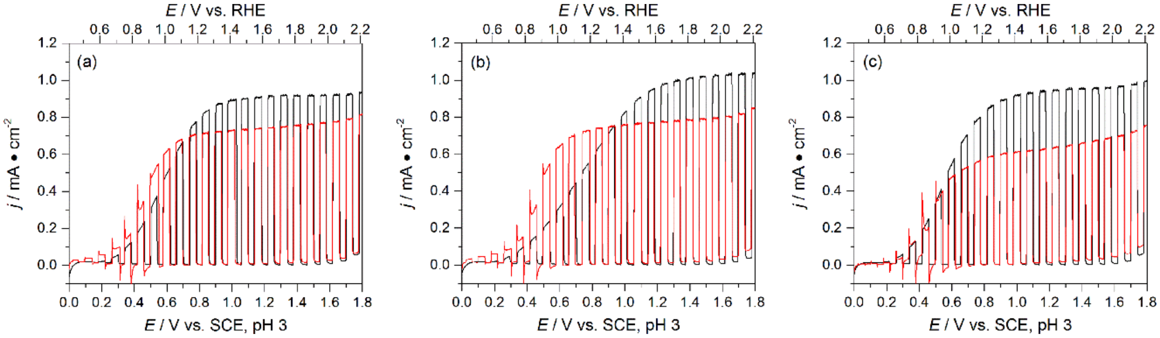

Figure 2.8 Chopped light LSV traces of **Ru-P$_2$** (a), **Ru$_2$-P$_2$** (b), **Ru$_2$-P** (c) in red compared to bare WO_3 (black) in pH 3 Na_2SO_4

The results become more confusing when compared to the linear sweep voltammetry of the catalysts on $CuWO_4$. $CuWO_4$ has a smaller band gap than TiO_2 and WO_3. As mentioned above, the decrease in bandgap should result in increased hole population at the surface of the semiconductor. The results of this screen suggest that the increase in hole influx for this particular series of catalysts has some impact on the increase in photocurrent since the relative % increase in photocurrent between TiO_2, WO_3, and $CuWO_4$ for **Ru$_2$-P$_2$** and **Ru$_2$-P** gradually increase as light absorption increases as summarized in Table 2.5. The opposite is observed for **Ru-P$_2$**. For **Ru-P$_2$**, the % increase in photocurrent decreases as light absorption increases as found in Figure 2.9 (a).

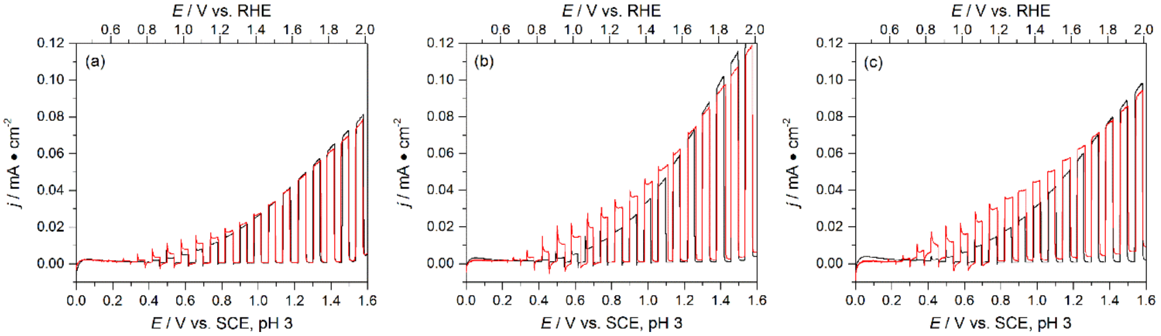

Figure 2.9 Chopped light LSV of **Ru-P$_2$** (a), **Ru$_2$-P$_2$** (b), **Ru$_2$-P** (c) in red compared to bare $CuWO_4$ (black) in pH 3 Na_2SO_4

Catalyst	**TiO_2 (% increase)**	**WO_3 (% increase)**	**$CuWO_4$ (% increase)**
Ru-P$_2$	67%	-14%	17
Ru$_2$-P$_2$	0%	-22%	66
Ru$_2$-P	-33%	-32%	96

Table 2.5 Increase in photocurrent for different semiconductors when modified with **Ru** catalysts at saturated potentials

One of the most likely rationales for these trends is the selectivity of WO_3 and the oxidation potentials associated with each complex. For WO_3, the valence band is essentially at the same electrochemical potential as TiO_2. As such, the increase is still observed for **Ru-P$_2$**. However, the inefficiency inherently associated with WO_3 leads to an uncertain % increase in photocurrent related to water oxidation for each complex. The only trace evidence that the water oxidation rate is being improved is the earlier onset of photocurrent and steeper slope towards saturation.

When the band gap is compressed further for $CuWO_4$, the valence band is now shifted up further. Although the valence band position may have a significant impact on the ability to oxidize the complexes, the valence band is still at 2.8 V vs. NHE. As a result, this energy should be more than enough potential energy to activate the different complexes. But, since **Ru-P$_2$** is most likely undergoing a secondary reaction mechanism because it most likely is unable to form the necessary dimeric transition state, the E_{cat} oxidation potentials for this reaction may be significantly higher. Although it is unlikely that the potentials shift to greater than 2.8 V vs. NHE, this explanation is still a possible reason for the loss of photocurrent. The more likely explanation is that in the case of $CuWO_4$, hole transfer to solution is regulated by an additional electronic state in the middle of the band gap (a mid-gap state). The mid-gap state for $CuWO_4$ has been demonstrated to limit the rate of catalysis for $CuWO_4$.[18] As such, it is possible that the redox potential for **Ru-P$_2$** is now shifted below that state and can no longer be activated by $CuWO_4$. On the other hand, the mid-gap state could be very close to the redox potentials for **Ru$_2$-P$_2$** and **Ru$_2$-P**. As a result, these catalyst could still be photoactivated by the $CuWO_4$ under illumination. To probe this idea further, Fe_2O_3 could also be used as the light absorber since there is similarly strong evidence for mid-gap states limiting its catalytic performance as well.[19]

Comparison of **Ru$_2$-P$_2$** and **Ru$_2$-P** on WO_3 and $CuWO_4$ reveal contradictory results. For example, based on homogeneous water oxidation rates, **Ru$_2$-P** should exhibit higher rates of catalysis when anchored to the electrode surfaces. For WO_3, this outcome is not the case. However, for $CuWO_4$, **Ru$_2$-P** demonstrates slightly higher photocurrent densities than **Ru$_2$-P$_2$**. This result suggests that the rate of holes reaching the surface and efficiency of electron transfer are separate, important factors for governing the ability of the semiconductors to activate the molecular catalyst on the surface. For example, **Ru$_2$-P$_2$** is

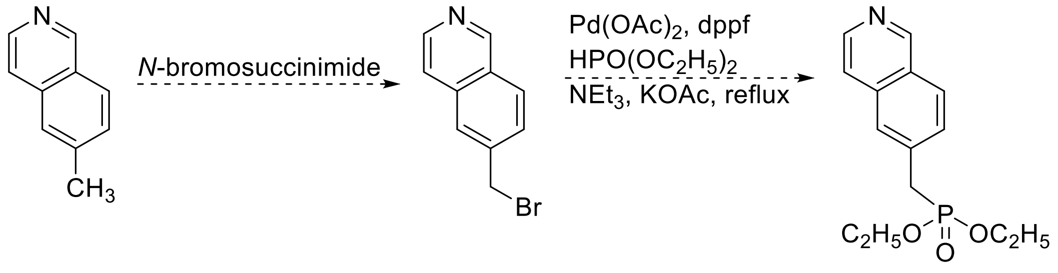

Scheme 2.15 Proposed synthesis of unconjugated isoquinolyl phosphonate

conjugated between the semiconductor and the ruthenium centers. As a result electron transfer efficiency should be more efficient than **Ru$_2$-P**, which is not conjugated to the semiconductor. Therefore, if the rate of holes reaching the surface is low or regulated (such as $CuWO_4$), then the faster molecular catalyst should improve the photocurrent more significantly. However, if the rate of holes reaching the surface is sufficiently fast, then efficiency of electron transfer to the semiconductor becomes most important. The main takeaway from these experiments should be that conjugating the reactive center to the semiconductor is better for improving the rate of photocatalysis, but non-conjugated complexes are still capable of transferring electrons. To better probe this hypothesis, it would be prudent to examine the impact of a methylene spacer between the isoquinoline and the phosphonate group. This compound could be synthesized according to Scheme 2.15.

2.6 Conclusions

This chapter has laid the foundation for the rest of this thesis. Herein, a sufficiently pH stable anchor, diethyl phosphonate, has been determined through the use of a model, polypyridyl ruthenium complex. This chapter is pivotal towards designing future ligand scaffolds with the goal of anchoring molecular species to semiconductor light absorbers. Furthermore, this chapter serves as an initial proof of principle that molecular water oxidation catalysts are successfully anchored to semiconductor electrodes and exhibit increased reactivity under illumination. In addition to this proof of principle, the work with **Ru-P$_2$**, **Ru$_2$-P$_2$**, and **Ru$_2$-P** on various semiconductors demonstrates the fickle nature of this research from the standpoint that each unique system may or may not function as desired depending on the selection of semiconductors and molecular catalysts targeted.

2.7 Experimental Methods

General Methods

All reaction were carried out under N_2 unless otherwise stated. Dry solvents were typically not necessary for most reactions. However, where stated, solvents were dried according to standard procedures. All other materials were obtained from commercial sources, and used as purchased. **Ru-R** complexes were prepared according known procedures.[10] $Ru(DMSO)_4Cl_2$, $Ru(terpy)Cl_3$, $Ru(terpy)(bpy)Cl_2$, 2,2'-bipyridyl-6,6'-dicarboxylic acid (bpa), $Ru(bpa)(DMSO)_2$, 5-bromo-(1,3-phenylene)dimethanol, and 1,3-

bis(*N*-methylimidazolyl)benzene (bmim) were synthesized according to known procedures. [6,8,9,20,21,22] Column chromatography was performed using standard 200 mesh silica gel. Elemental analyses were performed by Atlantic Microlab, Inc. for C, H, and N determinations. NMR spectra were recorded in $CDCl_3$, CD_6SO, or CD_3OD using a Varian MR400 at 400 MHz. Electrospray ionization mass spectra were collected on a Micromass LCT TOF MS through a Waters 1525 GC. UV/Visible/NIR spectroscopy was performed on an Agilent CaryWin 5000.

Synthetic Procedures

6-bromoisoquinoline

Dissolved 5.0 g (19.2 mmol) N-(4-bromobenzyl)-2,2-dimethoxyethanamine in 50 mL dry CH_2Cl_2. Cooled solution to 0 °C and added chlorosulfonic acid (7.0 mL, 105 mmol) in 12 mL dry CH_2Cl_2 dropwise to the stirring mixture in five minutes. The resulting cloudy green solution was heated to 50 °C overnight in air. After 30 minutes the reaction turned amber orange. The reaction was cooled to room temperature and diluted with solid ice. The cold stirring solution was then neutralized carefully with sat. $NaHCO_3$. The layers were then separated and the aqueous phase was extracted two additional times with CH_2Cl_2. The combined organic layers were dried with Na_2SO_4, filtered, and concentrated. The red oil (505 mg, 13% yield) that remained was the carried onto subsequent steps without further purification. ^{1}HNMR($CDCl_3$, ppm): 9.21 (1H, s), 8.53 (1H, d), 7.99 (1H, s), 7.82 (1H, d), 7.67 (1H, m), 7.55 (1H, d); ESI-MS$^+$: 208.0 m/z

Diethyl 6-isoquinolylphosphonate

Added 10 mg $Pd(OAc)_2$ (0.089 mmol), 81 mg dppf (0.146 mmol), 38 mg KOAc (0.387 mmol) to a two neck flask. The headspace was purged with N_2 for 10 minutes. After purging, the solids were dissolved in 12 mL THF, NEt_3 (0.68 mL, 4.88 mmol) was added, and the solution heated to 65 ^oC under N_2 for 10 minutes. Diethyl phosphite (0.48 mL, 3.73 mmol) and 6-bromoisoquinoline (1.0 g in 3 mL THF, 4.81 mmol) were added to the red orange solution. The reaction was refluxed overnight. A precipitate formed over the course of the reaction. The reaction was then cooled to room temperature and concentrated. The crude product was dissolved with 50 mL CH_2Cl_2 and washed with sat. $NaHCO_3$ (~30 mL). After the layers were separated, the aqueous layer was washed with CH_2Cl_2 (2x 50 mL). The combined organic layers were washed with brine, dried with Na_2SO_4, filtered, and concentrated *in vacuo*. The resulting brown oil was purified by column chromatography on silica using 3-5% methanol in dichloromethane. Purification resulted in a brown oil (901 mg, 91% yield). ^{1}HNMR($CDCl_3$, ppm): 9.31 (1H, s), 8.61 (1H, s), 8.38 (1H, d), 8.04 (1H, m), 7.88 (1H, t), 7.72 (1H, s), 4.14 (4H, m), 1.32 (6H, m); ^{13}CNMR(ppm): 152.50, 144.04, 134.80, 132.32, 131.71, 129.86, 128.04, 127.90, 121.00, 62.51, 16.38; ^{31}PNMR(ppm): 16.98; ESI-MS$^+$: 266.1 m/z

5-bromo-1,3-di(bromomethyl)benzene

Suspended 5-bromo-(1,3-phenylene)dimethanol (579 mg, 2.67 mmol) in 50 mL dry CH_2Cl_2. The solution was cooled to 0 ^oC, and PBr_3 (0.53 mL, 5.60 mmol) was added dropwise over several minutes. The reaction was warmed to room temperature and stirred under N_2 overnight. The reaction was quenched by cooling to 0 ^oC and carefully adding 50 mL sat. $NaHCO_3$. The layers were then separated, and the aqueous layer was washed with additional CH_2Cl_2 (2x 50 mL). The combined organic layers were dried with Na_2SO_4, filtered, and concentrated *in vacuo*. The resulting white solid (627 mg, 68% yield) was the desired product and carried onto the next step without additional purification. ^{1}HNMR($CDCl_3$, ppm): 7.59 (2H, d), 7.50 (1H, s), 4.67 (4H, s); ^{13}CNMR(ppm): 141.51, 132.12, 129.60, 32.92; ESI-MS$^+$: 342.8 m/z

5-bromo-1,3-bis(*N*-methylimidazolyl)benzene

Deprotonated imidazole (249 mg, 3.66 mmol) with 255 mg KOH (3.84 mmol) suspended in 100 mL acetonitrile with 5 mL H_2O. The solution was stirred for 1 hour at room temperature, upon which time the solid 5-bromo-1,3-di(bromomethyl)benzene (627 mg, 1.83 mmol) was added to the reaction. The reaction was stirred under ambient conditions overnight, and concentrated *in vacuo*. The resulting yellow residue was taken into 50 mL CH_2Cl_2 and washed with H_2O (50 mL). The aqueous layer was extracted two additional times with CH_2Cl_2. The combined organic layers were dried with Na_2SO_4, filtered, and concentrated. The obtained white solid (260 mg, 45% yield) was sufficiently pure for subsequent steps. ^{1}HNMR($CDCl_3$, ppm): 7.51 (2H, s), 7.24 (2H, s), 7.21 (2H, s), 7.10 (2H, s), 6.85 (2H, s), 6.78 (1H, s), 5.05 (4H, s) ^{13}CNMR(ppm): 139.32, 130.34, 129.97, 124.21, 119.14, 49.76; ESI-MS$^+$: 317.0 m/z

Diethyl 1,3-bis(*N*-methylimidazolyl)-5-phenyl-phosphonate

Added 7.4 mg $Pd(OAc)_2$ (0.033 mmol), 40 mg dppf (0.066 mmol), 13 mg KOAc

(0.132 mmol) to a two neck flask. The headspace was purged with N_2 for 10 minutes. After purging, the solids were dissolved in 8 mL THF, NEt_3 (0.29 mL, 2.08 mmol) was added, and the solution heated to 65 ^{o}C under N_2 for 10 minutes. Diethyl phosphite (0.21 mL, 1.64 mmol) and 5-bromo-1,3-bis(*N*-methylimidazolyl)benzene (260 mg, 0.82 mmol) were added to the red orange solution. The reaction was refluxed overnight. The reaction was cooled to room temperature and concentrated. The crude product was dissolved with 50 mL CH_2Cl_2 and washed with sat. $NaHCO_3$ (~30 mL). After the layers were separated, the aqueous layer was washed with CH_2Cl_2 (2x 50 mL). The combined organic layers were washed with brine, dried with Na_2SO_4, filtered, and concentrated *in vacuo*. The resulting brown oil was purified by column chromatography on silica using 5-10% methanol in dichloromethane. Purification resulted in a brown oil (143 mg, 47% yield). ^{1}HNMR($CDCl_3$, ppm): 7.42 (4H, m), 7.12 (1H, s), 6.88 (4H, m), 5.10 (4H, s), 3.18 (4H, m), 1.16 (6H, m); ^{31}PNMR(ppm): 16.61; ESI-MS$^+$: 375.2 m/z

General procedure for [(Ru(bpa)(CH_3CN)(DMSO))$_2$(R-bmim)]

Dissolved 100 mg Ru(bpa)$(DMSO)_2$ (0.20 mmol) and 24 mg 1,3-bis(methylimidazolyl)benzene (0.10 mmol) in 10 mL CH_3CN. The solution was degassed for 10 minutes and heated to reflux under N_2 overnight. The reaction was cooled to room temperature. A brown precipitate that formed was isolated by filtration, and washed with acetonitrile and diethyl ether. The dried brown solid was the desired complex (104 mg, 89% yield), however HNMR revealed minor impurities while ESI-MS$^+$ suggested the only product was the desired complex with various solvent molecules bound. ^{1}HNMR($CDCl_3$, ppm): 8.73 (2H, t), 8.57 (2H, s), 7.94 (2H, d), 7.88 (3H, m), 7.84 (2H, s), 7.74 (2H, t), 7.64 (3H, m), 7.54 (2H, d), 3.09 (2H, s), 2.46 (7H, s), 2.02 (1H, s)

[(Ru(bpa)(CH_3CN)(DMSO))$_2$(phos-bmim)]

Yielded a brown powder (98 mg, 89% yield). ESI-MS$^+$: $[(Ru)_2(\text{phos-bmim})+Na]^{2+}$ = 661.2 m/z; $[(Ru)_2(\text{phos-bmim})–(CH_3CN)_2]^{2+}$ = 611.2 m/z; $[(Ru)_2(\text{phos-bmim})–(DMSO)_2+H_2O]^{2+}$ = 582.2 m/z

General procedure for [Ru(bpa)(R'-isq)$_2$] and [(Ru(bpa)(R'-isq))$_2$(R-bmim)]

Dissolved 49 mg [(Ru(bpa)(CH_3CN)(DMSO))$_2$(bmim)] (0.043 mmol) and 10.5 uL isoquinoline (isq, 0.086 mmol) in 10 mL CH_3OH. The solution was degassed for 10 minutes and heated to reflux under N_2 for 2 hours. The reaction was concentrated *in vacuo*, and purified by column chromatography on silica gel using a gradient elution from 3-50% CH_3OH in CH_2Cl_2. The first brown band eluted was [Ru(bpa)$(isq)_2$] as a brown solid (19 mg, 78% yield). The third red band eluted was [(Ru(bpa)(isq)$)_2$(bmim)] (5 mg, 10% yield).

[Ru(bpa)$(isq)_2$] (Ru)

^{1}HNMR(d_6-DMSO, ppm): 8.75 (1H, dd), 8.57 (1H, s), 7.98 (1H, s), 7.86 (3H, m), 7.75 (1H, dt), 7.65 (2H, m), 7.50 (1H,d); ESI-MS$^+$: 602.2 m/z

[(Ru(bpa)(isq)$)_2$(bmim)] (Ru_2)

^{1}HNMR(CD_3OD, ppm): 8.53 (5H, m), 8.04 (m, 4H), 7.81 (6H, m), 7.70 (2H, t), 7.58 (4H, m), 7.52 (2H, m), 7.29 (2H, s), 7.24 (1H, t), 7.01 (2H, d), 6.89 (2H, s), 6.73 (1H, s), 6.18 (2H, s), 3.33 (theoretically 4H covered by CD_3OD, s); ESI-MS$^+$: 1182.1 m/z

[Ru(bpa)(phos-isq$)_2$] (Ru-P_2)

Results in a brown powder (8 mg, 17% yield). ^{1}HNMR(CD_3OD, ppm): 8.79 (2H, s), 8.70 (2H, m), 8.32 (2H, d), 8.01 (5H, m), 7.85 (4H, m), 7.73 (3H, m), 7.52 (1H, s), 4.11 (8H, m), 1.28 (16H, m); ^{31}PNMR(ppm): 16.15; ESI-MS$^+$: 874.3 m/z

[(Ru(bpa)(phos-isq)$)_2$(bmim)] (Ru_2-P_2)

Results in a brown powder (10 mg, 23% yield). ^{1}HNMR($CDCl_3$, ppm): ^{31}PNMR(ppm): 16.33, 15.90; ESI-MS$^+$: [Ru_2-P_2 + Na]$^+$ 1481.6 m/z

[(Ru(bpa)(isq)$)_2$(phos-bmim)] (Ru_2-P)

Results in a brown powder (18 mg, 26% yield). ^{1}HNMR($CDCl_3$, ppm): 8.49 (4H, m), 7.90 (3H, s), 7.76 (5H, m), 7.56 (3H, s), 7.44 (4H, m), 6.89 (2H, s), 6.18 (1H, s), 5.11 (2H, s), 4.02 (4H, s), 1.24 (6H, s); ^{31}PNMR(ppm): 16.95; ESI-MS$^+$: [Ru_2-P – isq]$^+$ = 1235.8 m/z

Modification of WO_3

Electrodes of WO_3 were prepared exactly according to the procedure reported previously in Chapter 3. As prepared electrodes were soaked for 72 hours in 15-10 uM [Ru] dissolved in CH_3CN with dropwise addition of MeOH to ensure complete dissolution. The films were soaked in the dark under ambient conditions.

Photoelectrochemical Measurements Photoelectrochemical experiments were carried out on either a CHI 660 or CHI 1000. Under non-aqueous conditions, 100 mM recrystallized $TBAPF_6$ was used as the supporting electrolyte in dry CH_3CN in a wetbox under constant N_2 atmosphere. Glassy carbon or modified WO_3 was used as the working electrode, platinum wire or disk was used as the counter electrode, and SCE was used as the reference electrode.

Aqueous electrochemistry was carried out using 18.2 ohm Millipore water with various supporting electrolytes. The electrode of interest was always the working electrode, platinum wire was the counter electrode, and SCE was the reference electrode. Photoelectrochemistry was performed by illuminating electrodes with a 150 W Xe lamp equipped with an AM 1.5G filter and adjusted to 100 mW cm^{-2} through a fiber optic bundle.

Faradaic efficiency measurements were carried out using a FOSPOR fluorescence O_2 sensor from NeoFox in a N_2 purged custom two sided cell separated by a medium frit. The O_2 sensor was calibrated using two-point calibration at 20.9% O_2 in air and 0.0% O_2 under flowing N_2 for 30 minutes. The reactions were illuminated at 100 mW cm^{-2} with an AM 1.5G filter after sealing the cell and collecting baseline O_2 for at least 15 minutes. The potential was always poised at 1.23 V vs. RHE.

Homogeneous water oxidation using $Ce(NH_4)_2(NO_3)_6$ Homogeneous water oxidation was carried out in the dark using $Ce(NH_4)_2(NO_3)_6$ as the sacrificial oxidant. The FOSPOR O_2 probe was calibrated at 20.9% O_2 in air and 0.0% O_2 under flowing N_2 for 30 minutes. The appropriate amount of catalyst (from an acetonitrile stock solution) was added to 10 mL H_2O to afford a final catalyst concentration of 1.0 uM in H_2O. The solution was purged with N_2 for 20 minutes and then the cell was sealed under N_2. After collecting baseline for at least 15 minutes, 0.40 mL of degassed 1 M $Ce(NH_4)_2(NO_3)_6$ in water was added to the reaction through a Schlenk port. To counterbalance the head space pressure, 0.40 mL of head space was removed from the vessel. The reaction was sealed, and O_2 production was measured. After all of the cerium was consumed (as evidenced by solution turning clear from yellow), additional $Ce(NH_4)_2(NO_3)_6$ was added similar to the first spike. Cerium was added until no more O_2 evolution was observed for at least 30 minutes.

References

1 Recent reviews of DSSCs: a) Ooyama, Y.; Harima, Y. *Eur. J. Org. Chem.* **2009**, 2903; b) Mishra, A.; Rischer, M. K. R.; Bäuerle, P. *Angew. Chem. Int. Ed.* **2009**, *48*, 2474; c) Grätzel, M.; Durrant, J. R. "Dye and perovskite sensitized mesoscopic solar cells," *Clean Electrity and Photovoltaics*: 2nd, pp. 413-452.

2 Representative examples: a) Fillinger, A.; Parkinson, B. A. *J. Electrochem. Soc.* **1999**, *146*, 4559; b) Kilsa, K.; Mayo, E. I.; Brunschwig, B. S.; Gray, H. B.; Lewis, N. S.; Winkler, J. R. *J. Phys. Chem. B* **2004**, *108*, 15640.

3 Young, K. J.; Martini, L. A.; Milot, R. L.; Snoeberger III, R. C.; Batista, V. S.; Schmuttenmaer, C. A.; Crabtree, R. H.; Brudvig, G. W. *Coord. Chem. Rev.* **2012**, *256*, 2503.

4 McNamara, W. R.; Milot, R. L.; Song, H-e, Snoeberger III, R. C.; Batista, V. S.; Schmuttenmaer, C. A.; Brudvig, G. W.; Crabtree, R. H. *Energy Environ. Sci.* **2010**, *3*, 917.

5 Negre, C. F. A.; Milot, R. L.; Martini, L. A.; Ding, W.; Crabtree, R. H.; Schmuttenmaer, C. A.; Batista, V. S. *J. Phys. Chem. C* **2013**, *117*, 24462.

6 Duan, L.; Bozoglian, F.; Mandal, S.; Stewart, B.; Privalov, T.; Llobet, A.; Sun, L. *Nat. Chem.* **2012**, *4*, 418.

7 Jiang, Y.; Li, F.; Zhang, B.; Li, X.; Wang, X.; Huang, F. Sun, L. *Angew. Chem. Int. Ed.* **2013**, *52*, 3398.

8 Sullivan, B. P.; Calvert, J. M.; Meyer, T. J. *Inorg. Chem.* **1980**, *19*, 1404.

9 Takeuchi, K. J.; Thompson, M. S.; Pipes, D. W.; Meyer, T. J. *Inorg. Chem.* **1984**, *23*, 1845.

10 Brewster, T. P.; Konezny, S. J.; Sheehan, S. W.; Martini, L. A.; Schmuttenmaer, C. A.; Batista, V. S.; Crabtree, R. H. *Inorg. Chem.* **2013**, *52*, 6752.

11 Park, H.; Bae, E.; Lee, J-J.; Park, J.; Choi, W. *J. Phys. Chem. B* **2006**, *110* 8740.

12 a) Yan, S. G.; Hupp, J. T. *J. Phys. Chem* **1996**, *100*, 6867; b) Chen, Z.; Concepcion, J. J.; Jurss, J. W.; Meyer, T. J. *J. Am. Chem. Soc.* **2009**, *131*, 15590.

13 a) Kalyanasundaram, K. *Coord. Chem. Rev.* **1982**, *46*, 159; b) Montalti, M.; Cedi, A.; Prodi, L.; Gandolfini, M. T. In *Handbook of Photochemistry*, 3rd ed.; CRC Press Taylor & Francis Group: Boca Raton, FL, 2006; 379–404.

14 Gao, Y.; Ding, X.; Liu, J.; Wang, L.; Lu, Z.; Li, Sun, L. *J. Am. Chem. Soc.* **2013**, *135*, 4219.

15 Patil, P. S.; Patil, P. R. *Bull. Mater. Sci.* **1996**, *19*, 651.

16 Yourey, J. E.; Bartlett, B. M. *J. Mater. Chem.* **2011**, 21, 7651.

17 Zhong, D. K.; Zhao, S.; Polyansky, D. E.; Fujita, E. *J. Catal.* **2013**, *307*, 140.

18 Pyper, K. J.; Yourey, J. E.; Bartlett, B. M. *J. Phys. Chem. C.* **2013**, *117*, 24726.

19 Klahr, B.; Gimenez, S.; Fabregat-Santiago, F.; Hamann, T. W.; Bisquert, J. *J. Am. Chem. Soc.* **2012**, *134*, 4294.

20 Evans, I. P.; Spencer, A; Wilkinson, G. *J. Chem. Soc., Dalton Trans.* **1973**, 204.

21 Alyapyshev, M. Y.; Babain, V. A.; Borisova, N. E.; Kiseleva, R. N.; Safronov, D. V.; Reshetova, M. D. *Mendeleev Commun.* **2008**, *18*, 336.

22 Alcalde, E.; Mesquida, N.; Pérez-García, L. *Eur. J. Org. Chem.* **2006**, 3988.

Chapter 3

Anchoring Molecular Iron Catalysts to WO_3

Portions of this chapter have been published:

Klepser, B. M.; Bartlett, B. M. *J. Am. Chem. Soc.* **2014**, *136*, 1694-1697.

3.1 Introduction

At the start of this work, there were no known instances of activating molecular WOCs using semiconductors as the light absorber. Over the last two years, there have been multiple reports along these lines.[1,2,3,4] Although the first attempt to activate the fastest molecular ruthenium WOCs in Chapter 2 was not completely successful, there are numerous other catalysts to try. During this time, a molecular ruthenium catalyst tethered to Fe_2O_3 was communicated.[1] However, in this report, no evidence for oxygen evolution is presented. Furthermore, this report did not demonstrate prolonged stability of the anchors under illumination or under an applied bias in aqueous solutions. Carboxylate anchors are used to attach the Ru complex to the Fe_2O_3 surface, and carboxylate anchors typically suffer from weak surface attachment in aqueous solutions.[5]

This report was followed by the report from Zhong and co-workers that demonstrated the photostability of a different Ru WOC on WO_3 using phosphonate anchors. However, the reported improvements in photocurrent are minimal. For instance, the onset of photocurrent is less than 50 mV earlier and the saturated photocurrent is less when the WO_3 surface is modified.[2] These results matched similarly to those observed in Chapter 2.

Although our work has already focused on phosphonate anchors and WO_3, our goal is to differentiate this work by improving earth-abundant first-row transition metal complexes and quantifying the improvement in photocatalysis. As mentioned in the introduction, many years ago Elizarova et al. reported water oxidation using first-row transition metal catalysts.[6] It was ultimately discovered that many of their best catalysts decomposed into simply bipyridine salts or heterogeneous catalysts.[7] Until recently, good first-row transition metal WOCs were non-existent. In 2010, Ellis and co-workers reported a Fe tetra-amido macrocyclic ligand (TAML) complex which oxidized water at a very high rate for a very short duration. Shortly thereafter, Fillol et al. reported a large family of iron catalysts that exhibited excellent stability in the presence of sacrificial oxidants and moderate reaction rates.[8] The best catalyst (**Fe-1**) from that report, depicted in Scheme 3.1, served as the inspiration for differentiating our research from the previous to reports and led to the first photocatalytic system wherein the improvement in photocatalysis and selectivity could be quantified. The family of catalysts including **Fe-1** have been shown to act as molecular catalysts in solution, and the catalytic mechanism has been thoroughly characterized previously.[10]

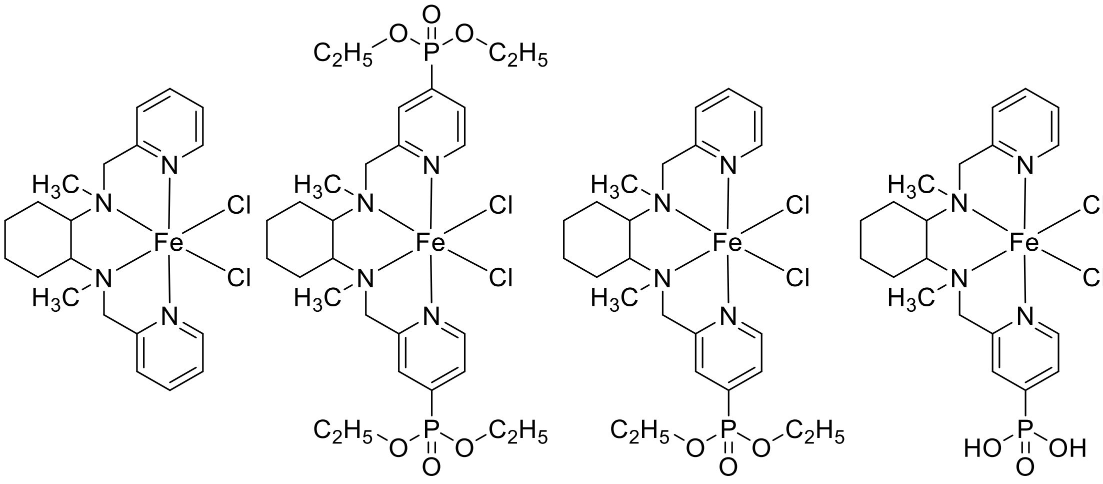

Fe-1 **Fe-2** **Fe-3** **Fe-4**

Scheme 3.1. Targeted phosphonate modified molecular Fe WOCs

3.2 Synthesis and Characterization of Modified Fe WOCs

There are very few examples of modifying the *para-* position on the pyridine rings for the *N,N'*-bis(2-methyl-pyridyl)-*N,N'*-dimethyl-cyclohexyldiamine (**1**) class of ligands.[9] At first, the most challenging aspect towards synthesizing the modified ligands is devising a protocol to efficiently incorporate anchoring groups onto the early intermediates. Scheme 3.2 represents the optimized synthesis for incorporating the protected phosphonate anchoring group onto the 2-chloromethyl-pyridine (**II**). The first step in this synthesis has demonstrated good conversion relative to alternative methods towards incorporating the *o*-methyl alcohol (**I**). In addition to the optimized reaction, SeO_2 and $KMnO_4$ are pursued as oxidants for 4-bromo-2-methylpyridine. These resulted in low yields and slow conversion of the methyl group to the corresponding aldehydes. As such, the three step reaction is preferred in this case.

Palladium cross-coupling is used to convert the 4-bromo substituent to the corresponding diethyl phosphonate. The reaction conditions are adapted from a previously reported synthesis.[10] Through numerous iterations, it has become apparent that this reaction is not sensitive to oxygen, although the reaction rates are slightly higher when performed under air free conditions. Additionally, the reaction is not sensitive to water since dry and wet THF reacted similarly. Although it is reported that this reaction should be carried out in excess of the aryl bromide to improve the ability to separate the products (the diethyl phosphite streaks during column chromatography and limits separation), these reactions still worked exceptionally well at equimolar concentrations of diethyl phosphite and aryl bromide.

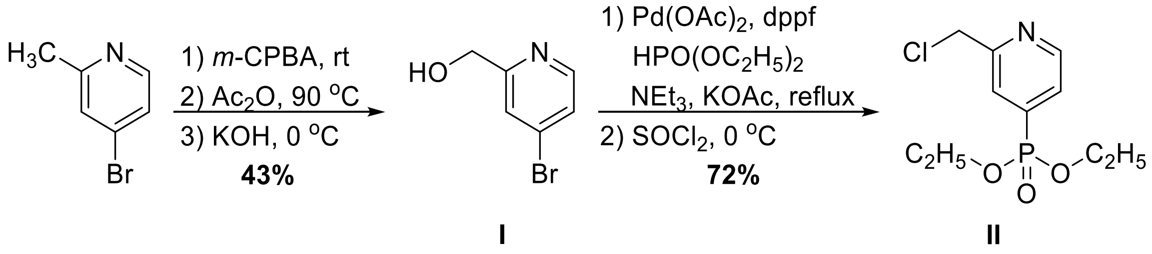

Scheme 3.2. Synthetic route to phosphonate precursor

From alcohol **I**, the *o*-aldehyde is initially targeted to better coincide with common literature methods for synthesizing ligand **1**. However using Dess-Martin periodinane, SeO_2, or $KMnO_4$ results in slow conversion of the *o*-alcohol results in <30% product formation. Alternatively, thionyl chloride reacts quantitatively with the *p*-bromopyridine or the *p*-pyridylphosphonate to afford the corresponding intermediate **II**. As such, the preparation of **II** is the higher yielding route to incorporating phosphonate into the desired ligand scaffold.

The remaining obstacle associated with preparing ligand **2** is the poor literature precedent for alkylation of the *N*,*N*'-dimethyl-*trans*-1,2-cyclohexyldiamine. Previously, these reactions are reported to take many days,[11] are multiphasic,[12] or require strict control of the reaction pH.[13] Theoretically, the alkylation is a simple S_N2 reaction which should only require base and heat since the alkyl substituent is a bad leaving group. Under optimized conditions, *N*,*N*'-dimethyl-*trans*-1,2-cyclohexyldiamine is alkylated with **II** in acetonitrile with excess triethylamine at reflux. No starting material is observed after refluxing 3 hours.

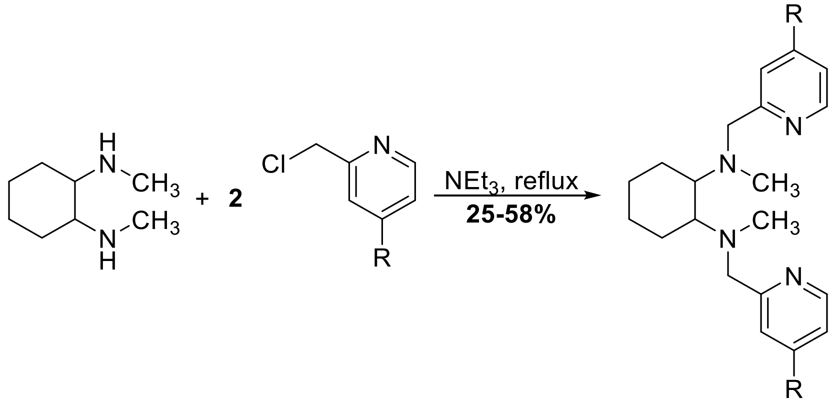

R = -H
-PO(OC$_2$H$_5$)$_2$

R = -H **1**
-PO(OC$_2$H$_5$)$_2$ **2**

Scheme 3.3. Synthesis of symmetric ligands

Using commercially available substrates, the symmetric ligands **1** and **2** could be prepared rapidly. The major advantage of this synthesis is the flexibility of each step. For instance, the aryl bromide could be converted into other anchoring groups (such as imidazolidine or catecholate) by changing the palladium cross-coupling reaction conditions. Another flexible aspect of this synthesis is the ability to perform palladium cross-coupling reactions on the complete ligand. When the dibrominated ligand is subjected to palladium cross-coupling with diethyl phosphite, the reaction proceeds in moderate yield. This observation is most likely because the constructed ligand is unable to geometrically adopt the square planar coordination sphere that is commonly necessary for palladium cross-coupling reactions.[14] As such, the reaction is not inhibited by the tetra-coordinate nature of the ligand wherein other ligands might inhibit palladium's reactivity.

Although ligand **2** is initially the desired target, due to the elongated *z*-axis of the resulting complex, it is hypothesized that the surface coverage for the corresponding iron complex may be diminished because the two anchoring groups could occupy multiple surface sites. As a result, an asymmetric ligand is also prepared that only possessed a single anchoring phosphonate group. To further increase the adsorptivity of the complex, the phosphonate group is deprotected prior to adsorbing the complexes onto WO_3. Ligands **3** and **4** are most efficiently synthesized according to

Scheme 3.4 and Scheme 3.5. Intermediate **III** is formed quantitatively upon stirring *N*,*N*'-dimethyl-*trans*-1,2-cyclohexane diamine with 2-pyridylcarboxaldehyde at room temperature for 15 minutes. Previously, **IV** was prepared by ring opening of the imidazole intermediate **III** with $NaBH_4$.[15] However, when **III** is refluxed with $NaBH_4$ overnight, no product is observed by TLC analysis or mass spectrometry. As such, a stronger hydride source, $NaBH_3CN$, is required to open the imidazole ring and produce the asymmetric product. This reaction proceeds in a 73% yield.

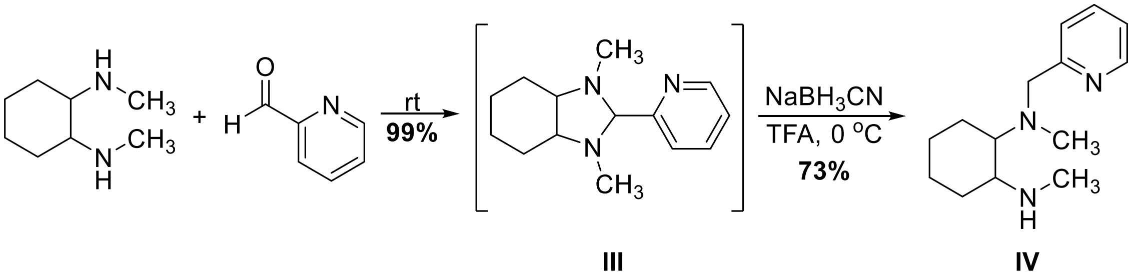

III **IV**

Scheme 3.4. Incorporating assymetry in ligand

After setting the ligand's asymmetry, ligand **3** can be prepared according to our previously developed conditions for synthesizing the diphosphonate analog. Although compound **IV** exhibits asymmetry, incorporating a second pyridyl ring results in significantly decreased symmetry. As a result, ^{13}C-NMR spectroscopy cannot be used to verify the structure of ligand **3** even at high concentrations. Furthermore, the peaks in the ^{1}H-NMR spectra are broad and poor peak splitting is observed. High-resolution mass spectrometry (HRMS) confirms the identity of ligand **3**. Furthermore, thin layer chromatography (TLC) illustrates ligand **3**'s purity. Ligand **3** can then be deprotected to prepare ligand **4**. Ligand **4** is isolated in 56% yield from reaction with 10 equivalents of bromotrimethylsilane when stirred at room temperature and quenched with methanol.

The final deprotection of diethyl phosphonate proved the most sensitive reaction in the whole synthesis. This reaction needed to be kept under extremely inert conditions, and in our hands required fresh, dry TMSBr. Furthermore, 10 equivalents of TMSBr are imperative to the success of this reaction. When the reaction is carried out in the presence of 5 eq., only partial deprotection is observed.

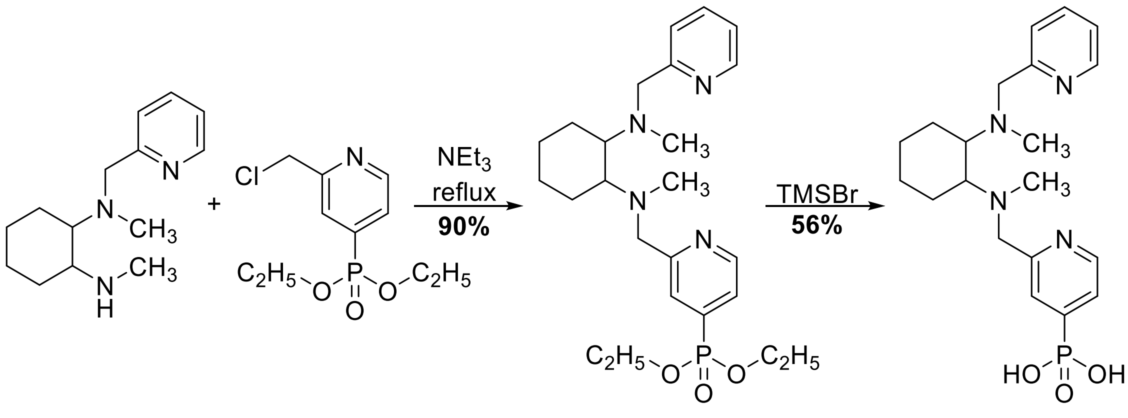

3 **4**

Scheme 3.5. Synthesis and deprotection of asymmetric ligand

Finally, metal coordination is carried out in acetonitrile under air-free conditions to ensure the iron chloride is not prematurely oxidized. The results of those reactions are summarized in Scheme 3.6. The reactions are rapid and apparent by a swift color change from orange (the color of the ligand in solution) to yellow, orange, red, or purple. In the UV-Vis spectroscopy of **Fe-1**, **Fe-2**, and **Fe-3**, the visible MLCT shifts significantly depending on the number of anchoring groups as illustrated in Figure 3.1. Additionally, the solubility of the iron complexes in various solvents increased as the number of anchoring

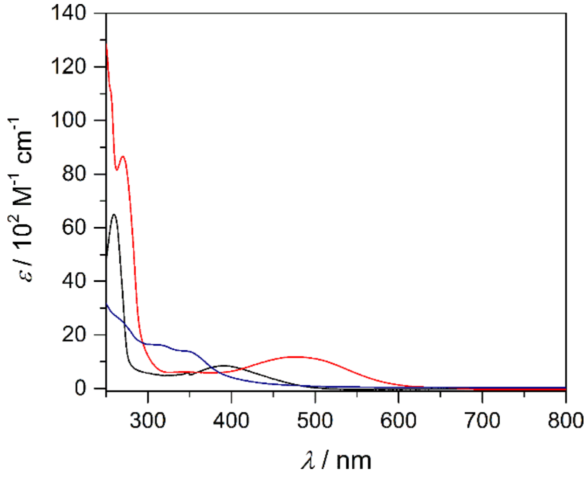

Figure 3.1 UV-Vis spectra of **Fe-1** (black), **Fe-2** (red), and **Fe-3** (blue) in CH_3CN

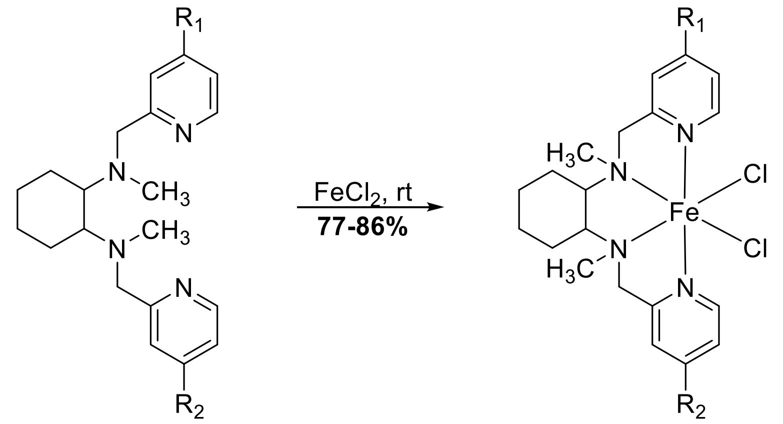

$R_1 = R_2 =$ -H	**1**	$R_1 = R_2 =$ -H	**Fe-1**
-$PO(OC_2H_5)_2$	**2**	-$PO(OC_2H_5)_2$	**Fe-2**
$R_1 =$ -H		$R_1 =$ -H	
$R_2 =$ -$PO(OC_2H_5)_2$	**3**	$R_2 =$ -$PO(OC_2H_5)_2$	**Fe-3**
-$PO(OH)_2$	**4**	-$PO(OH)_2$	**Fe-4**

Scheme 3.6. Metallation of ligands with $FeCl_2$

groups increased. For instance, **Fe-1** is barely soluble in acetonitrile and insoluble in water, whereas **Fe-2** is readily soluble in all solvents but diethyl ether. Due to the paramagnetic nature of these complexes, and the relative asymmetry of **Fe-3** and **Fe-4**, ^{1}H-NMR spectroscopy can only confirm the purity and identity of **Fe-1** and **Fe-2**. However, ESI-MS$^+$ analysis indicates that only the desired complex is present in the corresponding complexes, and there is no free ligand. Elemental analysis ensures no impurity of iron chloride and confirms the purity of the desired complexes **Fe-1** and **Fe-2**. The single crystal X-ray structure of **Fe-2**, depicted in Figure 3.2, suggests the desired configuration is obtained for all of the obtained iron complexes.

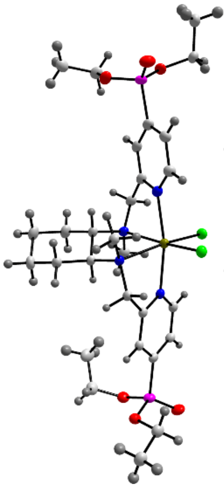

Select Bond Metrics

Fe–N_{py}, *avg*	2.178 Å
Fe–N_{am}, *avg*	2.286 Å
Fe–Cl, *avg*	2.421 Å
C–P, *avg*	1.822 Å
N_{py}–Fe–N_{py}	167.3°
N_{am}–Fe–N_{am}, *avg*	77.9°
N_{py}–Fe–N_{am}, *avg*	85.2°
Cl–Fe–Cl	100.4°

Figure 3.2. X-ray crystal structure of 1 where C = white, H = gray, N = blue, O = red, P = magenta, Cl = green, Fe = yellow

Cyclic voltammetry (CV) in non-aqueous solutions is used to confirm the electrochemical redox potential of complexes **Fe-1** and **Fe-2** as presented in Figure 3.3. The open circuit potential and initial peak suggest that the complexes are indeed Fe^{2+} in solution. In the absence of water and oxygen, the $Fe^{2+/3+}$ couple is the primarily evident redox event. It has been suggested previously the $Fe^{3+/4+}$ redox couple is kinetically slow and are not typically be observed under non-aqueous conditions.[16] However, there is a small peak present for the complexes that suggested these complexes are undergoing a $Fe^{3+/4+}$ redox event. This observation is imperative to understanding the activation potential

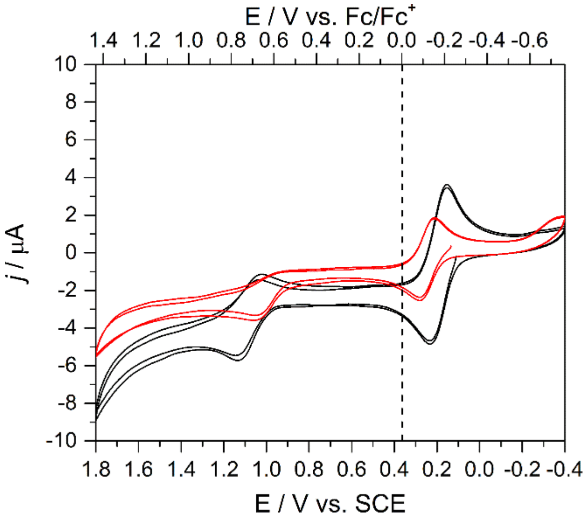

Figure 3.3 Cyclic voltammetry of **Fe-1** and **Fe-2** in 100 mM $TBAPF_6$ with CH_3CN at 20 mV s^{-1} using GC WE, Pt CE, and SCE RE

for catalysts because the resting catalytic species is likely in the Fe^{4+} oxidation state.[8] The non-aqueous electrochemistry is much less important for comparing all complexes than the

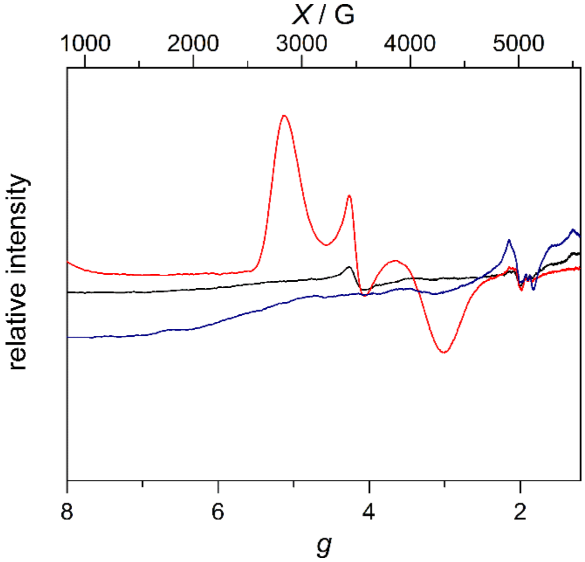

Figure 3.4 Spectroelectrochemical EPR spectrum of 2.5 mM **Fe-2** in 100 mM $TBAPF_6$ with CH_3CN at 4 K after electrolysis at open circuit potential (black), 0.60 V vs. SCE (red), and 1.40 V vs. SCE (blue)

aqueous CVs for **Fe** in solution.

To probe the oxidation states further, spectroelectrochemical electron paramagnetic resonance spectroscopy (EPR) is carried out with **Fe-2**. Electrolysis at various potentials followed by EPR spectroscopy reveals that iron begins as Fe^{2+} in the prepared complex. Within five minutes, Fe^{2+} is oxidized to Fe^{3+}, evidenced by the signal appearing in Figure 3.4. Electrolyzing at potentials beyond the small peak in the CV result in slow electron transfer to the solution. This result is consistent with previous examples of electrochemically synthesizing Fe^{4+} complexes. The EPR spectrum after 30 minutes of electrolysis reveals that the complex has been further oxidized to Fe^{4+} through the loss of signal. Although the $Fe^{2+/3+}$ couple is reversible for both complexes, Fe^{3+} could not be observed after electrolysis. This result suggests that trace water is present in solution, which gives rise to an $Fe^{4+}{=}O$ species in solution that can only be reduced electrochemically back to Fe^{2+}. When the complex is reduced from $Fe^{4+/2+}$, the reaction is relatively rapid, but requires twice the charge previously measured for the previous reactions. The charge doubling indicates the transfer of 2 e^-‘s back into solution supporting the $Fe^{4+/2+}$ transformation. However, no EPR spectrum is recorded since no change in the spectra is expected.

In order to ensure reactivity of the modified catalysts in aqueous solution, CV curves of the complexes are measured in pH 3 HCl or Na_2SO_4. The catalysts exhibited low electrocatalytic currents in the dark, but the electrochemical onset potentials for water oxidation are determined relative to the normal hydrogen electrode (NHE) and are summarized in Table 3.1. In pH 3 Na_2SO_4, **Fe-1** and **Fe-2** exhibit two peaks in the reductive wave for the $Fe^{2+/3+}$ as represented in Figure 3.5. The second peak is much less prominent (slight shoulder) in pH 3 HCl. It is therefore concluded that the second wave corresponds to the competitive –Cl/–H_2O ligand exchange. Wherein the solution with less Cl^- exhibits higher current densities for the –H_2O bound $Fe^{3+/2+}$ species (the pH 3 Na_2SO_4).

Complex	**$Fe^{2+/3+}$**	**$Fe^{3+/4+}$**	**E_{on} / V RHE**
Fe-1	0.73 V	-	1.38 V
Fe-2	0.80 V	1.55 V	1.41 V
Fe-3	0.72 V	1.47 V	1.38 V

Table 3.1 Electrochemical oxidation potentials for **Fe** complexes in 100 mM Na_2SO_4, pH 3, GC WE, Pt CE, SCE RE at 20 mV/s.

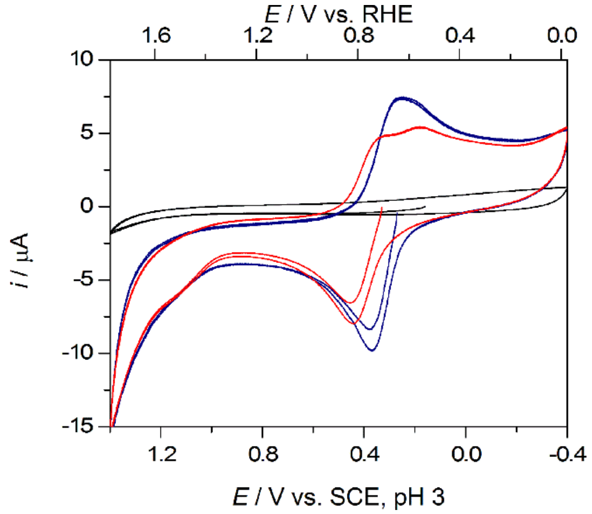

Figure 3.5 Representative aqueous CV trace of **Fe-2** in pH 3 Na_2SO_4 (red) or HCl (blue) at 20 mV s^{-1} with GC WE, Pt CE, SCE RE. (CV curves of the other complexes appear in Figure Figure B.1)

Finally, to ensure homogeneous reactivity is retained for the modified complexes, the complexes are reacted in the presence of 1000 eq. $Ce(NH_4)_2(NO_3)_6$ (CAN). The results are summarized in Table 3.2. From these results, it is apparent that the single phosphonate complexes exhibit diminished stability but only exhibit slightly decreased rate of catalysis. The most promising aspect of anchoring the catalyst to an oxidative surface such as a semiconductor is that the oxidative unit will be consumed immediately instead of being in excess. Furthermore, similar complexes have exhibited stability under highly acidic or highly oxidative conditions, but rapidly decompose in the presence of both conditions.[17] Therefore the modified complexes should all be suitable for anchoring onto semiconductor light absorbers.

Catalyst	**3 h TON (mol O_2 mol^{-1} Fe)**	**TOF (mol O_2 mol^{-1} Fe s^{-1})**
Fe-1	146	0.089
Fe-2	115	0.051
Fe-3	28	0.015
Fe-4	13	0.006

Table 3.2 Water oxidation of **Fe** catalysts in the presence of 1000 eq. CAN

3.3 Characterization of Fe WOCs on WO_3 before Photoelectrochemistry

With working WOCs in hand, it is necessary to develop conditions suitable for anchoring diethyl phosphonates onto WO_3. **Fe-2** is utilized as the test case for determining conditions to obtain maximum surface coverage. The adsorption of molecular species onto electrode surfaces follows the adsorption model described by Langmuir in 1916. Under this model, it is assumed that each surface site is equivalent and there is an equilibrium between the adsorbed and solution species. As such, over time, the molecule will equilibrate towards a maximum surface coverage. For dye sensitized solar cells, long exposure or heating have been employed to reach the maximum adsorption equilibrium. In the case of **Fe-2**, maximum surface coverage can be achieved in 24 hours at room temperature or 8 hours at 60 °C.

Although there is no method to prove the catalyst is covalently bound to the WO_3 surface definitively, CV traces of the WO_3 electrodes before soaking suggests that the molecular is likely anchored to the surface, evidenced by the $Fe^{2+/3+}$ redox event observed at ~-0.2 V vs. $F_c^{0/+}$ as shown in Figure 3.6. When the electrodes modified with **Fe-2** are removed from solution, no redox events associated with **Fe-2** are observed. These results provide good evidence that **Fe-2** is strongly bound to the surface and is not physisorbed. **Fe-3** and **Fe-4** exhibit similar CV characteristics. However, **Fe-1** does not exhibit binding to the WO_3 surface as will be discussed in the following section. This result confirms that the anchoring groups must be present in order to adsorb the catalysts to the electrode surface.

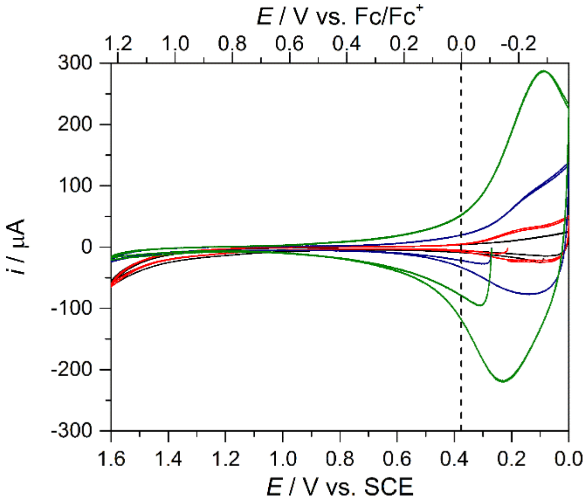

Figure 3.6 CV of **Fe-2** (red), **Fe-3** (blue), and **Fe-4** (green) on WO_3 (bare - black) in 100 mM $TBAPF_6$ with CH_3CN at 20 mV s^{-1} with Pt CE, SCE RE

The advantage of these catalysts is the easily identifiable $Fe^{2+/3+}$ redox event and its highly reversible nature. Because the event is well defined for these complexes, bulk electrolysis can be used to closely approximate the surface coverage of the catalysts on the surface. By comparing the charge passed for the same modified and bare WO_3 electrode, Faraday's equation can be employed to calculate the number of e^-'s required to completely oxidize or reduce the electrochemically active species on the surface. Since $Fe^{2+/3+}$ is a one e^- event, the surface coverage can be calculated according to the equation:

$$n = -\frac{\Delta Q}{F \times z} \qquad (1)$$

Where n is the moles of catalyst on the surface, ΔQ is the change in number of electrons passed, F is Faraday's constant, and z is the number of electrons per reaction. The surface coverages are summarized below in Table 3.3. Representative examples of the bulk electrolyses are found in Figure Figure B.2. It should also be noted that **Fe-2** exhibits limited binding to bare FTO (>2 nmole), which is the conductive substrate upon which the WO_3 nanoparticles are deposited on (see Figure Figure B.3).

Catalyst	Surface Coverage (nmoles cm^{-2})
Fe-1	0
Fe-2	15±5
Fe-3	27±3
Fe-4	93±20

Table 3.3 Surface coverage of **Fe** on WO_3 in 100 mM $TBAPF_6$ in CH_3CN

Although electrochemistry is useful for determining the amount of catalyst on the surface, it is insufficient to identify the electrochemically active species on the WO_3 surface conclusively as **Fe-2**, **Fe-3**, or **Fe-4**. To prove the presence of the desired ligand bound to the electrode surface, Raman spectroscopy is used. Because Raman is a light scattering technique, it is commonly used to determine surface adsorption and identify impurities on the bulk of a material. Since the catalyst is only bound on the surface of the WO_3, low intensities are expected for the catalyst bound to the surface. Raman spectroscopy of the catalyst powders matches the corresponding peaks of the modified WO_3 as depicted in Figure 3.7. The intensity of the peaks for **Fe-3** and **Fe-4** are significantly reduced from **Fe-2** on WO_3 this result further indicates the significant drop in symmetry associated with one vs. two phosphonate anchoring groups.

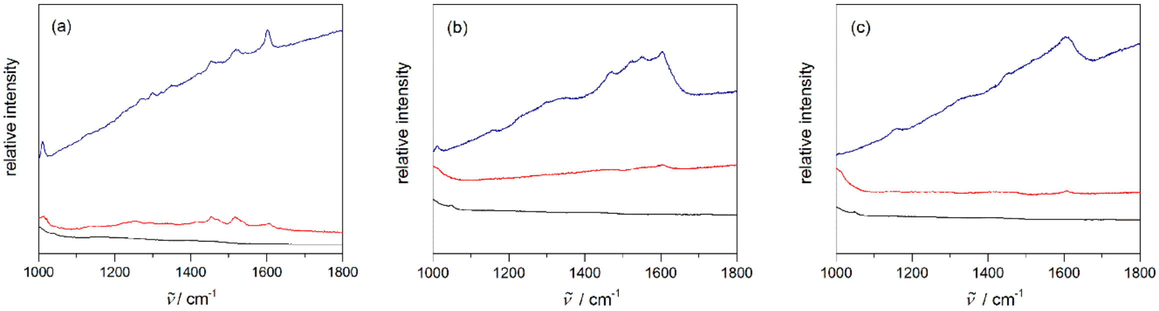

Figure 3.7 Raman spectroscopy of **Fe-2** (a), **Fe-3** (b), **Fe-4** (c) on WO_3 (red) compared to unmodified WO_3 (black) and the corresponding **Fe** powder (blue)

Along with electrochemical and Raman spectroscopic evidence for surface attachment, a spectroscopic surface technique is also necessary to ensure the iron is present on the surface. It will also serve as an important marker that the complex does not decompose into catalytic Fe_2O_3 or FeOOH nanoparticles under illumination. When X-ray photoelectron spectroscopy (XPS) is employed on the modified WO_3 films, the Fe 2p peaks are present prior to photoelectrochemical reactions as illustrated in Figure 3.8. This data further supports the notion that the modified catalysts are successfully anchored onto the WO_3 surface.

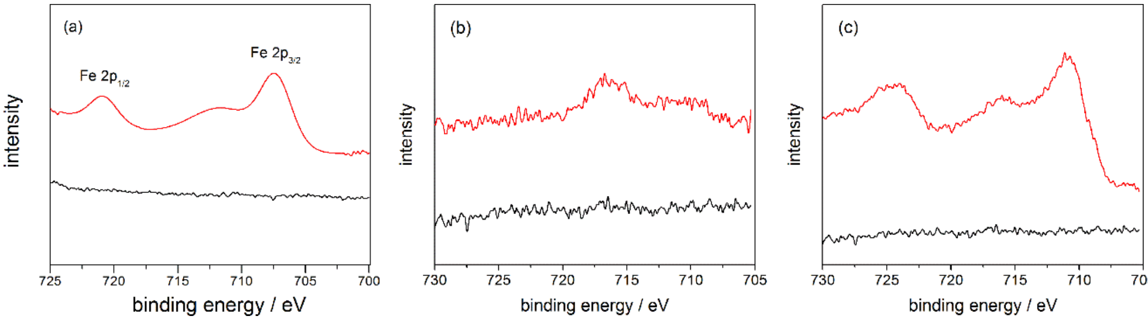

Figure 3.8 X-ray photoelectron spectra of **Fe-2** (a), **Fe-3** (b), and **Fe-4** (a) on WO_3 (red) compared to unmodified WO_3 (black) prior to performing photoelectrochemistry

3.4 Photoelectrochemistry of Fe WOCs on WO_3

With the catalysts successfully anchored to WO_3, the photoelectrochemistry of the catalysts on WO_3 is compared to the unmodified or component modified WO_3. As stated previously, the overarching hypothesis of this thesis is that the molecular catalyst will be the primary active site upon electron transfer from the catalyst to the semiconductor. Two outcomes are anticipated. First, the rate of water oxidation should increase since the molecular catalysts are typically faster than the semiconductor surface (10^{-2} vs. 10^{-6} TOs^{-}

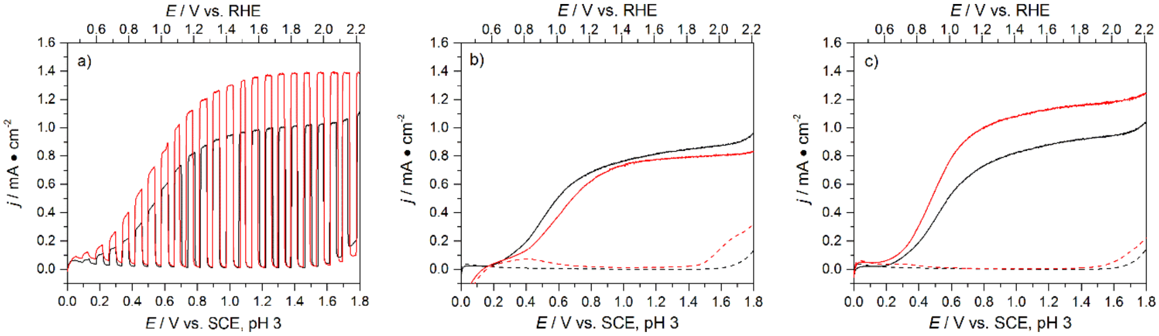

Figure 3.9 Representative linear sweep voltammetry of **Fe-2** (a), **Fe-3** (b), and **Fe-4** (c) on WO_3 (red) under 1 sun illumination in the light (solid) or dark (dashed) compared to the same electrode prior to adsorption (black) 100 mM Na_2SO_4 pH 3 using Pt CE and SCE RE

^{1} for **Fe-1** and WO_3 respectively).[8,18] Second, the Faradaic efficiency (F.E.(O_2), O_2 product generated per four reacted electrons per the stoichiometry of the reaction), which is comparable to selectivity towards the desired reaction, of the combined system should be improved. For other semiconductors, the F.E.(O_2) is unity.[19] However, WO_3 presents a unique case wherein WO_3 kinetically oxidizes the anions of common salts used in electrochemistry at a rate comparable to that of water oxidation. As a result, WO_3 typically exhibits F.E.(O_2)s significantly lower than unity. Therefore, anchoring a molecular catalyst to the surface should impart greater F.E.(O_2) for the system because the catalysts cannot thermodynamically oxidize the anions and the kinetically slow active sites for WO_3 should be occupied. The observation of improved F.E.(O_2) is imperative for establishing the catalytic activity of the molecular species on the electrode surface. Therefore, in the case of anchoring new catalysts, they should all initially be anchored to WO_3 to ensure they are participating in photocatalysis.

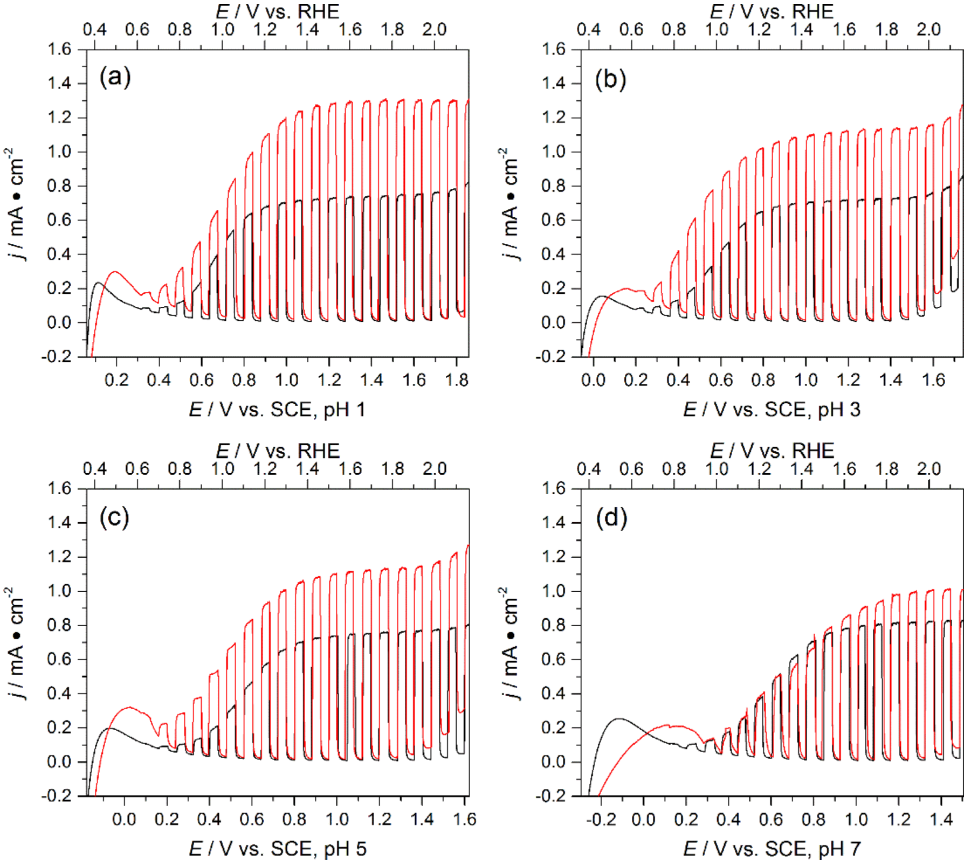

Figure 3.10 Chopped light LSV traces of **Fe-2** on WO_3 (red) compared to unmodified WO_3 (black) in 100 mM Na_2SO_4 at pH 1 (a), 3 (b), 5 (c), or 7 (d) under 1 sun illumination at 20 mV s^{-1} using Pt CE and SCE RE

With this design principle in mind, the dark, light, or chopped linear sweep voltammograms (LSVs) are collected for the **Fe** catalysts bound to WO_3 in 100 mM Na_2SO_4 at pH 3. The electrolyte and pH are selected based on the observations by Choi et al. and Gray et al. that WO_3 exhibits ~60% F.E.(O_2) under illumination in the presence of SO_4^{2-} at pH 3.[20,21] In the dark, the catalysts exhibit no early onset in electrocatalysis for **Fe-2** on WO_3. This observation is inconsistent with the onset of electrocatalysis in solution at ~1.72 V vs. NHE. The most likely explanation for the early onset in **Fe-2** is that the large number of active sites relative to **Fe-2** on the surface. Furthermore, in the dark, the $Fe^{2+/3+}$ redox couple is apparent in all cases. This result supports the notion that the catalysts are initially bound to the surface in pH 3 aqueous solution.

Under illumination, the combined photocatalysts exhibit a change in photocurrent densities for the modified electrodes as illustrated in Figure 3.9. **Fe-2** on WO_3 exhibits the greatest change (up to 60% increase) in photocurrent, indicating that this catalyst allows for the fastest rate of water oxidation on the surface and/or it has the fastest rate of electron transfer between itself and the WO_3 electrode. These possibilities can most readily be distinguished through the use of transient absorption spectroscopy. **Fe-3** on WO_3 demonstrates no change in photocurrent density under illumination. This result suggests that this catalyst is either inactive on the electrode surface or the charge transfer between WO_3 and the catalyst is slow. Finally, **Fe-4** on WO_3 exhibits up to a 35% increase in photocurrent indicating that the rate of catalysis or charge transfer is still slow than **Fe-2** on WO_3, but is faster than **Fe-3**. The results from homogeneous water oxidation suggests that the rate of catalysis could be the issue for **Fe-3** and **Fe-4** due to the large decrease in the initial turnover frequency. However, the large difference in photocurrent between **Fe-3** and **Fe-4** suggests that the likely explanation is charge transfer between the catalysts and WO_3. This observation is supported by the dye-sensitized solar cell literature, which has demonstrated a link between increasing anchors and increasing charge-transfer rates.[22] Deprotecting both anchoring groups from **Fe-2** should result in the maximum photocurrent enhancement based on the observation that **Fe-4** exhibits higher photocurrents than **Fe-3**.

To ensure that ligands **2-4** or $FeCl_2$ are not responsible for enhancing the photocurrent density on their own, WO_3 films are soaked under identical conditions with the individual components for each catalyst. In all cases, no improvement in photocurrent density results. Furthermore, when all components are removed and WO_3 is soaked in acetonitrile, no change in photocurrent density is observed. As a result, these control experiments show that the photocurrent enhancement is a result of the molecular **Fe-2**, **Fe-3**, or **Fe-4** being present on the WO_3 surface. Representative LSVs of these controls are summarized in Figure Figure B.5.

Although confident the complete catalysts are necessary for improving the WO_3 photocurrent density, it is important to ensure that the improvements are not related to the pH of the system. Adjusting the pH would also allow the stability of the anchoring group to be probed as well. As a result, when the pH is adjusted from pH 1 to pH 7 in 100 mM Na_2SO_4, the photocurrent enhancement of **Fe-2** on WO_3 decreases from 70% at pH 1 to 30% at pH 5. However, at pH 7 the photocurrent is minimally effected. This data suggests that either the catalyst is unstable/falls off the surface above pH 5 or that WO_3 is undergoing minor degradation at pH 7 (see Figure 3.10). The stability of catalysts vs. semiconductor will be compared in Chapter 4, when the complex is anchored to $CuWO_4$, which is more stable under basic conditions, and will help separate catalyst and semiconductor stability.

Another key question is whether the thickness of the WO_3 impacts the relative change in photocurrent density for **Fe-2**. The optimal thickness for the WO_3 is ~1.8-2.0 μm. However, by spin casting fewer layers of WO_3, the thickness could be dropped to ~400-600 μm. The thinner WO_3 electrodes exhibit significantly lower photocurrent densities, as expected. When the thinner films are modified with **Fe-2**, the increase in photocurrent is proportionally similar (50% vs. 60%) to the increase for optimized WO_3 from this synthesis (Figure Figure B.6). This result suggests that the increase in photocurrent may be insensitive to the synthesis, thickness, or morphology of the semiconductor, rather it is intrinsically linked to the performance of the catalyst. Chapter 4 will probe this idea further by comparing improvements in photocurrent through multiple synthetic routes to $CuWO_4$.

In order to state that the catalyst is forming an active species on the WO_3 electrode under illumination definitively, it is necessary to quantify the products produced during the course of the reaction. Relative to bare WO_3, the WO_3 exhibits a significant increase in F.E.(O_2) when modified with **Fe-2**, **Fe-3**, or **Fe-4**, as illustrated in Figure 3.11, from 58% to ~75% for all three catalysts. This result indicates that all of the catalysts are improving

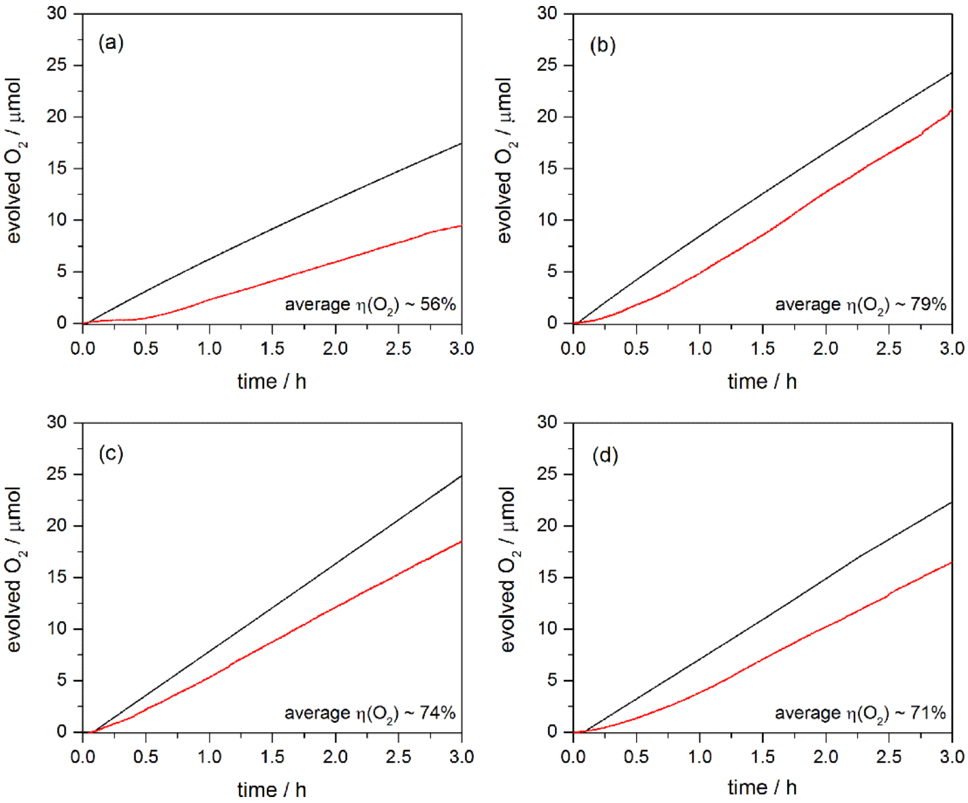

Figure 3.11 Faradaic efficiency of unmodified WO_3 (a) compared with **Fe-2** (b), **Fe-3** (c), and **Fe-4** (d) on WO_3 under 1 sun illumination at 1.23 V vs. RHE starting at t = 0; determined from theoretical yield (black) and measured yield (red) of O_2

the selectivity of the WO_3 towards water oxidation. Additionally, the similar F.E.(O_2) for all three catalysts suggests that the catalytically active mechanism for water oxidation is similar for these catalysts on the surface of WO_3. And, although minor ligand modifications has a large impact on electron transfer and relative rate of the reaction, the anchoring environment has little impact on the preference to react through the molecular catalysts as opposed to the semiconductor itself.

To address the charge balance of the entire reaction, post-illumination UV-Vis spectroscopy of the electrolyte are used to quantify the secondary products from the reaction. Because of the presence of highly oxidized sulfate anions, $FeSO_4$ could be added to an aliquot of the electrolyte, and it would be instantly oxidized by any non-O_2 products in solution. Upon addition of NaSCN, the free SCN^- rapidly coordinates to Fe^{3+} in solution. $Na_3Fe(SCN)_6$ forms a deep red complex (ε = 172 M^{-1} cm^{-1} at λ_{max} = 465 nm) whereas $Na_4Fe(SCN)_6$ forms a colorless complex. As a result, the amount of non-O_2 products can be quantified by UV-Vis spectroscopy. This experiment reveals that the remaining charge balance for the reactions are the oxidation of anions in solution to $S_2O_8^{2-}$ or HSO_5^- or to H_2O_2 and not into CO_2 formation via decomposition of the molecular species. The balanced chemical reactions can be found in the experimental section of this chapter.

The initial measurement of F.E.(O_2) for the modified electrodes is three hours under illumination, and to address the ultimate stability of the molecular species on the electrode surface. When **Fe-2** on WO_3 is illuminated for 12 hours (see Figure 3.12), the F.E.(O_2) remains higher for approximately the first 3-6 hours. After that time, there is a drop in the rate of O_2 production and the F.E.(O_2) begins to regress back to the F.E.(O_2) for bare WO_3. To ensure that this regression is due to the decomposition or detachment of the molecular species, bare WO_3 is also illuminated for 12 hours and the F.E.(O_2) is consistent over 12 hours of illumination.

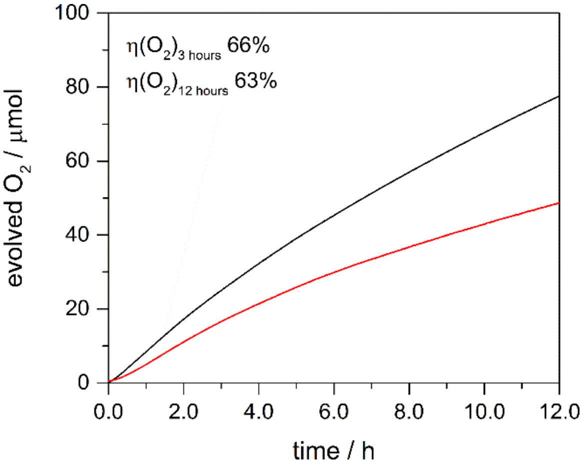

Figure 3.12 Faradaic efficiency of **Fe-2** modified WO_3 under 1 sun illumination at 1.23 V vs. RHE starting at t = 0; determined by theoretical yield (black) and actual yield (red) of O_2

Two of the major concerns with this project are 1) ensuring the catalyst does not decompose into an active species on the electrode surface and 2) the catalyst is only active when attached to the surface. To probe the first of these concerns, the F.E.(O_2) with $FeCl_2$ and ligand modified WO_3 has been carried out. When WO_3 is modified with the ligand, no improvement in F.E.(O_2) is observed. In fact, in the case of anchoring the ligand to WO_3, production of O_2 becomes moderately inhibited. Examples of this experiment can be found in Figure Figure B.7.

In order to address the concern about the active species being directly anchored to the electrode surface for improved F.E.(O_2), in separate experiments, **Fe-1** or **Fe-2** are added to the electrolyte at comparable concentrations to the surface coverage. In both instances, no improvement in F.E.(O_2) is observed. In fact, the F.E.(O_2) is slightly decreased. The decrease in F.E.(O_2) is likely due to some competitive light absorption by the catalyst in solution since the solutions are faintly colored (see Figure Figure B.8). Another way this concern is addressed by replacing the electrolyte after 3 hours of illumination and repeating the F.E.(O_2) measurement on the same film. For **Fe-2** on WO_3, the F.E.(O_2) is maintained after replacing the electrolyte (Figure 3.13). These results support the notion that the catalyst must be anchored in order to oxidize water under illumination, and that the active catalytic species remains bound to the WO_3 in some capacity up to 6 hours.

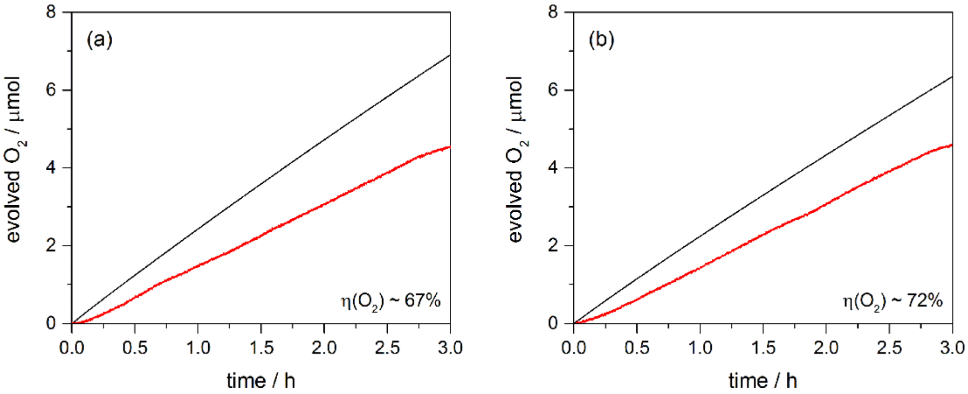

Figure 3.13 Faradaic efficiency of **Fe-2** on WO_3 over two trials (a) and (b) with fresh 100 mM Na_2SO_4 pH 3 under 1 sun illumination at 1.23 V vs. RHE; determined from theoretical yield (black) and actual yield (red) of O_2

3.5 Characterization of Fe WOCs on WO_3 after Photoelectrochemistry

Alongside photoelectrochemical *in situ* control experiments, Raman and UV-Vis spectroscopy are performed to probe the identity of the active species on the electrode surface after carrying out photoelectrochemistry, (Figure Figure B.9 and Figure B.10). In both instances, no ligand vibrational modes and MLCTs bands are visible on the electrode surface after electrolysis. The lack of spectroscopic signatures suggests that the surface coverage decreases significantly during electrolysis, or that the catalyst is decomposing.

To address these possibilities, non-aqueous CV traces (identical conditions to Figure 3.6) of the electrode recorded after electrolysis is used as well. However, no electrochemical events corresponding to the original catalyst are observed (Figure Figure B.11) after electrolysis. This result could be due to the observation that when the catalyst achieves higher oxidation states, the electrochemical potentials and redox reactions change significantly. Although these results strongly suggest the catalyst has been removed from the surface, it does not provide evidence for the active catalytic species. Mass spectrometry recorded of the electrolyte after illuminating **Fe-2** on WO3 for 3 hours revealed no degradation of **Fe-2** in the electrolyte. Instead numerous high oxidation state **Fe-2** complexes are visible in the ESI-MS$^+$ as illustrated in Figure B.12 and summarized in Table 3.4. High oxidation state intermediates are required for the previously proposed mechanism for the molecular catalyst **Fe-1**.[8]

Peak	Molecular Species	m/z$^+$	Change to Ligand
1	$[Fe^{V}(\mathbf{2})(SO_4)_2(CH_3OH)]^+$	876.2	none
2	$[Fe^{V}(\mathbf{2\text{-}(OC_2H_5)_4})(SO_4)_2]^+$	732.0	deprotected
3	$[Fe(\mathbf{2\text{-}(OC_2H_5)_4})(H_2O)(CH_3OH)]^+$	590.1	deprotected
4	$[Fe^{V}(\mathbf{2})(SO_4)_2(H_2O)_3]^{2+}$	449.1	none
5	$[Fe^{V}(\mathbf{2\text{-}(OC_2H_5)_2})(SO_4)_2(CH_3OH)]^{2+}$	306.6	partially deprotected

Table 3.4 Summary of peaks from ESI-MS$^+$ of the 100 mM Na_2SO_4 electrolyte after bulk electrolysis with **Fe-2** on WO_3

Although ESI-MS$^+$ data suggests that the catalyst does not decompose in the electrolyte under continuous 1-sun illumination with WO_3, it is still possible that some ligand decomposition occurs under illumination on the WO_3 surface. This possibility would result in Fe remaining bound, but with no ligand structure being present. It would also be consistent with the CV after electrolysis wherein the active species simply cannot be reduced from the higher, active oxidation states. Therefore, XPS is used to probe for the presence of Fe on the WO_3 electrodes after electrolysis. XP spectroscopy reveals that no Fe 2p binding peaks at 707 and 721 eV appear, indicating that no iron is present on the surface of WO_3 after illumination (Figure Figure B.13). This result suggests that nanoparticles are not forming on the surface during electrolysis. In addition, SEM images are collected before and after electrolysis. SEM images in Figure Figure B.14 reveal no visible nanoparticles on the WO_3 surface before or after electrolysis. Furthermore, EDX mapping is inconclusive because no Fe can be detected before or after photoelectrochemistry is performed. This data coupled with the high solubility of iron oxide materials in acidic medium further suggests that Fe_2O_3 or FeOOH nano-particles are not the likely active species. Instead, the spectroscopic data suggests that the active species has completely dissociated from the WO_3 surface. However, this conclusion is in direct conflict with the F.E.(O_2) control experiments performed previously. Therefore, these results suggest that the active species remains attached to the surface at concentrations below the detection limits of spectroscopic techniques at disposal.

3.6 Conclusions

This work has successfully developed a flexible synthesis to readily modify **Fe-1** with the intention of anchoring a modified earth-abundant molecular WOC (**Fe-2**, **Fe-3**, and **Fe-4**) to a semiconducting photoelectrode in order to photoactivate the molecular WOC. This work is also the first example of quantifying the improvement in F.E.(O_2) when molecular catalysts are anchored to a semiconductor electrode. Coupled with the results obtained in Chapter 2, the improvement in photocurrent or F.E.(O_2) can play an important role in implicating the active mechanism or species on the electrode surface under illumination. The work described in this chapter has laid the foundation for exploring possible applications of this approach to complexes and various semiconductors.

3.7 Experimental Methods

General Methods. All reactions were carried out under a nitrogen atmosphere unless otherwise noted. THF, CH_3CN, and CH_2Cl_2 were dried prior to use according to common practices. All other materials were obtained from commercial sources, and used as purchased. Column chromatography was performed using standard 200 mesh silica gel. Elemental analyses were performed by Atlantic Microlab, Inc. for C, H, N, and Cl determinations. ^{1}HNMR and ^{13}CNMR spectra were recorded in $CDCl_3$ or CD_3CN using a Varian MR400 at 400 MHz. Electrospray ionization mass spectra were collected on a Micromass LCT TOF MS through a Waters 1525 GC. UV/Visible/NIR spectroscopy was performed on an Agilent CaryWin 5000.

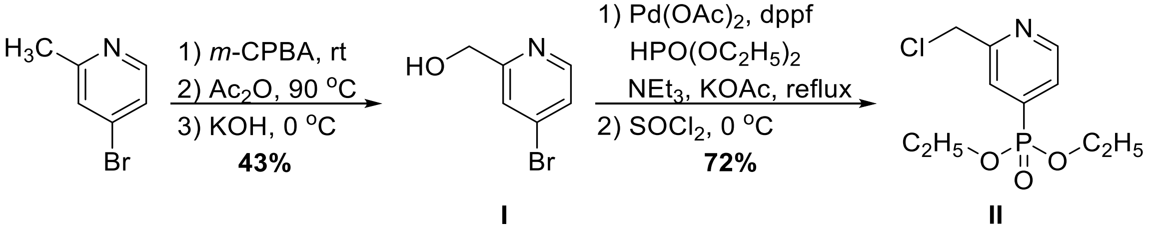

Preparation of I[23]: 4-bromo-2-methylpyridine (4.30 g, 25.0 mmol) in 100 mL $CHCl_3$ was stirred with 70 wt% *m*-CPBA (8.01 g, 32.5 mmol) open to air for 2 hours. The reaction was quenched with 15 mL saturated $NaHCO_3$, and the resulting layers were separated. The aqueous layer was extracted with 30 mL CH_2Cl_2 (2×). The combined organic layers were washed with 30 mL of 2 M HCl, dried with Na_2SO_4, filtered, and concentrated.

The resulting yellow oil was dissolved in 50 mL acetic anhydride and heated to 90 ºC under air overnight. The dark solution was concentrated by vacuum distillation, and the residue was cooled to room temperature and dissolved in 30 mL methanol. The resulting solution was cooled to 0 ºC. KOH (2.8 g, 50.0 mmol) was added to the chilled solution, and upon complete addition the ice bath was removed. The solution was warmed to room temperature and stirred for 3 hours. The reaction was concentrated under reduced pressure. The dark residue was taken up into 50 mL ethyl acetate and washed with saturated $NaHCO_3$. The aqueous layer was extracted with additional ethyl acetate (2× 50 mL) and the combined organic layers were dried with Na_2SO_4, filtered, and concentrated. The crude product was purified on silica with 50% ethyl acetate/hexanes. The desired alcohol **I** (2.04 g) was isolated in 43% yield over three steps. ^{1}HNMR($CDCl_3$, ppm): 8.32 (d, 1H), 7.49 (s, 1H), 7.345 (d, 1H), 4.71 (s, 2H), 4.13 (broad, 1H); ^{13}CNMR(ppm): 161.13, 149.17, 133.79, 125.78, 124.11, 63.91; ESI-MS$^+$: [**I**+H]$^+$ = 187.2 m/z

Preparation of II[24]: Palladium acetate (8.5 mg, 0.038 mmol), dppf (42.0 mg, 0.076 mmol), and KOAc (16 mg, 0.17 mmol) were dissolved in 5 mL THF. Triethylamine (0.27 mL, 1.9 mmol) was added to the reaction and the solution was heated to 70 ºC under N_2 for 15 minutes. To the hot reaction, diethyl phosphite (0.16 mL, 1.27 mmol) and **I** (250 mg, 1.33 mmol) were added and the reaction was refluxed overnight. The reaction was cooled to room temperature and the reaction was concentrated under reduced pressure.

The crude residue was then taken into 5 mL of CH_2Cl_2 and cooled to 0 ºC. Thionyl chloride (0.27 mL, 3.70 mmol) in 3 mL CH_2Cl_2 was added dropwise over 5 minutes. The resulting suspension was warmed to room temperature and stirred for 4 hours in air. The reaction was concentrated, and the brown residue was taken into 25 mL CH_2Cl_2 and washed with 25 mL saturated $NaHCO_3$. The resulting aqueous layer was extracted with CH_2Cl_2 (2× 25 mL) and the combined organic layers were washed with brine. Finally, the organic layer was dried with Na_2SO_4, filtered, and concentrated under reduced pressure. This yielded the desired product **II** (239 mg) as a brown residue that was sufficiently pure by NMR in 72% yield over two steps. ^{1}HNMR($CDCl_3$, ppm): 8.68 (t, 1H), 7.80 (d 1H), 7.57 (dd, 1H), 4.68 (s, 2H), 4.13 (m, 4H), 1.31 (t, 6H); ^{13}CNMR(ppm): 157.10, 149.69, 139.81, 124.535, 124.34, 62.835, 46.20, 16.30; ^{31}PNMR(ppm): 14.0; ESI-MS$^+$: [**II**+H]$^+$ = 263.9 m/z

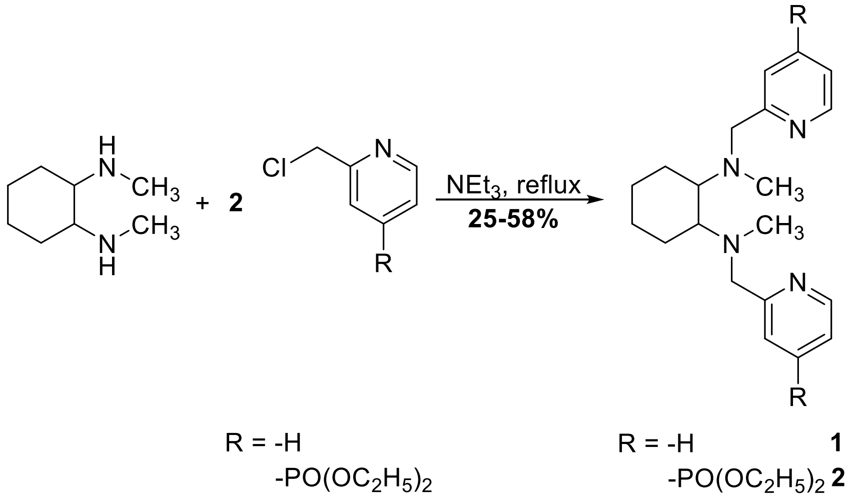

General Preparation of 1 or 2: The racemic cyclohexane diamine (54 mg, 0.38 mmol) was dissolved in 5 mL of acetonitrile. Triethylamine (0.16 mL, 1.13 mmol) and **II** (199 mg, 0.76 mmol) were added to the stirring solution. The reaction was heated to 100 ºC and attached with a long reflux condensor. After heating the reaction overnight, it was cooled to room temperature and concentrated under reduced pressure. The residue was dissolved in 10 mL CH_2Cl_2 and washed with 10 mL saturated $NaHCO_3$. The aqueous layer was extracted an additional 2 times with CH_2Cl_2. The combined organic layers were dried with Na_2SO_4, filtered, and concentrated. The crude product was purified on silica with 86% ethyl acetate, 10% methanol, and 4% conc. NH_4OH (R_f ~0.5). Fractions collected from the column were dried with Na_2SO_4, filtered, and concentrated under reduced pressure. This yielded an orange oil (173 mg, 58%). ^{1}HNMR($CDCl_3$, ppm): 8.58 (t, 2H), 7.875 (d, 2H), 7.455 (q, 2H), 4.09 (m, 8H), 3.91 (s, 4H), 2.575 (d, 2H), 2.28 (s, 6H), 1.875 (d, 2H), 1.68 (d, 2H), 1.25 (m, 14H), 1.07 (t, 2H); ^{13}CNMR(ppm): 148.98, 138.52, 136.69, 124.41, 123.22, 63.95, 62.63, 60.86, 36.78, 26.93, 25.64, 16.27; ^{31}PNMR 15.26; ESI-MS$^+$: [**2**+H]$^+$ = 597.0 m/z$^+$

1: exhibited poor separation (400 mg, 25%); ^{1}HNMR($CDCl_3$, ppm): 8.46 (dd, 2H), 7.545 (m, 4H), 7.08 (q, 2H), 3.83 (q, 4H), 2.635 (d, 2H), 2.27 (s, 6H), 1.955 (d, 2H), 1.735 (d, 2H), 1.28 (d, 2H), 1.13, (d, 2H); ^{13}CNMR(ppm): 161.44, 148.57, 136.17, 122.77, 121.48, 6456, 60.46, 36.62, 25.84; ESI-MS$^+$: [**1**+H]$^+$ = 323.8 m/z

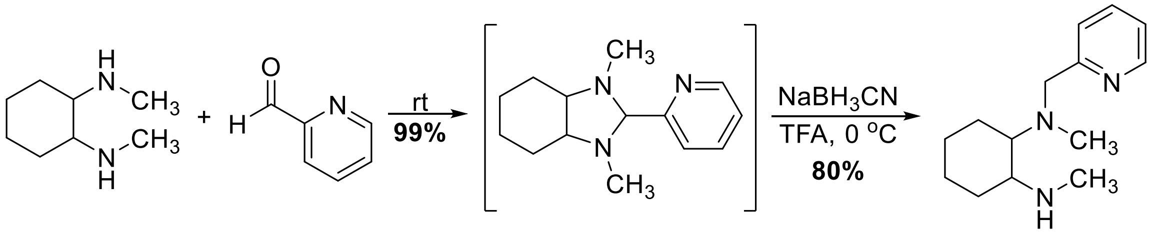

III

IV

Preparation of IV: *N*,*N*'-dimethyl-*trans*-1,2-cyclohexyldiamine (0.75 mL, 4.76 mmol) and 2-pyridine carboxaldehyde (0.46 mL. 4.76 mmol) were stirred in 50 mL chloroform at room temperature in air for 1 hour. The reaction was concentrated *in vacuo*, and yielded a light yellow oil, which was the desired intermediate (**III**). **III** (1.10 g, 4.76 mmol) was dissolved in 50 mL MeOH, and the reaction was cooled to 0 °C for 15 minutes. Whereupon $NaBH_3CN$ (0.30 g, 4.76 mmol) was added to the solution in one portion. The reaction was stirred for 15 minutes, and trifluoroacetic acid (0.73 mL, 9.52 mmol) was added dropwise to the reaction. The reaction was warmed to room temperature and stirred an additional 3 hours. After 3 hours, the reaction was cooled to 0 °C, and an aqueous solution of 1 M NaOH was added until the solution was basic. MeOH was removed from the solution, and the resulting aqueous layer was extracted with CH_2Cl_2 (3 x 50 mL). The combined organic layers were washed with 100 mL brine, dried with Na_2SO_4, filtered, and concentrated *in vacuo*. The resulting yellow oil (0.890 g, 80% yield) was sufficiently pure for following reactions. ^{1}HNMR($CDCl_3$, ppm): 8.475 (dd, 1 H), 7.62 (dt, 1H), 7.36 (d, 1H), 7.11 (t, 1H), 3.665 (q, 2H), 2.38 (m, 4H), 2.26 (m, 1H), 2.18 (s, 3H), 2.10 (d, 1H), 1.88 (m, 1H), 1.77 (d, 1H), 1.68 (d, 1H), 1.20 (m, 4H), 1.03 (m, 1H); ^{13}CNMR(ppm): 160.24, 148.94, 136.59, 122.48, 121.89, 66.60, 60.25, 59.14, 37.16, 33.41, 30.60, 25.38, 24.55, 22.27; ESI-MS$^+$: [**IV**+H]$^+$ = 234.2

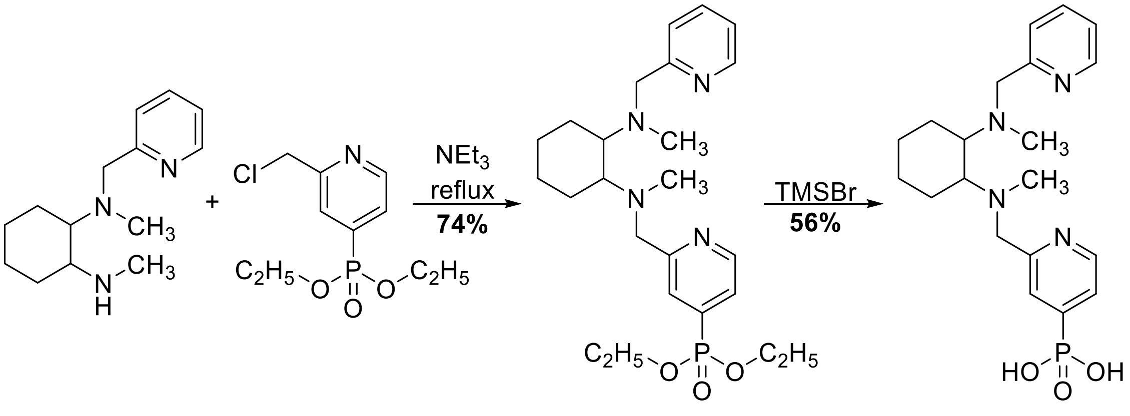

3 **4**

Preparation of 3: Dissolved **IV** (0.808 g, 3.46 mmol) in 50 mL CH_3CN. Added NEt_3 and **II** to the solution. The reaction was heated to reflux for 2 hours. Upon cooling the reaction to room temperature, the solvent was removed *in vacuo*, and the resulting red oil was dissolved in 100 mL CH_2Cl_2. The organic layer was washed with sat. $NaHCO_3$ (50 mL). The aqueous layer was extracted an additional 2 x with CH_2Cl_2 (50 mL). The combined organic layers were washed with brine (100 mL), dried with Na_2SO_4, filtered, and concentrated *in vacuo*. The result red oil was purified by column chromatography on neutral alumina using 5% MeOH in EtOAc (R_f = 0.4). The desired product was obtained as a dark orange oil (1.177 g, 74% yield). ^{1}HNMR($CDCl_3$, ppm): 8.46 (s, 1H), 8.32 (s, 1H), 7.59 (m, 2H), 7.46 (m, 1H), 7.14 (m, 1H), 4.14 (m, 10H), 3.26 (m, 1H), 2.96 (s, 1H), 2.64 (m, 2H), 2.34 (m, 2H), 1.82 (s, 2H), 2.23 (m, 1H), 2.07 (m, 1H), 1.77 (s, 2H), 1.23 (m, 8H), 1.00 (m, 1H); ^{13}CNMR(ppm): unable to resolve all peaks due to asymmetry; ^{31}PNMR(ppm): 15.09; ESI-MS$^+$: [**3**+H]$^+$ = 461.2

Preparation of 4: Dissolved **3** (0.206 g, 0.447 mmol) in 3 mL anhydrous CH_2Cl_2. Fresh trimethylsilyl bromide (0.580 mL, 4.47 mmol) was added to the reaction in a N_2 atmosphere. The reaction was stirred at room temperature. After 48 hours, the reaction was quenched by slowly adding 3 mL MeOH and concentrated *in vacuo*. The resulting brown oil was triturated with acetonitrile (~10 mL) which resulted in a white precipitate. When the white precipitate was left to dry it reformed a brown oil. The brown oil was the pure, desired ligand (0.130, 56% yield). ^{1}HNMR(CD_3OD, ppm): 8.88 (s, 1H), 8.66 (m, 1H), 8.27

(d, 1H), 8.05 (m, 1H), 7.92 (m, 1H), 7.77 (broad, 2H), 4.56 (q, 4H), 3.53 (s, 2H), 2.99 (s, 3H), 2.76 (s, 1H), 2.39 (m, 2H), 2.28 (s, 1H), 2.18 (m, 1H), 1.89 (m, 2H), 1.70 (d, 1H), 1.44 (m, 3H); ^{13}CNMR(ppm): unable to resolve due to asymmetry; ^{31}PNMR(ppm): 9.45; ESI-MS^{+}: [**4**+H]$^{+}$ = 405.2

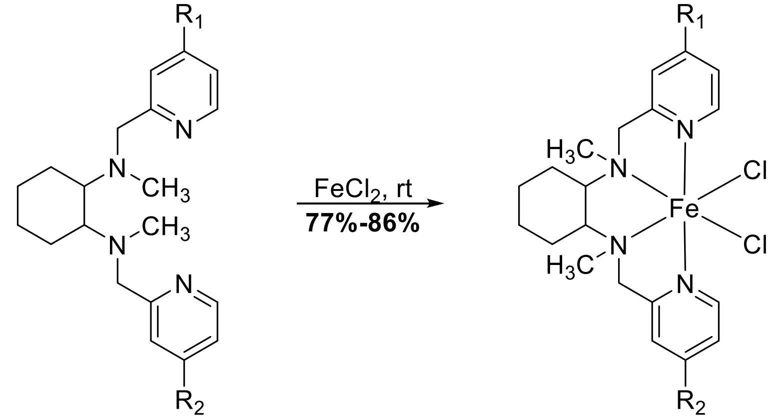

R$_1$ = R$_2$ = -H **1**
-PO(OC$_2$H$_5$)$_2$ **2**
R$_1$ = -H
R$_2$ = -PO(OC$_2$H$_5$)$_2$ **3**
-PO(OH)$_2$ **4**

R$_1$ = R$_2$ = -H **Fe-1**
-PO(OC$_2$H$_5$)$_2$ **Fe-2**
R$_1$ = -H
R$_2$ = -PO(OC$_2$H$_5$)$_2$ **Fe-3**
-PO(OH)$_2$ **Fe-4**

General Preparation of Fe-1, Fe-2, Fe-3, Fe-4^{25}: 1.0 eq. of ligand was added to 5 mL acetonitrile under N_2. To the stirring solution, 1.0 eq. of anhydrous $FeCl_2$ was added, and the reaction immediately changed colors. The reaction was stirred overnight and concentrated under reduced pressure. If a precipitate was present, the solid was isolated as the pure product and rinsed with diethyl ether. If no precipitate formed, the solution was concentrated and dried in a vacuum oven, yielding the pure complex. X-ray quality crystals were obtained by slow diffusion of ether into a concentrated solution of the complex in CH_3CN.

Fe-1: Yellow powder (419 mg, 77%); ^{1}HNMR(CD_3CN, ppm): 109.48, 63.25, 54.58, 51.27, 20.43, 15.46, 3.17, 2.49, 1.98, 0.10, -19.03; ESI-MS^{+}: [Fe(**1**)Cl(CH_3CN)]$^{+}$ = 423.4 m/z^{+}, [Fe(**1**)Cl_2•0.5H_2O] EA: (theory) C 52.20, H 6.35, N 12.17, Cl 15.41; (found) C 52.10, H 6.29, N 12.21, Cl 15.13

Fe-2: Purple powder (116 mg, 86%); ^{1}HNMR(CD_3CN, ppm): 108.3, 62.07, 51.92, 51.39, 14.90, 8.0, 3.94, 2.01, 1.43, 0.16, -2.18, -2.85, -11.73; ESI-MS^{+}: [Fe(**2**)Cl(CH_3CN)]$^{+}$

= 721.4 m/z$^+$; [Fe(**2**)(Cl)$_{1.7}$(HO)$_{0.3}$•0.7H$_2$O] EA: (theory) C 46.12, H 6.59, N 7.68, Cl 8.10; (found) C 45.27, H 6.47, N 7.67, Cl 8.06

Fe-3: Red powder (29 mg, 81%); ^{1}HNMR(CD$_3$OD, ppm): 8.15, 6.30, 3.51, 2.92, 2.50, 2.17, 1.72; ESI-MS$^+$: [Fe(**3**)Cl$_2$]$^+$ = 586.1.

Fe-4: Orange powder (51 mg, 78% yield); ^{1}HNMR(CD$_3$OD, ppm): 9.29, 8.68, 5.58, 4.72, 3.97, 2.93, 2.52, 1.89; ESI-MS$^+$: [Fe(ppmcn)+Li]$^{2+}$ = 234.2, [Fe(ppmcn)(H$_2$O)]$^{3+}$ = 157.9.

Sol-gel Synthesis of WO$_3$. WO$_3$ was prepared via a modified route that has been previously reported.[26] A Type 1 Dow-X cation exchange resin was activated by washing with 1 column volume of 3 M HCl. The column was then washed with Milli-pore H$_2$O until the pH was nearly neutral (~4 column volumes). A freshly prepared solution of NaWO$_4$×2H$_2$O (3.29 g) in 20 mL H$_2$O was added carefully to the exchange column. Initially, the eluent was collected into a waste beaker, however, the tungstic acid (eluent turned green) was collected into a stirring round bottom flask containing 25 mL EtOH. Once the tungstic acid finished eluting from the column, the waste beaker was replaced. The column was continually washed with water until the tungstic acid finished eluting and was further washed with 4 column volumes of H$_2$O. The column can be reused indefinitely following this procedure. After concentrating the tungstic acid to 20 mL *in vacuo*, 6.6 g of polyethylene glycol (300 MW PEG) is added to the colloid. The resulting colloid can be used to prepare films up to three days.

FTO was cleaned by sonication in acetone, EtOH, and water (15 minutes each), and dried under a stream N$_2$ gas. The clean FTO was masked with electrical tape to yield a 1 cm^2 area. 25 μL tungstic acid colloid was spread over the masked electrode area, and the electrode was spun at 2500 rpm for 30 seconds. After each layer, the films were annealed for 30 minutes at 500 °C. Once the films were cooled to room temperature, the process of spin coating was repeated until 10 layers were achieved. This produces electrodes that reproducibly obtain ~0.8 mA • cm^{-2} with an average thickness of ~1.8 μm.

Modification of WO$_3$ with [Fe]: WO$_3$ electrodes were heated to 60 ^{o}C in ~500 μM **[Fe]**/acetonitrile solution and sealed in a vial. The anodes were soaked for 8 hours in the dark and then rinsed with excess acetonitrile and dried with N$_2$. This procedure resulted in a light yellow tint to the modified electrodes.

Electrochemistry. All electrochemistry was performed on either a CH Instruments CHI-600 or CHI-1000 potentiostat. All potentials are referenced to SCE (saturated calomel electrode) with saturated KCl electrolyte reference electrode (RE), and Pt was used as the counter electrode (CE) in all experiments. Non-aqueous solvents were dried prior to use and $TBAPF_6$ was recrystallized from EtOH prior to use. Glassy carbon (GC) was used as the working electrode (WE) for solution-based electrochemistry. Aqueous solutions were prepared using 18.2 Ω Milli-pore H_2O and concentrated sulfuric acid, and then pH adjusted with 7 M NaOH to obtain the desired concentration and pH. The aqueous solutions were also purged with N_2 prior to use, but were not sealed under N_2. All photoelectrochemical measurements were carried out in custom-built cells with quartz viewing windows. All illumination was carried out using a Newport Oriel 150 W Xe lamp fitted with an AM1.5G filter from Newport whose power was adjusted to 100 mW/cm^2.

Faradaic Efficiency: Oxygen Detection. Oxygen was quantified using a FOSSPOR fluorescence probe using two-point calibration at 20.90% and 0.00% O_2. O_2 evolution experiments were carried out in a custom-built two-sided cell with quartz windows, where the O_2 probe, working electrode, and reference electrode were on one side, with the temperature probe and the Pt auxiliary electrode on the other side. The solutions were purged with N_2 overnight, and then sealed under N_2 on a Schlenk line. The photoelectrode was illuminated at 100 mW/cm^2 filtered with AM 1.5G and the potential was held at 809 mV *vs.* SCE in pH 3 Na_2SO_4 (1.23 V *vs.* NHE). After collecting a stable 0% baseline for ~30 minutes, the photoanode was illuminated for ~3 hours. Following illumination, the O_2 was allowed to reach a stable O_2 level for ~30 minutes to allow for temperature fluctuations with the probe. Finally, the run was successful if the O_2 returned near 20.90% after re-exposing the O_2 probe to air. Faradaic efficiency was determined by dividing the measured moles of O_2 by the theoretical yield, determined by dividing the total charge collected during the experiment by 4*F* (n = 4 e^-, *F* = 96,485.34 C/mol e^-).

Faradaic Efficiency: Non-oxygen Detection. Non-oxygen by-products from bulk electrolysis were measured by quantifying the amount of Fe^{2+} that was oxidized by the non-O_2 oxidants in solution (mainly $S_2O_8^{2-}$, HSO_5^-, and H_2O_2) according to the following reactions:

$$2\ Fe^{2+} + S_2O_8^{2-} \rightarrow 2\ Fe^{3+} + 2\ SO_4^{2-} \qquad \textbf{(1)}$$

$$2\ \mathrm{Fe}^{2+} + \mathrm{HSO}_5^- + 2\mathrm{H}^+ \rightarrow 2\ \mathrm{Fe}^{3+} + \mathrm{HSO}_4^- + \mathrm{H}_2\mathrm{O} \qquad (\mathbf{2})$$

$$2\ \mathrm{Fe}^{2+} + \mathrm{H}_2\mathrm{O}_2 + 2\ \mathrm{H}^+ \rightarrow 2\ \mathrm{Fe}^{3+} + 2\ \mathrm{H}_2\mathrm{O} \qquad (\mathbf{3})$$

The amount of Fe^{3+} generated in the second reaction was quantified by addition of excess Na(SCN). The amount of Fe^{3+} generated was determined using Beer's law and 1 mol of Fe^{3+} was generated for every 1 mol of e^- not used to oxidize water completely, and thus the Faradaic efficiency of the cells for non-O_2 production was measured. To perform the reaction, 2.0 mL of 5 mM $FeSO_4$ in 100 mM pH 3 Na_2SO_4 and 1.0 mL of the test solution were mixed and equilibrated for 15 minutes to allow for the reaction to go to completion. NaSCN was added to the solutions (~40 mM) to generate the deep red $[Fe(SCN)_6]^{3-}$ species, detectable by UV-Vis spectroscopy ($\varepsilon = 172\ M^{-1}\ cm^{-1}$ at $\lambda_{max} = 465$ nm). The measurement was standardized using $Ce(HSO_4)_4$. If the reactions were not carried out in aerated solutions and during the time frame of the experiments then the detected concentrations of the non-O_2 oxidants was significantly diminished.

References

1 Chen, X.; Ren, X.; Liu, Z.; Zhuang, L.; Lu, J. *Electrochem. Commun.*, **2013**, *27*, 148.

2 Zhong, D. K.; Zhao, S.; Polyansky, D. E.; Fujita, E. J. Catal. 2013, 307, 140.

3 Fukuzumi, S.; Kato, S.; Suenobu, T. *Phys. Chem. Chem. Phys.* **2011**, *13*, 17960.

4 Zhang, B.; Li, F.; Yu, F.; Wang, X.; Zhou, X.; Li, H.; Jiang, Y.; Sun, L. ACS Catal. 2014, 4, 804.

5 Representative examples: a) Gillaizeau-Gauthier, I.; Odobel, F.; Alebbi, M.; Argazzi, R.; Costa, E.; Bignozzi, C. A.; Qu, P.; Meyer, G. J. *Inorg. Chem.*, **2001**, *40*, 6073. b) Park, H.; Bae, E.; Lee, J-J.; Park, J.; Choi, W. *J. Phys. Chem. B.*, **2006**, *110*, 8740

6 a) Elizarova, G. L.; Matvienko, L. G.; Lozhkina, N. V.; Parmon, V. N.; Zamaraev, K. I. *React. Kinet. Catal. Lett.* **1981**, *16*, 191; b) Elizarova, G. L.; Matvienko, L. G.; Lozhkina, N. V.; Maizlish, V. E.; Parmon, V. N. *React. Kinet. Catal. Lett.* **1981**, *16*, 285; c) Elizarova, G. L.; Matvienko, L. G.; Lozhkina, N. V.; Parmon, V. N. *React. Kinet. Catal. Lett.* **1983**, *22*, 49; d) Elizarova, G. L.; Matvienko, L. G.; Lozhkina, N. V.; Parmon, V. N. *React. Kinet. Catal. Lett.* **1984**, *26*, 67.

7 Barnett, S. M.; Goldberg, K. I.; Mayer, J. M. *Nat. Chem.* **2012**, *4*, 498.

8 Fillol, J. L.; Codolá Z.; Garcia-Bosch, I.; Gómez, L.; Pla, J. J.; Costas, M. *Nat. Chem.* **2011**, *3*, 807.

9 a) Delroisse, M.; Rabion, A.; Chardac, F.; Tétard, D.; Verlhac, J-B.; Fraisse, L.; Séris, J-L. *J. Chem. Soc., Che. Commun.*, **1995**, 949. b) Mialane, P.; Tchertanov, L.; Banse, F.; Sainton, J.; Girerd, J-J. *Inorg. Chem*, **2000**, *39*, 2440. c) England, J.; Gondhia, R.; Bigorra-Lopez, L.; Petersen, A. R.; White, A. J. P.; Britovsek, G. J. P. *Dalton Trans.*, **2009**, 5319.

10 Kalek, M.; Jezowska, M.; Stawinski, J. *Adv. Synth. Catal.* **2009**, *351*, 3207.

11 White, M. C.; Doyle, A. G.; Jacobsen, E. N. *J. Am. Chem. Soc.* **2001**, *123*, 7194.

12 Sato, M.; Mori, Y.; Iida, T. *Synthesis* **1992**, 539.

13 a) Arjan, H.; Boyd, Coumbarides, G. S.; Eames, J.; Jones, R. V. H.; Stenson, R. A.; Suggate, M. J. *Tetrahedron Lett.* **2005**, *46*, 1921; b)Jiang, X.; Liu, H.; Zheng, B.; Zhang, J. *Dalton Trans.* **2009**, 8714.

14 Chen, K.; Que, L., Jr. *Chem. Commun.* **1999**, 1375.

15 Cohen, A.; Kopilov, J.; Goldberg, I.; Kol, M. *Organometallics* **2009**, *28*, 1391.

16 Collins, M. J.; Ray, K.; Que, L., Jr. *Inorg. Chem.* **2006**, *45*, 8009.

17 Ellis, W. C.; McDaniel, N. D.; Bernhard, S.; Collins, T. J. *J. Am. Chem. Soc.* **2010**, *132*, 10990.

18 Harriman, A.; Pickering, I. J.; Thomas, J. M. *J. Chem. Soc., Faraday Trans. 1* **1988**, *84*, 2795.

19 Representative examples: a) Wrighton, M. S.; Ginley, D. S.; Wolczanski, P.T.; Ellis, A. B.; Morse, D. L.; Linz, A. *Proc. Nat. Acad. Sci. USA* **1975**, *72*, 1518; b) Yourey, J. E.; Bartlett, B. M. *J. Mater. Chem.* **2011**, *21*, 7651.

20 a) Mi, Q.; Zhanaidarova, A.; Brunschwig, B. S.; Gray, H. B.; Lewis, N. S. *Energy Environ. Sci.* **2012**, *5*, 5694; b) Mi, Q.; Coridan, R. H.; Bruschwig, B. S.; Gray, H. B.; Lewis, N. S. *Energy Environ. Sci.* **2013**, DOI 10.1039/C3EE40712H.

21 Hill, J. C.; Choi, K-S. *J. Phys. Chem. C* **2012**, *116*, 7612.

22 Giokas, P. G.; Miller, S. A.; Hanson, K.; Norris, M. R.; Glasson, C. R. K.; Concepcion, J. J.; Bettis, S. E.; Meyer, T. J.; Moran, A. M. *J. Phys. Chem. C* **2013**, *117*, 812.

23 Deng, L.; Diao, J.; Chen, P.; Pujari, V.; Yao, Y.p Cheng, G.; Crick, D. C.; Prasad, B. V. V.; Song, Y. *J. Med. Chem.* **2011**, *54*, 4721-4734.
24 Kalek, M.; Jeowska, M.; Stawinski, J. *Adv. Synth. Catal.* **2009**, *351*, 3207-3216.
25 Costas, M.; Que, L. Jr. *Angew. Chem. Int. Ed.* **2002**, *41*, 2179-2181.
26 Santato, C.; Odziemkowski, M.; Ulmann, M.; Augustynski, J. *J. Am. Chem. Soc.* **2001**, *123*, 10639-10649.

Chapter 4

Anchoring a Molecular Iron Catalyst to Other Semiconductors

4.1 Introduction

In Chapter 3 we demonstrated the ability of **Fe-2** to improve the photoelectrochemical performance of WO_3 in acidic electrolytes.[1] However, these results give rise to an important question: How does the semiconductor impact the photoelectrochemical performance of the hybrid electrode? To date, Fe_2O_3 and WO_3 are the only semiconductors that have been used to activate molecular catalysts.[1,2,3] The best rational that has been provided to date is that these semiconductors are easily prepared and they exhibit favorable photophysical properties. For Fe_2O_3, the material has a small band gap (E_g = 2.1 eV) and absorbs longer wavelengths in the visible spectrum.[4] WO_3 has high hole mobility to increase the number of holes that reach the surface.[5]

However, both of these materials possess indirect band gaps, which means that both materials require some additional angular momentum from a simultaneously absorbed (or emitted) phonon (commonly from lattice vibrations) in order to be excited into the conduction band after absorption.[6] Therefore, there is a lower probability of both species being absorbed simultaneously leading to lower absorption coefficients. As a result, semiconductors with a direct band gap should exhibit better performance when modified with **Fe-2** because the probability of absorbing photons close to E_g is much higher. A higher amount of light absorption should result in more electron-hole pairs being generated in the semiconductor, and more holes should reach the surface. The best way to compare this phenomenon is through comparing the external quantum efficiency (EQE, as described in Equation 4.1 where I_{sc}(A) = short circuit current, P(W) = power of incident photons, and λ(nm) = wavelength of light absorbed) for various semiconductors at a wavelength of light both materials absorb strongly. For instance, both WO_3 and $BiVO_4$ absorb visible light at 420 nm, but $BiVO_4$ converts significantly more incident photons to current (73% vs. 34%

at 420 nm) than WO_3 because it has a direct band gap and WO_3 does not.[7,8]

$$EQE\ \% = \frac{I_{sc}(A)}{P(W)} \times \frac{1240}{\lambda(nm)} \times 100 \qquad (4.1)$$

With this idea in mind, we first want to compare the photoelectrochemistry of **Fe-2** on $BiVO_4$ with the photoelectrochemistry of **Fe-2** on WO_3. In addition to examining $BiVO_4$, we also want to compare materials with different electronic structures. The different semiconductors examined are included in Figure 4.1 and Table 4.1. The important consideration here is that each material has very different photophysical properties (e.g. electron diffusion length, hole diffusion length, absorptivity coefficient) along with different electronic properties (e.g. band-gap energy, conduction/valence band position, band composition). However, there are two important features that are thought to be most important for activating molecular catalysts. First, the band edges must be properly aligned energetically with the HOMO of the active water oxidation species. Second, the smaller the band gap the greater the photocurrent enhancement will be.

Fe-2 on metal oxide	**E_g, eV**	**EQE**	**α at λ_{max}**
TiO_2	3.1	0% above 400 nm	a = 1.2×10^6 cm^{-1} @ 290 nm
WO_3	2.7	15-34% @ 420 nm	a = 4.7×10^5 cm^{-1} @ 270 nm
$CuWO_4$	2.4	0.94% @ 420nm	a = 7.0×10^3 cm^{-1} @ 400 nm
Fe_2O_3	2.1	18% @ 420 nm	a = 3.9×10^5 cm^{-1} @ 400 nm
$BiVO_4$	2.4	73% @ 420 nm	a = 3.4×10^5 cm^{-1} @ 300 nm

Table 4.1 Summary of common electronic properties semiconductors to be modified with **Fe-2** [4,7, 9,10,13-16]

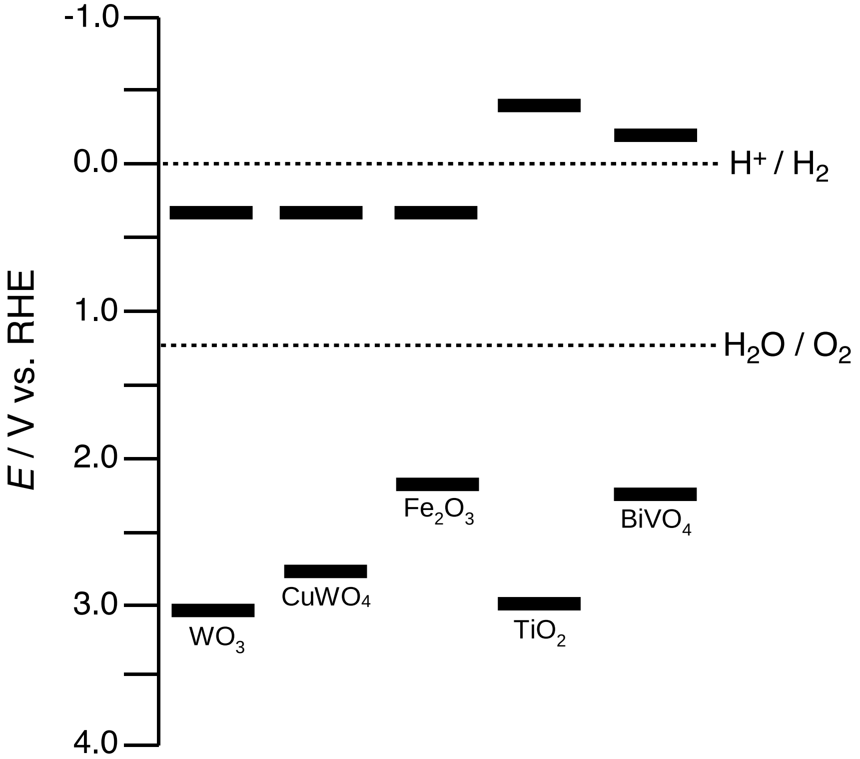

Figure 4.1 Potential energy diagram of semiconductors screened by anchoring **Fe-2**

4.2 Anchoring a Molecular Iron Catalyst to Other Semiconductors

$BiVO_4$ is used as the first material of comparison because it has a smaller, direct band gap compared to WO_3. When $BiVO_4$ is modified with **Fe-2**, the bright yellow electrode exhibits discoloration after soaking 8 hours in acetonitrile at 60 °C. Furthermore, the dark linear sweep voltammograms for **Fe-2** on $BiVO_4$ does not exhibit the redox couple associated with **Fe-2** in solution at ~0.7 V vs. RHE for the $Fe^{2+/3+}$ redox couple because the open circuit voltage of $BiVO_4$ is higher than that potential. Therefore, the identity of the catalyst on the surface cannot be definitively concluded. However, there is an overall increase in the dark current through the LSV trace (Figure C.1), and the earlier onset of dark electrocatalysis suggests the active species is likely bound to the surface.

Under chopped light illumination, the modified electrode displays delayed onset of photocurrent. At 1.23 V vs. RHE, there is a large decrease (-65%) in the amount of photocurrent observed when **Fe-2** is anchored to the surface. However, at much higher potentials (>1.7 V vs. RHE), the modified electrode generates more photocurrent than the bare $BiVO_4$. In addition to displaying more photocurrent at high overpotentials, at lower potentials, the modified semiconductor exhibits slow onset of photocurrent when the light as turned on and off. This observation is in direct contrast to **Fe-2** on WO_3 and the bare $BiVO_4$ where the onset of photocurrent is nearly instantaneous and often displays an exponential decay (transient photocurrent), which is associated with initial charge separation from the ground state in the dark. The lack of transient photocurrent suggests that the catalyst is not activated as quickly as the charge is being separated when illumination is resumed.

The observation of slow separation of charge is comparable to that observed for **Ru-P₂** and **Ru₂-P₂** on TiO_2 in Chapter 2. To examine this observation further and draw a closer comparison between catalytic systems and semiconductors, **Fe-2** is anchored to TiO_2. After modifying TiO_2 for 8 hours at 60 °C in acetonitrile, the translucent white TiO_2 electrodes have a yellow tint to the surface. UV-Vis spectroscopy of these films before photoelectrochemistry supports the presence of **Fe-2** on the electrode surface after soaking and rinsing the electrode thoroughly (as depicted in Figure C.2). Furthermore, when the modified electrode is placed in the pH 3 Na_2SO_4 electrolyte, the open circuit potential rests at 0.7 V vs. RHE, which aligns perfectly with the observed $Fe^{2+/3+}$ redox couple for **Fe-2** in solution. When a dark linear sweep is performed in the aqueous electrolyte, the $Fe^{2+/3+}$ redox couple is clearly evident as displayed in Figure C.3.

Chopped light illumination reveals a delayed onset of photocurrent as observed for **Fe-2** on $BiVO_4$ and the ruthenium catalysts on TiO_2. This result further supports the explanation that charge separation between the active species and the semiconductor is slow. However, the question then becomes what is slowing down charge separation? Because it has already been demonstrated that WO_3 rapidly collects holes from **Fe-2** under illumination, there must be some explanation for the difference in charge separation. The most likely explanation is depicted in Figure 4.2. This figure depicts the electrochemical potential energy differences between the semiconductor and the active state that has previously been demonstrated for **Fe-2**.[11]

To delve into this idea more deeply, when a semiconductor is placed in contact with an electrolyte, its Fermi level (E_f) must equilibrate with the solution-based redox couple. In the case of anchoring **Fe-2** to a semiconductor, the E_f of the semiconductor can

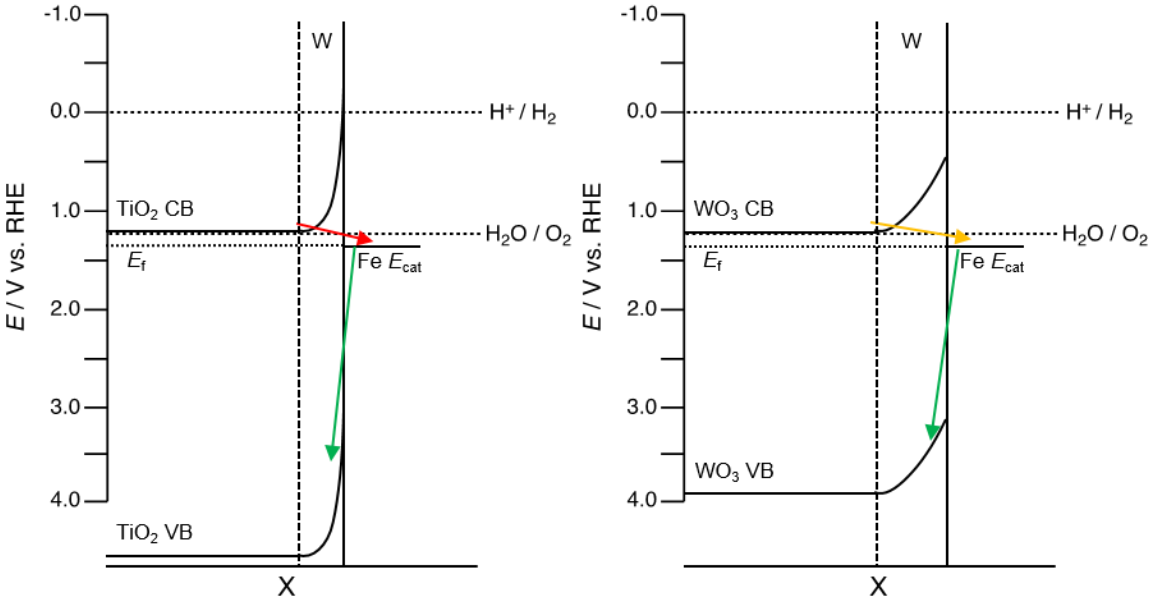

Figure 4.2 Energy diagrams of *n*-type TiO_2 and WO_3 in contact with electrolyte and the active species where the red arrow is competitive back electron transfer, the yellow arrow is slower back electron transfer, and the green arrows are the desired electron transfer; W is the depletion width, VB is valence band, and CB is conduction band

equilibrate with either **Fe-2** or with the electrolyte. The result of this equilibration is a change in the measured open-circuit potential when the electrode is placed in contact with the electrolyte.[6]

Because the open-circuit potential typically aligns with the $Fe^{2+/3+}$ redox couple when a modified electrode is placed in electrolyte, E_f is most likely equilibrating to the active species on the electrode surface. As a result of this equilibration, the E_f of different semiconductors will necessarily shift more or less to align with **Fe-2** depending on the initial E_f of the semiconductors. When the bands bend more, the depletion width of the material decreases. The depletion width is inversely proportional to the majority carrier donor density (N_D). As noted in Table 4.2, the N_D's for $BiVO_4$ and TiO_2 at E_{cat} (1.35 V vs. RHE) for **Fe-2** are much higher than the N_D's for WO_3, $CuWO_4$, and Fe_2O_3. As a result, the depletion width is much smaller for $BiVO_4$ and TiO_2 during photoelectrocatalysis with **Fe-2** on the surface. A decrease in depletion width causes the distance required for electron tunneling back to the surface to be reduced. Therefore, it is hypothesized that if the conduction band (and for *n*-type semiconductors, the E_f) is too high in potential energy then back electron transfer from the conduction band to the active species will be competitive with electron transfer from the active species to the valence band.

Based on this hypothesis, in the case of TiO_2, linear sweep experiments voltammetry under illumination will result in saturated photocurrent at lower potentials. When the film is constantly illuminated during a linear sweep experiment, the photocurrent is slightly higher than for the chopped light experiment, as depicted in Figure C.4. Varying the frequency of chopping the light will provide more concrete evidence for this hypothesis. Additionally, it is hypothesized that if the scan rate of the experiment is decreased an order of magnitude, then modified electrode should have more time to equilibrate between back and forward electron transfer, and the photocurrent should reach saturation more quickly. In fact, when the rate of the linear sweep is decreased from 20 mV/s to 2 mV/s, the modified electrode reaches higher photocurrents at much lower potentials (Figure C.5). Although linear sweep voltammetry is not an equilibrium measurement, as the scan rate decreases the electrode measures currents closer to the equilibrium between the electrode and solution. To take this experiment one step further, 0.2 mV/s would confirm this assignment. Transient absorption spectroscopy would also be useful to quantitatively probe this hypothesis, but we do not have the means for obtaining that measurement.

Further evidence for this explanation is obtained when the conduction band of the semiconductor is lowered to a similar energy as WO_3 using $CuWO_4$ and Fe_2O_3. Although the orbitals that comprise the conduction band are not the same in each case, the overall energy of the conduction band is similar (~0.4 V vs. RHE).[4,12,13] Additionally, this similarity in conduction band edge allows us to examine the impact of band gap and absorptivity of the semiconductors without altering the type of band gap (all three materials have indirect band gaps) and the conduction band energy. As can be seen in Table 4.1, the absorptivity of the semiconductors at their maximum absorption are comparable (albeit at different wavelengths) and the ability to use the incident photons can also be comparable (at the same wavelengths).[8,14,15,16]

When **Fe-2** is anchored to $CuWO_4$ and Fe_2O_3, the open circuit potentials for $CuWO_4$ and Fe_2O_3 shift from ~0.5 to 0.7 V vs. RHE and 0.4 to 0.7 V vs. RHE respectively, which suggests that **Fe-2** is successfully bound to the surfaces. The dark linear sweep for $CuWO_4$ reveals the $Fe^{2+/3+}$ redox couple for **Fe-2** (Figure C.6 and Figure C.7), but there is not an early onset in electrocatalytic water oxidation. For Fe_2O_3, the dark portion of the chopped light linear sweep reveals minimal evidence of the $Fe^{2+/3+}$ redox couple, but there is a lot of transient photocurrent that precludes any solid conclusions from being drawn.

In both cases, during chopped light linear sweeps, the photocurrent increases significantly when the corresponding semiconductor is modified with **Fe-2**. In the case of $CuWO_4$, a 100% enhancement is observed in Figure 4.3. For Fe_2O_3, a 270% enhancement is observed in Figure C.9. These results are consistent with the notion that as the band gap decreases, the photocurrent enhancement increases with **Fe-2** on the surface. However, it is important to consider the practicality of using electrodes comparable to $CuWO_4$ and Fe_2O_3 that achieve such low photocurrent densities. In this instance, despite the fact that **Fe-2** on WO_3 does not result in as much photocurrent enhancement, the actual photocurrent is significantly greater (Table 4.2). This result leads to the next important question: if better performing electrodes of $CuWO_4$ or Fe_2O_3 are prepared, how does the different synthesis method impact the photoelectrochemical enhancement?

Metal Oxide	**N_D, cm^{-3}**	**E_g, eV**	**j_{ph} at 1.23 V vs. RHE, μA • cm^{-2}**	**% increase**
TiO_2	3.74×10^{21} [a]	3.1	18	-67
WO_3	1.28×10^{20} [a]	2.7	1,180	60
$CuWO_4$	1.50×10^{20} [b]	2.4	36	up to 102
Fe_2O_3	5.84×10^{20} [c]	2.1	12	273
$BiVO_4$	1.58×10^{23} [b]	2.4	46	-45

Table 4.2 Summary of photocurrent increase for various semiconductors after anchoring **Fe-2** to the surface in pH 3 Na_2SO_4 under AM 1.5G 100 mW cm^{-2} illumination; N_D is reported at 43.75 (a) or 55.41 (b) Hz at 1.35 V vs. RHE (E_{cat} for **Fe-2**); (c) Fermi level pinning for Fe_2O_3 is observed at 1.35 V vs. RHE therefore N_D is reported for 55.41 Hz at 1.05 V vs. RHE[17,18,19,20,21]

4.3 Anchoring a Molecular Iron Catalyst to $CuWO_4$

At first glance, Fe_2O_3 seems like an ideal semiconductor to pursue in order to answer the question that arose in the previous section about the impact of the synthetic method for the electrode on photoelectrochemical enhancement when modified with **Fe-2**. However, Fe_2O_3 traditional exhibits low stability in acidic solutions due to its Lewis basic nature. In conjunction with this property, Fe_2O_3 has been shown previously to operate much more efficiently under alkaline conditions. But, the catalyst **Fe-2** and its anchoring groups

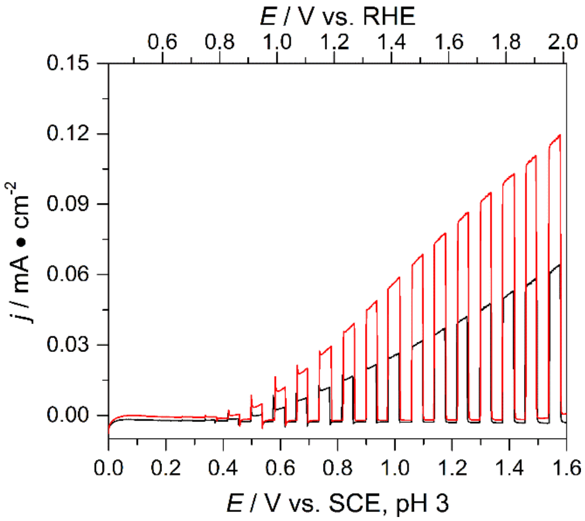

Figure 4.3 Chopped light linear sweep voltammetry of **Fe-2** on $CuWO_4$ (red) compared to bare $CuWO_4$ (black) prepared by spray pyrolysis under AM 1.5G 100 mW cm^{-2} illumination in 100 mM Na_2SO_4 pH 3 at 20 mV s^{-1} using Pt CE and SCE RE

have both demonstrated instability at pH greater than 9. [22,23] As a result, Fe_2O_3 is untenable for examining the impact of synthetic method on photoelectrochemical enhancement because the semiconductor will not be operating at its optimal pH.

On the other hand, $CuWO_4$ has demonstrated excellent stability over a wide range of pH from highly acidic to mildly alkaline (up to pH 9).[24] Furthermore, we have developed multiple methods for preparing $CuWO_4$ electrodes in our lab including spray pyrolysis, sol-gel processing, and single crystal molten salt growth. Additionally, $CuWO_4$ allows us to answer additional questions about **Fe-2**’s activity under illumination that cannot be answered using WO_3. For example, what is the pH stability of **Fe-2** when anchored to an electrode surface? How does the selectivity of the **Fe-2** modified semiconductor change when the unmodified semiconductor already exhibits 100% selectivity?

To begin answering these questions, four synthetic methods are employed to prepare $CuWO_4$. The original hypothesis is that if **Fe-2** is anchored to any $CuWO_4$ electrode, then the enhancement of photocurrent should be similar. As discussed in the previous section, when $CuWO_4$ prepared by spray pyrolysis is soaked with **Fe-2** in acetonitrile for 8 hours at 60 °C, the catalyst is readily adsorbed to the surface. After rinsing, the surface coverage can be electrochemically measured using the bulk electrolysis experiment described previously in Chapters 2 and 3. After modification, **Fe-2**’s coverage on the $CuWO_4$ surface is ~0.55 nmol cm^{-2}. This surface coverage is significantly lower coverage than is observed for **Fe-2** on WO_3. The likely explanation for that observation is the film thickness. Both WO_3 and $CuWO_4$ have a dense surface with many small nanoparticles for **Fe-2** to anchor to (Figure B.14 and Figure C.11). However, the $CuWO_4$ is much more thin than WO_3 (~0.5 vs. 1.8 μm as measured by scanning electron microscopy). Therefore, the **Fe-2** likely has less surface area within the film to anchor to thus resulting in a much lower surface coverage.

In addition to measuring the surface coverage for **Fe-2** on $CuWO_4$, Raman and X-ray spectroscopy (XPS) are used to further characterize the complex on the $CuWO_4$ surface. Raman spectroscopy is unable to detect the **Fe-2** ligand scaffold on the electrode surface do to the low surface coverage. However, XPS is able to see the presence of Fe on the surface (Figure C.12). The Fe 2p peaks at 709 and 722 closely align with the peaks observed with **Fe-2** on WO_3 and do not match those expected for either Fe_2O_3 or $FeCl_2$.[25] Therefore, it is concluded that **Fe-2** is in fact present on the $CuWO_4$ surface. Additionally, cyclic voltammetry in non-aqueous electrolytes and linear sweep voltammetry in pH 3 Na_2SO_4 (Figure C.6) both reveal the presence of the $Fe^{2+/3+}$ redox couple which aligns with the redox couple for **Fe-2** in solution.

Confident **Fe-2** is attached to the electrode surface, the photoelectrochemistry of the modified electrode is measured in pH 3 Na_2SO_4. The chopped light linear sweep trace depicted in Figure 4.3 demonstrates the increase in photocurrent to be reproducibly 102%. The photocurrent enhancement furthermore suggests that the catalyst is forming an active

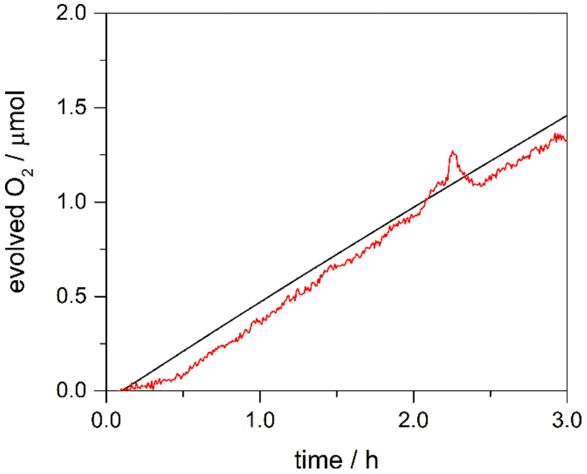

Figure 4.4 Faradaic efficiency of **Fe-2** on $CuWO_4$ towards water oxidation under AM 1.5G 100 mW cm^{-2} illumination at 1.23 V vs. RHE in pH 3 100 mM Na_2SO_4 using Pt CE and SCE RE

species on the electrode surface that is improving the rate of solar water oxidation.

To address our question about the selectivity of **Fe-2** on the surface, the Faradaic efficiency for water oxidation is measured during 3 hours of illumination (see Figure 4.4). The modified electrode exhibits 100% selectivity towards water oxidation. This result is not surprising considering that $CuWO_4$ is well known to oxidize water selectively in the presence of numerous electrolyte salts.[24] In addition to answering the prior question about the selectivity of **Fe-2** on an already selective material ensures that degradation of **Fe-2** is not contributing to the lower efficiency (79%) for **Fe-2** on WO_3. Instead, the loss of efficiency is only because of the photoelectrochemical contribution of WO_3. After electrolysis, XP spectra are obtained of the modified electrode. The catalyst cannot be observed by XPS after illumination for 3 hours (see Figure C.12). The likely explanation for this result is that the catalyst is falling off from the surface similar to when it is anchored to WO_3.

Synthetic Method	**Fe-2 modified $CuWO_4$ j_{ph} at 1.23 V ($\mu A \bullet cm^{-2}$)**	**% increase**
spray pyrolysis	36	103
sol-gel	100	35
oriented sol-gel	40	36
single crystal	125	66

Table 4.3 Synthetic methods compared to increase in photocurrent when $CuWO_4$ is modified with **Fe-2**

In addition to looking at the photoelectrochemical enhancement for **Fe-2** on $CuWO_4$ prepared by spray pyrolysis, the photoelectrochemical performance of **Fe-2** on $CuWO_4$ is also measured for electrodes prepared by two different sol-gel methods and on a single crystal of $CuWO_4$. The results of these experiments are summarized in Table 4.3, and the chopped light linear sweep curves are found in Figure C.13-Figure C.15. The $CuWO_4$ electrodes prepared by the different sol-gel methods both exhibited lower photocurrent enhancement than the spray pyrolyzed electrodes at 35%. The most likely explanation for this decrease in photoelectrochemical enhancement is that the sol-gel methods both produce preferred orientation of the $CuWO_4$ crystal lattice as evidenced by their corresponding X-ray diffraction patterns (XRD, Figure C.16 and Figure C.17). As a result, the sol-gel $CuWO_4$ electrodes are not as polycrystalline like the spray pyrolyzed electrodes (Figure C.18). To provide more evidence for this explanation, the $CuWO_4$ is being prepared by spray pyrolysis to have some preferred orientation using $Cu(OAc)_2$ in the precursor solution (as opposed to $CuCl_2$). These results will help provide further evidence for this claim or not.

For the modified single crystal of $CuWO_4$, there is also some preferred orientation associated with the material because it is a single crystal material, which most likely explains the decrease in photoelectrochemical enhancement for **Fe-2** anchored to the single crystal. An additional possibility is that the single crystal is also necessarily illuminated from the front (due to electrode construction, there is not back surface to illuminate). To ensure that this is not the reason for lower photocurrent enhancement, the spray pyrolyzed electrodes are front *and* back illuminated for the same electrode, and the change in photocurrent enhancement is approximately half for front illumination compared to back illumination with **Fe-2** on the electrode surface (Figure C.19). Therefore, it is likely that the lower photoelectrochemical enhancement from the single crystal is likely due to competitive light absorption from the complex on the surface and not from crystal orientation.

The results from screening different synthetic methods helps provide evidence towards the question about the impact of electrode construction on the photoelectrochemical enhancement when a semiconductor is modified with **Fe-2**. The best explanation of this evidence is that the synthetic method significantly impacts the photoelectrochemical enhancement observed when the molecular species is anchored to the electrode surface most likely due to the orientation of the crystal lattice on the conductive substrate.

The pH is also examined for how it impacts the photoelectrochemical enhancement when $CuWO_4$ in modified with **Fe-2**. Previously, we have shown that when **Fe-2** is anchored to WO_3, there is a large drop-off in rate of water oxidation above pH 5. However, because WO_3 exhibits poor stability up to pH 7, it is possible that the semiconductor is degrading and the catalyst is still capable of enhancing the rate. Therefore, it is of interest to reexamine this question using a semiconductor electrode that is stable through the acidic and neutral pH range. The results of this screen are summarized in Table 4.4 and Figure C.20.

From this experiment, it can be concluded that the photoelectrochemical enhancement observed for **Fe-2** on $CuWO_4$ is stable up to pH 7 in potassium phosphate (KP_i) and the optimal pH for **Fe-2** on $CuWO_4$ is below pH 4. The new electrolyte/buffer is used to prevent the pH from shifting as dramatically as it could in the un-buffered Na_2SO_4 electrolyte. This conclusion aligns closely with what has previously been reported for **Fe-1** in neutral electrolytes using $Ru(bipy)_3Cl_2$ and $Na_2S_2O_8$ as the sacrificial oxidants.[22]

pH	**j_{ph} at 1.23 V vs. RHE ($\mu A \bullet cm^{-2}$)**	**% increase**
1.62	16	60
2.03	16	136
3.01	25	161
4.03	34	72
4.96	23	56
6.02	28	94
6.97	18	77

Table 4.4 pH dependence of photocurrent enhancement with **Fe-2** on $CuWO_4$ prepared by spray pyrolysis

One question that arose from this series of experiments is how the electrolyte impacts the photoelectrochemical performance of **Fe-2** on $CuWO_4$. The main impetus for asking this question is that the stability of $CuWO_4$ is significantly better in potassium borate (KB_i) at pH 7 than KP_i.[24] However, we surmise that the stability is derived through strong

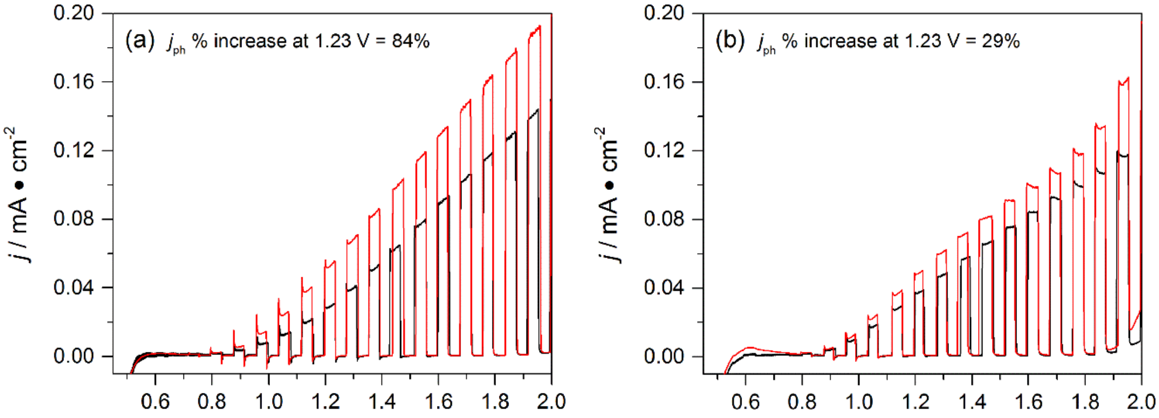

Figure 4.5 Chopped light linear sweep voltammogram of **Fe-2** on $CuWO_4$ (red) compared to bare $CuWO_4$ (black) in pH 7 100 mM KP_i (a) or 100 mM KB_i (b) under AM 1.5G 100 mW cm^{-2} illumination at 20 mV s^{-1} using Pt CE and SCE RE.

coordination of borate to the electrode surface, which facilitates the proton-coupled electron-transfer (PCET) reaction between $CuWO_4$ and the solution. Furthermore, KB_i has previously demonstrated an important role in facilitating water oxidation with electrocatalysts like CoB_i or NiB_i.[26,27] Due to this supposition, it is hypothesized that if KB_i is used in place of KP_i, then the photoelectrochemical enhancement observed with **Fe-2** on $CuWO_4$ will be less because the KB_i will also likely coordinate to the active species and prevent higher rates. Indeed, when the chopped light linear sweep experiment is performed in KB_i, the photoelectrochemical enhancement is significantly less than that observed in KP_i, as depicted in Figure 4.5.

Additionally, KB_i is poorly ionized at pH 7. Therefore, in attempt to make KB_i a better electrolyte, the pH is increased to 9.4. When the pH is increased to 9.4, the photocurrent enhancement is the same as that observed for bare $CuWO_4$ (Figure C.21). These experiments not only demonstrate that a non-coordinating electrolyte is important to photoelectrochemical enhancement for **Fe-2** on an electrode surface, but also that the molecular component is only stable up to pH 7. This result raises an additional question about how other non-coordinating weak acids (like nitrous, formic, or acetic acid) impact the photoelectrochemical enhancement when **Fe-2** is anchored to $CuWO_4$ in the pH range from 4-7.

Anchoring **Fe-2** on $CuWO_4$ allows us to begin answering many important questions about the optimal photoelectrochemical environment and the electrode synthesis' impact on the rate enhancement of solar water oxidation. Furthermore, these experiments help point out additional areas for developing future systems such as starting with the highest performing synthetic methods, optimizing the pH, and examining the influence of the electrolyte on catalytic performance.

4.4 Conclusions

This Chapter represents the initial findings of the impact the semiconductor has on activating the molecular catalyst **Fe-2**. The impact of synthetic conditions has been examined in depth for $CuWO_4$, and the results suggest that the synthetic method greatly impacts the amount of photocurrent enhancement that is observed. Since this work has demonstrated the ability to successfully modify single crystal substrates, examining the composition of exposed crystal faces and the impact the crystal face has on the binding and catalysis of the modified $CuWO_4$ would be very insightful for further probing the impact of synthetic method on photoelectrochemical performance. Furthermore, the impact of pH is examined for **Fe-2** on $CuWO_4$ and compared to the results obtained for **Fe-2** on WO_3. From these results, it can be concluded that the catalyst remains active up to pH 7 on the electrode surfaces, but maintains optimal reactivity at pH's below 4.

In addition to looking at the impact of electrode fabrication on activating **Fe-2** under illumination, various semiconductors are screened in place of WO_3 or $CuWO_4$ to vary the band structure of the semiconductor. From these experiments, it seems plausible that the band gap and conduction band energy play the largest role in activating the molecular catalyst. Wherein the band gap dictates the number of holes generated in the semiconductor (ideally to later oxidize the molecular catalyst) and the conduction band plays a role in preventing the catalyst from being activated (presumably through back electron transfer from the conduction band to the molecular catalyst). However, in order for these explanations to be more concrete, a more controlled synthetic method such as spray pyrolysis will be necessary to ensure morphologies and thicknesses are held constant. Additionally, the photocurrent density of the semiconductors should also be comparable across the different semiconductors for more comparability across the range of semiconductors. Ultimately, this screen does demonstrate the importance of selecting the right semiconductor to activate a desired molecular catalyst. Furthermore, when these results are compared to those obtained in Chapter 2 for the ruthenium catalysts, the observed rate enhancement is much higher for **Fe-2** than any of the **Ru** catalysts.

4.5 Experimental Methods

General Methods. All reactions were carried out under a nitrogen atmosphere unless otherwise noted. THF, CH_3CN, and CH_2Cl_2 were dried prior to use according to common practices. **Fe-2** was prepared as described in Chapter 3. All other materials were obtained from commercial sources, and used as purchased. Column chromatography was performed using standard 200 mesh silica gel. Elemental analyses were performed by Atlantic Microlab, Inc. for C, H, N, and Cl determinations. ^{1}HNMR and ^{13}CNMR spectra were recorded in $CDCl_3$ or CD_3CN using a Varian MR400 at 400 MHz. Electrospray ionization mass spectra were collected on a Micromass LCT TOF MS through a Waters 1525 GC. UV/Visible/NIR spectroscopy was performed on an Agilent CaryWin 5000.

Preparation of various semiconductors:

$CuWO_4$ – $CuWO_4$ was prepared via multiple synthetic methods.

Spray pyrolysis: Thin films of $CuWO_4$ were deposited onto fluorine doped tin oxide (FTO) coated glass substrates by spray pyrolysis using a custom built apparatus. Prior to deposition, 2.5 × 1 cm^2 FTO glass substrates were washed via sonication in three steps using acetone/ethanol/ DI water for 10 minutes each cycle. The substrates were then dried under a flow of N_2 after the final sonication in DI water. An aqueous precursor solution containing $CuCl_2$ and Ammonium metatungstate (AMT, $(NH_4)_6H_2W_{12}O_{40}\bullet xH_2O$) was sprayed through a custom glass nozzle onto the substrate. During deposition, the substrate was kept at a temperature of 275 °C, the nozzle distance from the top of the substrate was 10 inches, the carrier gas was N_2 (12.5 PSI) and the solution was sprayed 100 times. Each spray pulsed had a duration of 1s with a 5s delay between each pulse to ensure total evaporation of solvent between sprays. Additionally, as the solution was sprayed the nozzle oscillated from right to left to ensure even deposition. The concentraion of Cu^{2+} and W^{6+} in the precursor solution was kept at 10 mM (0.01M $CuCl_2$ and 0.000833M AMT). Finally, after spraying the precursor onto the substrate the electrodes were annealed at 550 °C for 1 hour in a muffle furnace to form crystalline $CuWO_4$.

Sol-gel: 1 mmol $Cu(NO_3)_2$ and 1 mmol ammonium meta tungstate (12 W/mol) were added to a 20 mL scintallation vial. The solids were dissolved in 1.34 g ethylene glycol. The resulting solution was light blue, and slightly cloudy. The cloudiness was removed through dropwise (5 drops) addition of H_2O to the vigorously stirring solution. The clear solution was heated for 3 hours at 92 °C After 3 hours of heating, a thick dark green solution formed. 25 µL of the hot solution were spread over 1 cm^2 FTO substrate and spun at 1200 RPM for 10 minutes followed by 5 seconds at 2000 RPM. The resulting transparent films were stable at room temperature in air for ~20 minutes. After spinning three films (~30 minutes), the green sol no longer produced high performing $CuWO_4$ (~100 µA cm^{-2}) electrodes as the $CuWO_4$ begins to precipitate.[24]

Oriented Sol-gel : Prepared by James J. Brancho and Christopher R. Dihn. In a 50 mL Erlenmeyer flask, 1.838 g W powder (99.9%, Aldrich) was allowed to react with 35 mL of 30% H_2O_2 solution (Aldrich) overnight, resulting in a clear, colorless solution with no observable unreacted metal or precipitate. The reaction was then cooled to 0 °C and ~2 mg Pt black was added in two aliquots to keep the decomposition of H_2O_2 from proceeding violently. Once bubbling had ceased (~6 hr), the mixture was vacuum filtered through a 0.45 µm membrane filter, yielding the peroxytungstic acid (PTA) solution as a filtrate. A 3 mL aliquot of PTA solution was transferred to a vial and 3 mL of isopropanol was added for a final [W^{6+}] of 0.143 M. The solution was stable under refrigeration at 4 °C for several weeks. To prepare $CuWO_4$ sol-gel electrodes, 1 mL of PTA/isopropanol (0.143 mmol W^{6+}) was added to a 4 mL scintillation vial with 0.274 g (1.43 mmol) citric acid and sonicated until the citric acid was dissolved. 0.0345 g $Cu(NO_3)_2$ 3 H_2O was added and the solution was again sonicated until homogeneous. A clear, light blue solution resulted. This solution was spin-coated onto clean FTO slides by applying 15 uL of solution to the FTO, spinning for 45 s at 1000 rpm, drying at 160 °C for 5 minutes, and repeating until 12 layers had been applied. Films were then placed into a pre-heated oven at 550 °C in air and annealed for 6 h.

Single crystal: Received from Joseph E. Yourey through molten salt synthesis.

TiO_2 – Modified procedure developed by the Mallouk group.[28] Put 250ml H_2O and 80mL acetic acid in a 500 mL round bottom. Chilled this solution to -5 °C. Prepared separately a solution of 7.896 g IPA and 35.52 g Ti(isopropoxide)$_4$. Added this solution drop wise at approximately 1 drop/sec under rapid stirring until the solution was completely added. Once added, the solution was heated to 80 °C and continued rapid stirring. During heating, the solution rapidly solidified into a gel and needed to be manually stirred to break up the gel. This insulation helped for uniform heating and really was necessary for this step. Once above 70 °C and near 80 °C it broke into a cloudy solution and stirred easily again. Refluxed at 80 °C for 8 hours.

Sonicated the resulting solution and transferred 12 mL into a PTFE reactor for hydrothermal treatment at 5 °C/min ramp up, heated at 250 °C for 12hrs, then cooled at 10 °C/min ramp down. The remaining solution can be covered and stored until needed later (indefinitely), however it must be sonicated prior to use. Removed bomb once cool and removed reactor. Pipetted off supernatant. Sonicated the reactor to release gaseous products for 5 minutes. Rotovaped the remaining solution to half the initial volume. Stirred this solution vigorously and added ~0.36 g of hydroxypropylcellulose very slowly. Continued stirring for 24 hours while covered. The resulting paste was thicker but still stirred well.

This paste was then doctor bladed onto clean FTO substrate using electrical tape as the guide for thickness, dried in air for 30 minutes, and then annealed at 500 °C for 1 hour with 1 hour heating and cooling. This resulted in reproducible anatase electrodes

$BiVO_4$ – Dropcast a yellow 200 mM $Bi(NO_3)_2$ and 200 mM $(NH_4)_2VO_4$ solution in 2M HNO_3. The solution was allowed to dry overnight in air, and was then annealed at 400 °C for 6 hours with 2 hour heating and cooling. These produced thick, yellow films of $BiVO_4$.

Fe_2O_3 – Electrodes of Fe_2O_3 were prepared according to Choi and co-workers through electrodeposition of iron hydroxide on FTO and then annealed to form hematite Fe_2O_3 at 500 °C for 8 hours heated and cooled at 2 °C/minute.[29]

$SnWO_4$ – Electrodes of $SnWO_4$ were prepared according to Pyper et al. through hydrothermal treatment of WO_3-hydrate in $Sn(NO_3)_2$ solutions.[30] WO_3 was prepared by a known procedure.[31] Sodium tungstate dihydrate, $Na_2WO_4 \cdot 2H_2O$, (0.308 g, 9.34×10^2 mmol) was dissolved in 40 mL deionized water. 3 mol/L HCl (13.34 mL, 4×10^4 mmol) was added dropwise to the stirring solution, which formed a yellow precipitate. Next, ammonium oxalate, $(NH_4)_2C_2O_4$, (0.267 g, 2.15×10^3 mmol) was added and the solution became clear and colorless. An additional 40 mL of deionized water was added, and the solution was stirred for 30 minutes. Then, 11.5 mL aliquots of solution were transferred to 23 mL PTFE liners (Parr Instrument Company). The FTO films were masked off with PTFE tape to a surface area of 1 cm^2 so that deposition onto the FTO area was controlled. The films were placed face down in the liner and sealed in a stainless steel autoclave. The vessels were held at 120 °C for 12 hours with a 10 °C/min ramp rate. These films were either kept as is ($WO_3 \cdot H_2O$, yellow/green in appearance) or annealed in air at 450 °C for 1 hour (monoclinic WO_3, green/white in appearance). A 0.5 mol/L $SnCl_2$ solution was made that had an initial pH of ~1. Next the $WO_3 \cdot H_2O$ or WO_3 films were placed face down in the hydrothermal vessel filled with 14 mL of 0.5 mol/L $SnCl_2$ solution whose pH was 1 or adjusted to 4 or 7 with 7 mol/L NaOH and 3 mol/L HCl. The vessels were sealed in steal autoclaves and heated for 24 hours at 180 °C with a 10 °C/min ramp rate. The films were rinsed with 3 mol/L HCl to remove any tin chloride hydroxide crystals that formed during the hydrothermal reaction

Modification of semiconductors with Fe-2: Semiconductor electrodes were heated to 60 ^oC in ~500 μM **Fe-2**/acetonitrile solution and sealed in a vial. The anodes were soaked for 8 hours in the dark and then rinsed with excess acetonitrile and dried with N_2. This procedure resulted in a light yellow tint to the modified electrodes.

Electrochemistry. All electrochemistry was performed on either a CH Instruments CHI-600 or CHI-1000 potentiostat. All potentials are referenced to SCE (saturated calomel electrode) with saturated KCl electrolyte reference electrode (RE), and Pt was used as the counter electrode (CE) in all experiments. Non-aqueous solvents were dried prior to use and $TBAPF_6$ was recrystallized from EtOH prior to use. Glassy carbon (GC) was used as the working electrode (WE) for solution-based electrochemistry. Aqueous solutions were prepared using 18.2 **Ω** Milli-pore H_2O and concentrated sulfuric acid, and then pH adjusted with 7 M NaOH to obtain the desired concentration and pH. The aqueous solutions were also purged with N_2 prior to use, but were not sealed under N_2. All photoelectrochemical measurements were carried out in custom-built cells with quartz viewing windows. All illumination was carried out using a Newport Oriel 150 W Xe lamp fitted with an AM1.5G filter from Newport whose power was adjusted to 100 mW/cm^2.

References

1 Klepser, B. M.; Bartlett, B. M. *J. Am. Chem. Soc.* **2014**, *136*, 1694.

2 Chen, X.; Ren, X.; Liu, Z.; Zhuang, L.; Lu, J. *Electrochem. Commun.* **2013**, *27*, 148.

3 Zhong, D. K.; Zhao, S.; Polyansky, D. E.; Fujita, E. *J. Catal.* **2013**, *307*, 140.

4 Katz, M. J.; Riha, S. C.; Jeong, N. C.; Martinson, A. B. F.; Farha, O. K.; Hupp, J. T. *Coord. Chem. Rev.* **2012**, *256*, 2521.

5 Patil, P. S.; Patil, P. R. *Bull. Mater. Sci.* **1996**, *19*, 651.

6 van de Krol, R. Principles of Photoelectrochemical Cells. In *Photoelectrochemical Hydrogen Evolution*; Grätzel, M. and van de Krol, R., Eds.; Springer: New York, 2012; pp. 13-68.

7 Jia, Q.; Iwashina, K.; Kudo, A. *Pro. Nat. Acad. Sci.* **2012**, *109*, 11564.

8 Chen, Q.; Li, J.; Zhou, B.; Long, M.; Chen, H.; Liu, Y.; Cai, W.; Shangguan, W. *Electrochem. Commun.* **2012**, *20*, 153.

9 Kumari, N.; Krupanidhi, S B.; Varma, K. B. R. *Mater. Res. Bull.* **2010**, *45*, 464.

10 Ghrairi, N.; Bouaicha, M. *Nanoscale Res. Lett.* **2012**, *7*, 357.

11 Fillol, J. L.; Codolá Z.; Garcia-Bosch, I.; Gómez, L.; Pla, J. J.; Costas, M. *Nat. Chem.* **2011**, *3*, 807.

12 Bignozzi, C. A.; Caramori, S.; Cristino, V.; Argazzi, R.; Meda, L.; Tacca, A. *Chem. Soc. Rev.* **2013**, *42*, 2228.

13 Yourey, J. E.; Bartlett, B. M. *J. Mater. Chem.* **2011**, *21*, 7651.

14 May, R. A.; Kondrachova, L.; Hahn, B. P.; Stevenson, K. J. *J. Phys. Chem. C* **2007**, *111*, 18251.

15 Glasscock, J. A.; Barnes, P. R. F.; Plumb, I. C.; Bendavid, A.; Martin, P. J. *Thin Sol. Films* **2008**, *516*, 1716.

16 Sartoretti, C. J.; Alexander, B. D>; Solarska, R.; Rutkowska, I. A.; Augustynski, J *J. Phys. Chem. B* **2005**, *109*, 13685.

17 TiO_2 $\varepsilon = 5.62$ - Wemple, S. H. *J. Chem. Phys.* **1977**, *67*, 2151.

18 WO_3 $\varepsilon = 50$ - Knox, A. B. *Trans. Br. Ceram. Soc.* **1967**, *66*, 85.

19 $CuWO_4$ $\varepsilon = 83$ - Arora, S. K.; Mathew, T. *Phys. Stat. Sol. A* **1989**, *116*, 405.

20 Fe_2O_3 $\varepsilon = 12$ - *Handbook of Chemistry and Physics* 74th ed.; Lide, D. R. ed.; CRC: Boaca Raton, FL, 1994.

21 $BiVO_4$ $\varepsilon = 32$ - Sarkar, S.; Chattopadhyay, K. K. *Physica E* **2012**, *44*, 1742.

22 Chen, G.; Chen, L.; Ng, S-M.; Man, W-L.; Lau, T-C. *Angew. Chem. Int. Ed.* **2013**, *52*, 789

23 Bae, E.; Choi, W.; Park, J.; Shin, H. S.; Kim, S. B.; Lee, J. S. *J. Phys. Chem. B* **2004**, *108*, 14093.

24 Yourey, J. E.; Pyper, K. J.; Kurtz, J. B.; Bartlett, B. M. *J. Phys. Chem. C.* **2013**, *117*, 8708.

25 Biesinger, M. C.; Payne, B. P.; Grosvenor, A. P.;n Lau, L. W. M.; Gerson, A. R.; Smart, R. St. C. *Appl. Surf. Sci.* **2011**, *257*, 2717.

26 Esswein, A. J.; Surendranath, Y.; Reece, S. Y.; Nocera, D. G. *Energy Envrion. Sci.* **2011**, *4*, 499.

27 Dinca, M.; Surendranath, Y.; Nocera, D. G. *Pro. Nat. Acad. Sci.* **2010**, *107*, 10337.

28 Youngblood, W. J.; Lee, S-H. A.; Kobayashi, Y.; Hernandez-Pagan, E. A.; Hoertz, P. G.; Moore, T. A.; Moore, A. L.; Gust, D.; Mallouk, T. E. *J. Am. Chem. Soc.* **2009**, *131*, 926.

29 Spray, R. L.; Choi, K-S. *Chem. Mater*. **2009**, *21*, 3701.

30 Pyper, K. J.; Evans, T. C.; Bartlett, B. M. *Chin. Chem. Lett.* **2015**, *in press* doi:10.1016/j.cclet.2015.01.027

31 Yang, J.; Li, W. Z.; Li, J.; Sun, D. B.; Chen, Q. Y. *J. Mater. Chem.* **2012**, *22*, 17744-17752.

Chapter 5

Solar Water Oxidation with Inactive Molecular Complexes on WO_3

5.1 Introduction

During the last five years, the field of molecular WOCs has experienced substantial growth. Spurred by the reports of Ellis et al.[1] and Fillol et al.[2], many new first-row transition metal catalysts have been reported.[3,4,5,6,7] In particular, the report by Mayer and co-workers encouraged us to pursue other first-row transition metal catalysts because of the significant rate enhancement achieved for copper relative to iron.[8] Following the report of an anionic copper polypeptide catalyst by Meyer et al., a trend in catalyst design for the first-row transition metals seemed to emerge.[9] The trend appeared to require multidentate, soft, nitrogen containing ligands. The ligands prepared in Chapter 3 matched these perceived requirements well. As a result of these reports, we thought we might be able to make new homogeneous WOCs using the modified ligand from Chapter 3.

If the new complexes exhibited no homogeneous reactivity, the “inactive” complexes may be limited catalytically by high oxidative potentials required to reach reactive species’ oxidation states. More simply, chemical oxidants such as $Ce(NH_4)_2(NO_3)_6$ (CAN E° = 1.72 V vs. NHE) or $Na_2S_2O_8$ (E° = 2.10 V vs. NHE) are incapable of providing enough energy to access the catalytically active species for water oxidation. Metal electrodes are often thermodynamically unable to activate the complex since dark water oxidation competes at large overpotentials. At best case, a complex that could theoretically oxidize water at 2.20 V vs. NHE would be unable to homogeneously catalyze water oxidation because no oxidant or electrode (maybe an Hg droplet) could provide enough energy to activate the complex. In contrast, the valence band holes in oxide semiconductors are positioned at ~3 V vs. RHE, which possesses a large excess of potential energy relative to water oxidation. For instance, a hole generated by WO_3 in the valence band has a potential energy of ~3.1 V vs. NHE. This hole could then in theory oxidize an inactive complex rapidly that could not be oxidized via another form of oxidant. Therefore, it is hypothesized that if a complex is inactive, semiconductors could be capable of oxidizing the "inactive" complexes due to the excess of oxidative potential energy. This general idea is summarized in Figure 5.1.

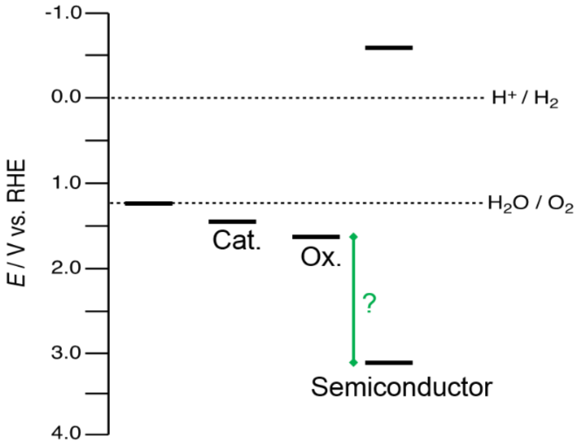

Figure 5.1 Energy diagram of a semiconductor's additional oxidative energy relative to molecular catalysts and other oxidants

5.2 Characterization of M Complexes

With this approach in mind, the other first-row transition metal complexes (Mn-Zn) are prepared for **M-1**, **M-2** as illustrated in Scheme 5.1. Similar to the method employed for **Fe** complexes, the metalation reaction is rapid and is associated with a drastic

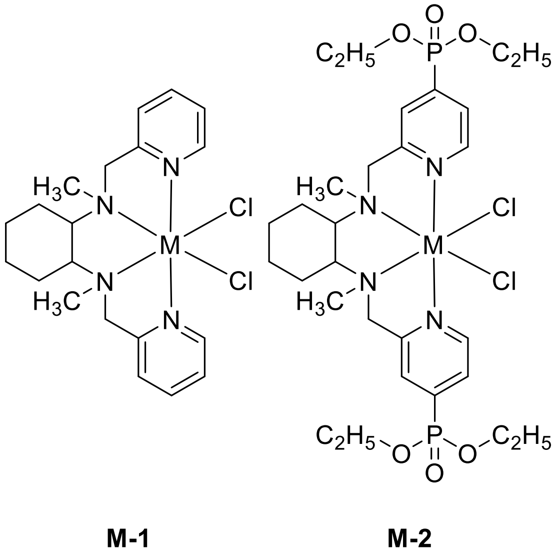

Scheme 5.1 Metal complexes targeted for homogeneous water oxidation and for anchoring to WO_3

color change with the exception of **Mn** and **Zn**. Upon formation, ^{1}H-NMR spectra are collected for the complexes. Although many of the complexes remain paramagnetic, the **Zn** complexes are diamagnetic, and show peak broadening and upfield shifts. These results are consistent with the ligand being coordinated to an electropositive metal-center. To further corroborate the identity of **M-1** and **M-2** complexes, ESI-MS$^+$ analysis is also employed. The mass spectrometry data demonstrates the presence of the desired complex ions, with little to no free ligand.

In order to probe the reactivity of the complexes, **M-1** is used for the standard comparison. **M-1** is selected for the homogeneous reaction in the presence of because **Fe-1** exhibits the highest reactivity with $Ce(NH_4)_2(NO_3)_6$ (CAN) in solution for the **Fe** catalysts. As illustrated in Figure 5.2, none of the other complexes exhibit any reactivity towards water oxidation in the presence of CAN. This result is unsurprising since few first-row transition metal catalysts have been discovered. Furthermore, the new complexes that have been reported for homogeneous water oxidation typically only operate at pH > 8.[3-9]

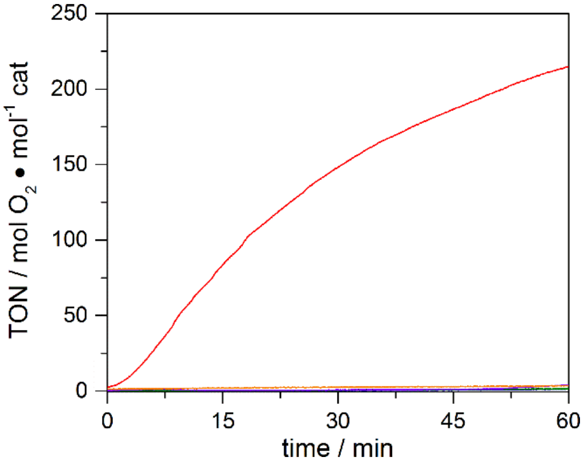

Figure 5.2 Homogeneous water oxidation with **M-1** in the presence of $Ce(NH_4)_2(NO_3)_6$ for Mn (black), Fe (red), Co (blue), Ni (green), Cu (purple), Zn (orange)

More realistically, many of the other first-row transitional metal catalysts for water oxidation operate electrochemically and/or at much higher pH. For example, both of the recently reported copper water oxidation catalysts operate under strictly basic conditions and as a result strictly electrochemically. Therefore, it is more likely that the complexes would exhibit some electrocatalytic activity, as opposed to homogeneous reactivity in the presence of CAN. Looking at the cyclic voltammetry (CV; see Figure C.1) of **M-2** in 100 mM Na_2SO_4 at pH 3 it is apparent that all complexes exhibit electrocatalysis at overpotentials greater than **Fe-2**.

Complex	E_{cat} (V vs. RHE)
Mn-2	1.70V
Fe-2	1.35 V
Co-2	1.81 V
Ni-2	1.68 V
Cu-2	1.64 V
Zn-2	1.62 V

Table 5.1 Electrochemical redox potentials for **M-2**

5.3 Photoelectrochemistry of M-2 on WO_3

With the results of the homogeneous screen in mind, we hypothesized that if the complexes are anchored to WO_3, then they may exhibit an improvement in photoelectrochemical performance of WO_3 similar to **Fe-2** on WO_3. The complexes are anchored to WO_3 through soaking the electrodes in acetonitrile solutions of **M-2** at 60 °C for at least 8 hours. When the modified electrodes are removed from the soaking solution, they are rinsed extensively. Despite rinsing the electrodes, the open circuit voltage for all of the electrodes shifts to more positive potentials significantly. This suggests that the complexes are anchored to the electrode surface.

Complex	j_{ph} % increase	F.E.(O_2) (%)
Bare WO_3	-	56
Mn-2	62	23
Fe-2	60	79
Co-2	35	75
Ni-2	46	97
Cu-2	71	99
Zn-2	82	83

Table 5.2 Photoelectrochemical performance of **M-2** on WO_3 in 100 mM Na_2SO_4 pH 3 under AM 1.5G 100 mW cm^{-2} illumination at 20 mV s^{-1} using Pt CE and SCE RE

The results of the screen are summarized in Table 5.2, and linear sweep voltammograms can be found in Figure D.2. From these experiments, there are three complexes (**Ni-Zn**) that exhibit significantly higher rates of oxygen evolution and higher selectivities. To ensure that these complexes exhibit higher reactivity because of the entire complex, WO_3 is soaked with $NiCl_2$, $CuCl_2$, and $ZnCl_2$. When WO_3 is soaked with the metal chloride salts, minimal improvement in the photocurrent is observed as depicted in Figure D.3. These experiments support the conclusion that the **M-2** complexes with Ni, Cu, and Zn are necessary for increasing the rate of oxygen evolution.

In addition to exhibiting higher rates of oxygen evolution compared to WO_3, the inactive complexes also exhibit higher rates of oxygen evolution compared to **Fe-2** on WO_3. This result implies that there may be many other complexes that have been previously studied for water oxidation, which can now be activated using a semiconductor like WO_3. However, based on these experiments, it is not possible to derive further design principles for preparing other complexes capable of being activated by semiconductor electrodes.

The **Zn-2** case is of particular interest because this result suggests that redox activity is not necessarily required for the molecular complex. There are two possible explanations for **Zn-2**'s reactivity. First, the oxidative potential energy from WO_3 is sufficient to oxidize/activate the Zn^{2+} complex. Second, the molecular complex acts as a reaction site (similar to ZnO) and form $Zn\text{-}(OH)_2$ or Zn=O species that can be subsequently attacked by water. Electrons that should normally be transferred from water to the molecular species are instead transferred directly to the semiconductor valence band. Because $ZnCl_2$ is incapable of improving the photoelectrochemical performance of WO_3 on its own, the electron transfer process is most likely facilitated by the ligand that also stabilizes the $Zn\text{-}(OH)_2$ species and prevents decomposition directly to ZnO on the WO_3 surface. To distinguish between these possibilities, another redox inactive complex should be prepared to comparew with **Zn-2**. If a redox inactive complex is capable of increasing the rate of oxygen evolution under illumination, then the second explanation is most likely.

Complex	Observed M 2p (eV)	M-Cl_2 2p B.E. (eV)	M-O 2p B.E. (eV)
Ni-2	855.4, 872.9	856-858, 876-874	853-854, 864-866
Cu-2	932.0, 952.0	934-936, 954-956	932.6-934, 943-944
Zn-2	1021.4, 1044.5	1022-1023, 1045-1046	1021, 1044.1-1044.7

Table 5.3 XPS observed binding energies of **M-2** M 2p peaks on WO_3 for **Ni-2**, **Cu-2**, and **Zn-2**

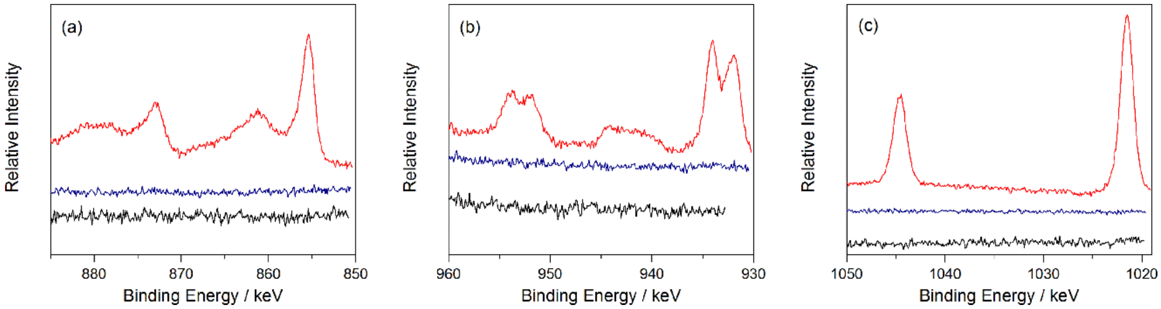

Figure 5.3 XP spectra of **Ni-2** (a), **Cu-2** (b), and **Zn-2** (c) on WO$_3$ before (red) and after photoelectrochemistry (blue) compared to bare WO$_3$ (black)

Similar to **Fe-2** on WO$_3$, we also want to test the stability of the complexes on the electrode surface. The complexes are unable to be seen using Raman spectroscopy or UV-Vis, so in addition to electrochemistry, X-ray spectroscopy (XPS) is used to probe for the presence of the different metals on WO$_3$. XPS of the modified electrodes before photoelectrochemistry points to the identity of the species present on the surface. Comparing the metal 2p peaks for Ni, Cu, and Zn to known values of the corresponding metal chlorides and oxides suggests that the species on the surface is not forming a metal chloride or oxide on the surface (Table 5.3).[10,11,12,13,14] Additionally, after photoelectrochemistry for 3 hours reveals that the complexes are present on the surface prior to photoelectrochemistry but have fallen into solution after 3 hours of illumination as illustrated in Figure 5.3.

These experiments lead us no closer to understanding the active species during catalysis. However, the most likely explanation for these complexes is similar to the case of **Fe-2** on WO$_3$. To probe this further, ESI-MS$^+$ of the electrolyte after 3 hours of electrolysis and repeating the experiment with the same electrode in fresh electrolyte will be used to probe for complex degradation in solution and to ensure that the catalytically active species that forms is still attached to the WO$_3$ surface. These experiments will lead us closer to understanding whether photoelectrochemistry is happening in solution or on the surface.

5.4 Conclusions

The discovery made in this chapter provides the opportunity for many new complexes to be explored for photoelectrochemical applications in the future. Furthermore, it suggests that the semiconductor is contributing a hole to the oxidative process.

Additionally, activation of the molecular species through electron transfer into the semiconductor conduction band from an excited state electron on the molecular catalyst is most likely not the case. An implication from this work is that semiconducting metal oxides should be capable of activating complexes towards more energetically demanding reactions.

5.5 Experimental Methods

General Methods

All reactions were carried out in air unless otherwise noted. THF, CH_3CN, and CH_2Cl_2 were dried prior to use according to common practices. All other materials were obtained from commercial sources, and used as purchased. Ligand **4** was obtained according to the synthesis described in Chapter 3. Column chromatography was performed using standard 200 mesh silica gel. Elemental analyses were performed by Atlantic Microlab, Inc. for C, H, and N determinations. NMR spectra were recorded in $CDCl_3$, CD_3CN, or CD_3OD using a Varian MR400 at 400 MHz. Electrospray ionization mass spectra were collected on a Micromass LCT TOF MS through a Waters 1525 GC. UV/Visible/NIR spectroscopy was performed on an Agilent CaryWin 5000.

Synthesis

General procedure for M(2)Cl_2:

One equivalent of ligand **2** and metal dichloride salt were dissolved in 3 mL CH_3CN. The solution was stirred at room temperature overnight, and concentrated *in vacuo*.

Manganese (tetraethyl N,N'-bis(methylpyrid-2-yl-4-phosphonate)-N,N'-dimethyl-1,2-diaminocyclohexane) dichloride (Mn(2)Cl_2, Mn-2)

Reaction with $MnCl_2 \times 4H_2O$ precursor produced an orange powder (8.9 mg, 83% yield). ^{1}HNMR(CD_3CN, ppm): 10.70, 9.87, 9.39, 6.43, 5.59, 4.09, 3.62, 3.11; ESI-MS$^+$: [Mn(**2**)(formate)]$^+$ = 696.0, [Mn(**2**)OH]$^+$ = 668.0

Cobalt (tetraethyl N,N'-bis(methylpyrid-2-yl-4-phosphonate)-N,N'-dimethyl-1,2-diaminocyclohexane) dichloride (Co(2)Cl_2, Co-2)

Reaction with $CoCl_2 \times 6H_2O$ precursor produced a green powder (15.2 mg, 82% yield). ^{1}HNMR(CD_3CN, ppm): 91.65, 72.95, 45.79, 26.70, 25.91, 23.52, 14.53, 10.21, 9.81, 9.49, 9.28, 8.92, 7.97, 7.76, 7.54, 4.43, 4.13, 2.19, 1.95, 1.31, 0.90, 0.31, -0.29, -1.48, -15.78; ESI-MS$^+$: [Co(**2**)(formate)]$^+$ = 700.0; [Co(**2**)Cl]$^+$ = 690.0

Nickel (tetraethyl N,N'-bis(methylpyrid-2-yl-4-phosphonate)-N,N'-dimethyl-1,2-diaminocyclohexane) dichloride (Ni(2)Cl$_2$, Ni-2)

Reaction with NiCl$_2$×4H$_2$O precursor produced a green-yellow powder (17 mg, 72% yield). ^{1}HNMR(CD$_3$CN, ppm): 51.41, 43.77, 24.68, 13.01, 12.97, 12.85, 9.66, 9.47, 8.66, 8.37, 7.25, 6.74, 6.62, 6.17, 3.09, -0.22; ESI-MS$^+$: [Ni(**2**)(formate)]$^+$ = 699.0, [Ni(**2**)Cl]$^+$ = 689.0

Copper (tetraethyl N,N'-bis(methylpyrid-2-yl-4-phosphonate)-N,N'-dimethyl-1,2-diaminocyclohexane) dichloride (Cu(2)Cl$_2$, Cu-2)

Reaction with anhydrous CuCl$_2$ precursor produced a brown powder (74 mg, 76% yield). ^{1}HNMR(CD$_3$CN, ppm): 7.89, 7.73, 7.56, 7.47, 4.64, 4.32, 4.23, 4.10, 3.89, 3.76, 3.27, 3.10, 2.11, 1.95, 1.78, 1.41, 1.35, 1.26, 1.13, 0.86, 0.57, -1.86, -6.57; ESI-MS$^+$: [Cu(**2**)(formate)]$^+$ = 704.4; [Cu(**2**)Cl]$^+$ = 694.3

Zinc (tetraethyl N,N'-bis(methylpyrid-2-yl-4-phosphonate)-N,N'-dimethyl-1,2-diaminocyclohexane) dichloride (Zn(2)Cl$_2$, Zn-2)

Reaction with ZnCl$_2$×4H$_2$O precursor produced a white precipitate (17 mg, 81% yield). ^{1}HNMR(CD$_3$CN, ppm): 11.82, 11.38, 10.81, 10.57, 7.01, 5.85, 5.30, 5.02, 4.31, 4.03, 2.44; ESI-MS$^+$: [Zn(**2**)(formate)]$^+$ = 705.0, [Zn(**2**)Cl]$^+$ = 695.0

General procedure for M(4)Cl$_2$:

One equivalent of ligand **4** and metal dichloride salt were dissolved in 3 mL MeOH. The solution was stirred at room temperature overnight, and concentrated *in vacuo*.

Manganese (N-(methylpyrid-2-yl)-N'-(methylpyrid-2-yl-4-phosphonic acid)-N,N'-dimethyl-1,2-diaminocyclohexane) dichloride (Mn(4)Cl$_2$, Mn-4)

Reaction with MnCl$_2$×4H$_2$O precursor produced an orange powder (29 mg, 72% yield). ^{1}HNMR(CD$_3$OD, ppm): 12.01, 11.42, 10.87, 7.75, 7.00, 6.60, 5.49, 4.94, 4.35; ESI-MS$^+$: [Mn(ppmcn)(formate)]$^+$ = 504.1, [Mn(ppmcn)MeOH]$^+$ = 490.1, [Mn(ppmcn)]$^+$ = 458.1

Cobalt (N-(methylpyrid-2-yl)-N'-(methylpyrid-2-yl-4-phosphonic acid)-N,N'-dimethyl-1,2-diaminocyclohexane) dichloride (Co(4)Cl$_2$, Co-4)

Reaction with $CoCl_2 \times 6H_2O$ precursor produced a green powder (52 mg, 78% yield). ^{1}HNMR(CD_3OD, ppm): 25.09, 12.14, 10.13, 9.38, 8.72, 8.38, 5.60, 4.03; ESI-MS$^+$: [Co(ppmcn)(formate)]$^+$ = 508.1, [Co(ppmcn)]$^+$ = 462.1

Nickel (N-(methylpyrid-2-yl)-N'-(methylpyrid-2-yl-4-phosphonic acid)-N,N'-dimethyl-1,2-diaminocyclohexane) dichloride (Ni(4)Cl_2, Ni-4)

Reaction with $NiCl_2 \times 4H_2O$ precursor produced a green-yellow powder (53 mg, 79% yield). ^{1}HNMR(CD_3OD, ppm): 47.72, 45.74, 38.85, 37.17, 19.57, 18.52, 16.73, 9.65, 8.97, 5.85, 4.22, 1.95, -1.88, -4.35; ESI-MS$^+$: [Ni(ppmcn)(formate)]$^+$ = 507.1, [Ni(ppmcn)]$^+$ = 461.1

Copper (N-(methylpyrid-2-yl)-N'-(methylpyrid-2-yl-4-phosphonic acid)-N,N'-dimethyl-1,2-diaminocyclohexane) dichloride (Cu(4)Cl_2, Cu-4)

Reaction with anhydrous $CuCl_2$ precursor produced a brown powder (53 mg, 75% yield). ^{1}HNMR(CD_3OD, ppm): 11.54, 9.53, 4.72, 3.28, 2.69, 1.19, 0.33, -1.07; ESI-MS$^+$: [Cu(ppmcn)(formate)$_4$(H_2O)]$^{2+}$ = 331.1

Zinc (N-(methylpyrid-2-yl)-N'-(methylpyrid-2-yl-4-phosphonic acid)-N,N'-dimethyl-1,2-diaminocyclohexane) dichloride (Zn(4)Cl_2, Zn-4)

Reaction with $ZnCl_2 \times 4H_2O$ precursor produced a white precipitate (35 mg, 86% yield). ^{1}HNMR(CD_3OD, ppm): 8.91 (b, 1H), 8.71 (b, 1H), 8.38 (b, 1H), 8.10 (b, 1H), 7.88 (b, 1H), 4.64 (d, 2H), 2.91 (b, 2H), 2.46 (b, 2H), 2.26 (b, 1H), 1.85 (b, 2H), 1.51 (b, 2H); ESI-MS$^+$: [Zn(ppmcn)(formate)Cl]$^+$ = 549.0, [Zn(ppmcn)Cl]$^+$ = 503.1, [Zn(ppmcn)]$^+$ = 467.1

WO_3 Preparation

WO_3 was prepared via a modified route that has been previously reported.[15] A Type 1 Dow-X cation exchange resin was activated by washing with 1 column volume of 3 M HCl. The column was then washed with Milli-pore H_2O until the pH was nearly neutral (~4 column volumes). A freshly prepared solution of $NaWO_4 \times 2H_2O$ (3.29 g) in 20 mL H_2O was added carefully to the exchange column. Initially, the eluent was collected into a waste beaker, however, the tungstic acid (eluent turned green) was collected into a stirring round bottom flask containing 25 mL EtOH. Once the tungstic acid finished eluting from the column, the waste beaker was replaced. The column was continually washed with water until the tungstic acid finished eluting and was further washed with 4 column volumes of H_2O. The column can be reused indefinitely following this procedure. After concentrating the tungstic acid to 20 mL *in vacuo*, 6.6 g of polyethylene glycol (300 MW PEG) is added to the colloid. The resulting colloid can be used to prepare films up to three days.

FTO was cleaned by sonication in acetone, EtOH, and water (15 minutes each), and dried under a stream N_2 gas. The clean FTO was masked with electrical tape to yield a 1 cm^2 area. 25 μL tungstic acid colloid was spread over the masked electrode area, and the electrode was spun at 2500 rpm for 30 seconds. After each layer, the films were annealed for 30 minutes at 500 °C. Once the films were cooled to room temperature, the process of spin coating was repeated until 10 layers were achieved. This produces electrodes that reproducibly obtain ~0.8 mA • cm^{-2} with an average thickness of ~1.8 μm.[16]

Electrochemistry

CH Instruments CHI-660 or CHI-1000 potentiostats were used to carry out all presented electrochemistry. Three electrode cells were used in all instances. For solution-based experiments, glassy carbon (GC) was used as the working electrode (WE), and Pt disk or wire were used as the auxilary electrode (AE). The measured potentials were referenced to SCE (saturated calomel electrode) with saturated KCl electrolyte as the reference electrode (RE). Acetonitrile was dried prior to use in electrochemical experiments, and $TBAPF_6$ was recrystallized from hot ethanol. Under aqueous conditions, pH 3 100 mM Na_2SO_4 was prepared using 18.2 Ω Milli-pore H_2O and concentrated sulfuric acid. The pH was then adjusted with 1 M NaOH. The aqueous solutions were purged with N_2 prior to use, but were not sealed under N_2. All photoelectrochemical measurements were performed in custom cells with quartz illumination windows. The electrodes were illuminated by a Newport Oriel 150 W Xe lamp fitted with an AM1.5G filter from Newport adjusted to 100 mW/cm^2 through a fiber optic bundle.

Oxygen Detection

Oxygen was quantified using a FOSPOR probe (from NeoFox) using two-point calibration at 20.90% and 0.00% O_2. A custom two-sided cell with quartz windows was utilizing to perform photoelectrochemical O_2 evolution experiments. The O_2 probe, working electrode, and SCE RE were on one side, and the temperature probe and the Pt

AE were on the other side. The solutions were purged at least 15 minutes with N_2, and then sealed under N_2 on a Schlenk line. Standard reaction conditions: illumination at 100 mW/cm^2 filtered with AM 1.5G while the potential was held at 809 mV *vs.* SCE in pH 3 100 mM Na_2SO_4 (1.23 V *vs*. NHE). The stable baseline was collected for ~30 minutes, and the photoanode was illuminated for ~3 hours. Following illumination, the O_2 was allowed to reach stabilize for ~30 minutes to allow for temperature fluctuations with the probe. Using Faraday's Law, the Faradaic efficiency could be calculated by dividing the measured moles of O_2 by the theoretical yield. The theoretical yield was determined by dividing the total charge passed during the experiment by $4F$ (4-electron oxidation, F = 96,485.34 C/mol e^-).

References

1 Ellis, W. C.; McDaniel, N. D.; Bernhard, S.; Collins, T. J. *J. Am. Chem. Soc.* **2010**, *132*, 10990.

2 Fillol, J. L.; Codolá, Z.; Garcia-Bosch, I.; Gómez, L.; Pla, J. J.; Costas, M. *Nat. Chem.* **2011**, *3*, 807

3 McCool, N. S.; Robinson, D. M.; Sheats, J. E.; Dismukes, G. C. *J. Am. Chem. Soc.* **2011**, *133*, 11446.

4 Wasylenko, D. J.; Palmer, R. D.; Schott, E.; Berlinguette, C. *P. Chem. Commun.* **2011**, *47*, 4249.

5 Luo, J.; Rath, N. P.; Mirica, L. M. *Inorg. Chem.* **2011**, *50*, 6152.

6 Evangelisti, F.; Güttinger, R.; Moré, R.; Luber, S.; Patzke, G. R. *J. Am. Chem. Soc.* **2013**, *135*, 18734.

7 Hong, D.; Jung, J.; Park, J.; Yamada, Y.; Suenobu, T.; Lee, Y.; Nam, W.; Fukuzumi, S. *Energy Environ. Sci.* **2012**, *5*, 7607.

8 Barnett, S. M.; Goldberg, K. I.; Mayer, J. M. *Nat. Chem.* **2012**, *4*, 498.

9 Zhang, M-T.; Chen, Z.; Kang, P.; Meyer, T. J. *J. Am. Chem. Soc.* **2013**, *135*, 2048.

10 Beisinger, M. C.; Lau, L. W. M.; Gerson, A. R.; Smart, R. St.C. *Appl. Surf. Sci.* **2010**, *257*, 887.

11 Biesinger, M. C.; Payne, B. P.; Grosvenor, A. P.; Lau, L W. M.; Gerson, A. R.; Smart, R. St.C. *Appl. Surf. Sci.* **2011**, *257*, 2717.

12 Moulder, J. F.; Stickle, W. F>; Sobol, P. E.; Bomben, K. D. *Handbook of X-ray Photoelectron Spectroscopy*, Chastain, J.; King, R. C. Jr. Eds. Physical Electronics, Inc.: Eden Prairie, MN; 1995 pp 83-89.

13 Frost, D. C.; McDowell, C. A.; Woolsey, I. S. *Chem. Phys. Lett.* **1972**, *17*, 320.

14 Mattogno, G.; Zanoni, R.; Giusto, D.; Russo, G.; Sisti, L. *Inorg. Chim. Acta* **1985**, *104*, 9.

15 Santato, C.; Odziemkowski, M.; Ulmann, M.; Augustynski, J. *J. Am. Chem. Soc.* **2001**, *123*, 10639-10649.

16 Klepser, B. M.; Bartlett, B. M. *J. Am. Chem. Soc.* **2014**, *136*, 1694.

Chapter 6

Outlook and Conclusions

6.1 Introduction

The primary objective of this thesis has been exploring a new approach to solar water oxidation wherein fast molecular catalysts are anchored to metal oxide semiconductors that act as a light absorber. As a result of this research, we have developed several photoelectrochemical systems that have helped lay the foundation for future research in this field. There are several important questions that this research has raised, and these questions must be addressed in order to demonstrate the actual power of this approach for all solar catalysis. First, what are the catalytically active species under illumination? Second, how do the intrinsic electronic properties of the semiconductor impact the photoelectrochemical performance of the catalyst-semiconductor material? Finally, how can semiconductors be employed to enable other solar oxidation reaction? The ensuing outlook grapples with these questions in more detail considering what is currently know about each issue and identifying how projects in our lab are already addressing these questions.

6.2 Outlook

6.2.1 Catalytically active species

The major challenge for this research, and really for all homogeneous catalysis, is proving that the molecular catalyst remains intact during the course of the reaction. Unlike traditional homogeneous systems, the approach employed in this thesis inherently heterogenizes the molecular catalysts. However, the central hypothesis to this work is that the molecular catalyst will retain its homogeneous reaction pathway when anchored onto the semiconductor surface. There are several techniques for spectroscopically identifying molecular intermediates for various catalysts that have been employed throughout the course of this research. Unfortunately, one of the key observations that has been made in the previous chapters, is that the catalysts fall off of the surface under reaction conditions. As a result, there is no concrete evidence that the molecular catalysts are remaining intact on the surface.

The main question that surfaces from these observations is: What is the identity of the active species on the electrode surface? It has been demonstrated through a series of control experiments in Chapter 3 that the active species is only capable of forming through attaching the specific molecular catalyst to WO_3. Furthermore, the active species remains present on the surface even after the catalyst is no longer visible spectroscopically. As is, the catalytic system we have developed will not be able to directly answer this question. Therefore, a seemingly simpler question must first be answered to point future research in the right direction. Namely, how can the stability of the covalent anchors be improved?

Anchoring groups have primarily been examined for the purpose of creating new dye sensitized solar cells (DSSCs). The main concerns have typically been the rate of charge transfer, stability under illumination, and ease of synthesis. However, because DSSCs

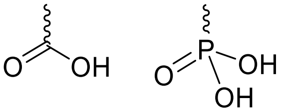

Scheme 6.1 Most commonly targeted anchoring groups for attaching molecules to semiconductors that are also susceptible to hydrolysis

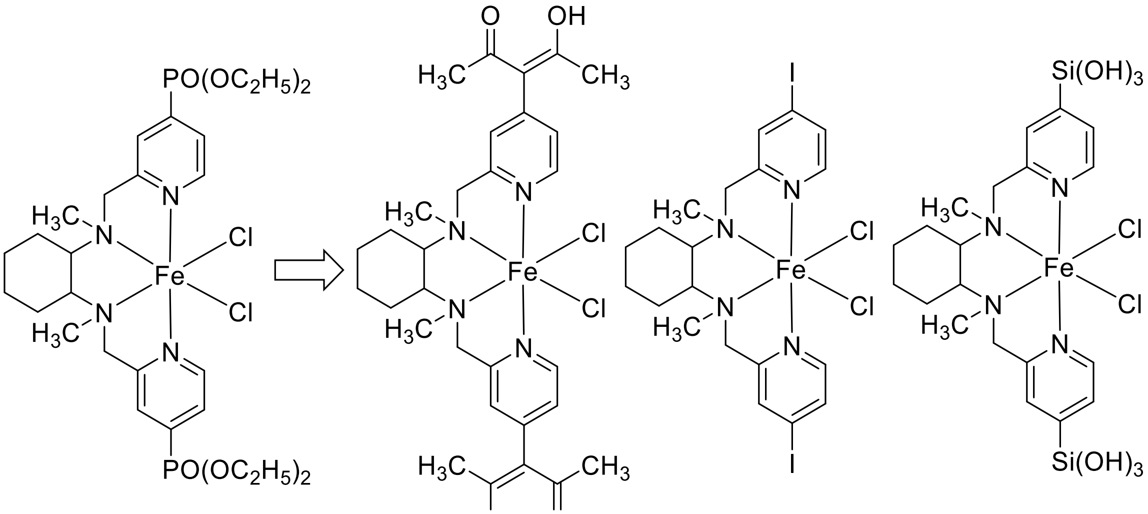

Fe-2

Scheme 6.2 Targeted anchoring groups for Fe-2 analogs that are less susceptible to hyrdolysis operate in non-aqueous electrolytes, aqueous stability is rarely considered when designing new anchoring groups. As a result, the common anchoring groups rely on metal-oxygen-R bonds where the R-O bond is typically an organic functional group that is relatively prone to hydrolysis (Scheme 6.1).[1] Furthermore, in aqueous environments, there is little that can be done to prevent surface exchange of the surface metal-aquo/complex bonds on the surface of the semiconductor.[2] Recently, there have been several new anchoring groups that have been reported that are not as susceptible to hydrolysis.[1,3,4] The alternative anchoring groups have been pursued synthetically for application on the iron catalyst reported in Chapter 3 as depicted in

Scheme 6.2. However, stability experiments in aqueous electrolytes have not been conducted for these complexes.

Instead of synthesizing the more complex ligand for the iron catalyst, efforts have refocused on using model complexes to rapidly examine the stability of various new anchoring groups. As specifically depicted in Scheme 6.3, work is ongoing looking at silanol and iodo surface coverages for another ruthenium complex on TiO_2. This work is in its initial stages, but the iodo binding affinities have shown good surface coverage and moderate stability in acidic environments using Raman spectroscopy. One question that has arisen from these initial experiments is how do the complexes remain bound to the surface? In other words, what is the stability of physisorbed vs. covalently bound complexes on an electrode surface? The results obtained previously have suggested that the catalyst must be covalently bound to the electrode, however, the covalency of their attachment has not been directly proven either because Raman stretching frequencies for the anchoring groups have not demonstrated shifting or reducing intensities. Therefore, it is of interest to develop a better protocol to more directly examine the binding of the

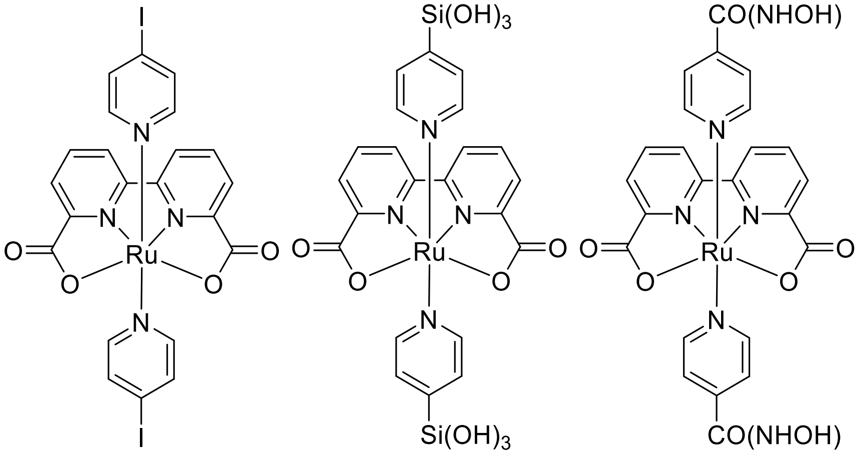

Scheme 6.3 Ruthenium model complexes still being pursued for anchoring experiments

complexes.

Once the stability of the catalyst on the surface can be improved, then the major question about the catalytically active species can be appropriately addressed. The main goal is to understand how binding the catalysts to the surface impacts the catalytic mechanism and to help understand whether the complex is indeed staying intact under illumination. This question is the most important question that needs to be addressed with future research because it has been demonstrated in several places that molecular complexes often serve as mere precursors for heterogeneous catalysts.[5] Furthermore, understanding how the mechanism of a catalyst changes on a surface could lead to selection criteria for alternate catalysts in future research.

6.2.2 Exploring other semiconductors

Another major question that this thesis raises is what properties should a semiconductor possess in order to successfully activate a molecular catalyst under illumination? For instance, must the conduction band have a certain potential energy difference between it and the catalyst? What is the minimum charge carrier density required to activate different catalysts? Is it the same for different catalysts? How could this approach be applied to non-oxide semiconductors? Answering this question would have a profound impact on the way semiconductor-catalyst are paired and the expectations for each pairing.

Chapter 2 and 4 have already briefly discussed attempts to use different semiconductors in attempt to improve each catalytic system. From these results, it is speculated that the amount of light the semiconductor absorbs is most important and the conduction band position plays an important role in determining successful activation of the catalysts. Furthermore, this idea suggests that back electron transfer from the conduction band plays an important role in determining successful photoelectrochemical enhancement. However, both of these reports exhibit poor control over morphology, surface area, and photoelectrochemical performance. And, because the intrinsic properties like band composition, hole mobility, etc. of each semiconductor are so different, it’s plausible that there are other factors that significantly impact the photoelectrochemical performance. Therefore, it would be important to carry out these experiments using more controlled syntheses and include a material like $BiVO_4$ that has an ideal band structure for overall water splitting. This controlled approach, coupled with computational modeling, should allow for more concrete comparisons to be made for different semiconductors about the requirements for successful catalysis.

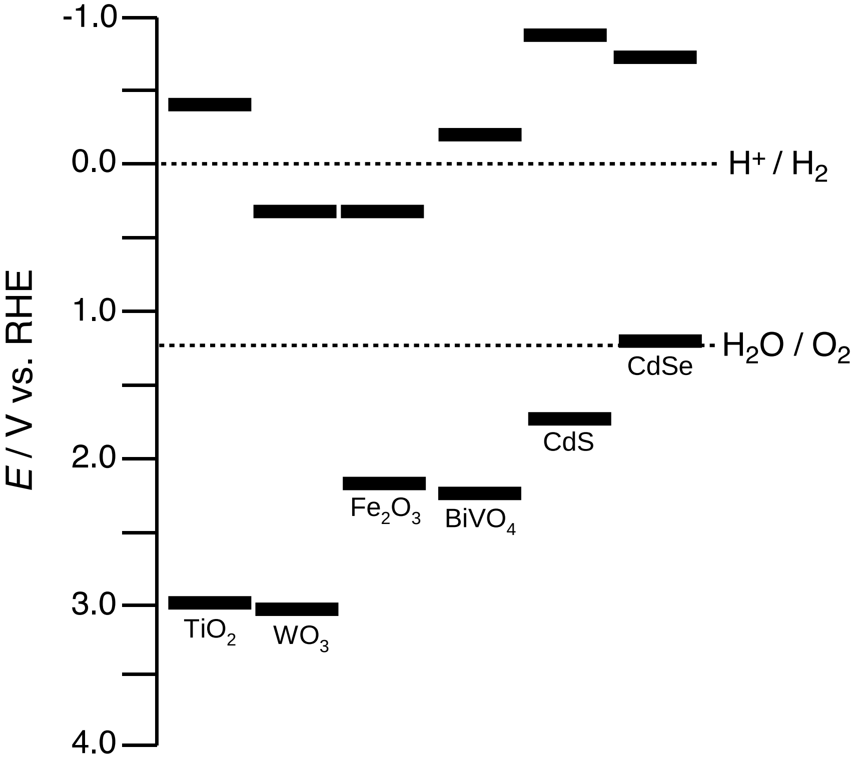

Figure 6.1 Band energy diagram for common semiconductors including non-oxide semiconductors

In addition to learning what physical properties are important for metal oxide semiconductors, this approach offers an exciting possibility to passivate non-oxide surfaces. Non-oxide semiconductors are interesting primarily because they tend to have more favorable band energies because the valence band is not comprised of the O 2p orbitals (see Figure 6.1).[6] Because the metal still contributes primarily to the conduction band, the band gap is much smaller, but the band edges are still typically remain well suited for overall water splitting. Unfortunately, non-oxide semiconductors, like cadmium sulfide (CdS) or cadmium selenide (CdSe), are unstable in aqueous environments under illumination. The semiconductors are unstable in aqueous environments under illumination because as the surface begins oxidizing water, the corresponding oxide forms on the semiconductor surface and the surface becomes passivated.

However, if the molecular catalysts are the primarily active species on the semiconductor surface, then the catalyst should stabilize the non-oxide semiconductor because the semiconductor is no longer performing water oxidation and therefore no longer auto-oxidizing its surface. To examine this hypothesis, CdS or CdSe would serve as excellent model systems for this approach because of their band edge alignment for both water oxidation and proton reduction. Stability should be the primary concern in this case as opposed to seeking photocurrent enhancement as has been previously examined because a linear sweep voltammograms under illumination prior to modification could result in some initial decay that is not recoverable.

6.2.3 Alternative organic oxidation reactions

Although this thesis has focused on the application of metal oxide semiconductors as light absorbers for oxidizing molecular water oxidation catalysts, the most exciting application of this approach lies in using solar energy to catalyze other reactions that require sacrificial oxidants. The approach that we have helped develop could be an excellent solution to photocatalysis of different oxidation reactions. For instance, as is demonstrated in Chapter 5, a lot more oxidative potential energy is accessible using semiconductors as the light absorber. The excess potential energy could allow many homogeneous catalysts to reach the higher oxidation states that are often only accessible with one or two sacrificial oxidants.

One specific application of this approach is currently underway in the Bartlett Lab. In this attempt, a manganese salophen complex is being targeted for its ability to oxidize alkenes to epoxides using peroxo-intermediates.[7] This target is an ideal system because instead of using hydrogen peroxide as the sacrificial oxidant, solar energy will be used to make the peroxo- intermediate from water under illumination. As illustrated in Scheme 6.4, catalyst **1** will be anchored to the electrode surface, and oxidize styrene (a model substrate) in the presence of water under illumination. To date, this research has revealed that modification of the manganese salen complex through the axial pyridine ligand is unable to remain coordinated to a TiO_2 electrode surface. As a result, work is underway to attach this catalyst through the salophen ligand to improve surface stability in the presence

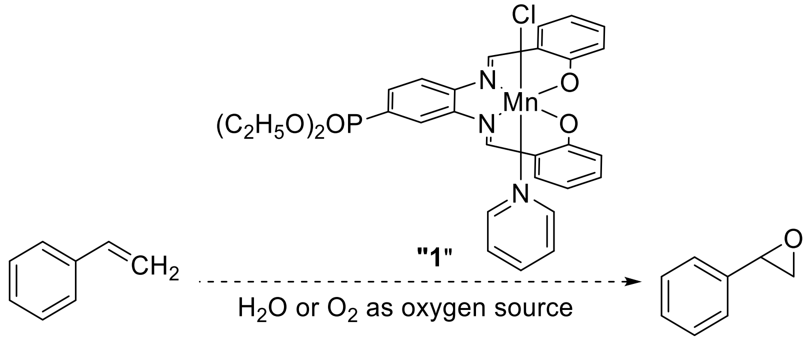

Scheme 6.4 Manganese salophen catalyst for oxidation of styrene
of aqueous solutions.

In the current example being pursued, the reaction of interest still oxidizes the substrate through oxygen-carbon bond formation. To truly understand the power of this approach, it is of interest to examine whether non-oxygenation reactions can be performed when the corresponding catalyst is anchored to a metal-oxide semiconductor. One area of specific interest is the oxidation of amine substrates. Recent work in the Bartlett Lab has been directed at exploring the ability of $CuWO_4$ to oxidize amines photoelectrochemically. Along this same vein, it remains to be determined whether the $CuWO_4$ is selective for amine oxidation when the substrate contains multiple functional groups (amines or alcohols). Therefore, a molecular species bound to the $CuWO_4$ electrodes could serve as a method to improve the selectivity on the modified semiconductor as is demonstrated in Chapter 3 for **Fe-2** on WO_3 towards water oxidation if $CuWO_4$ exhibits poor oxidative selectivity for different substrates.

Along the lines of oxidizing organic substrates, carbon-carbon (C-C) and carbon-heteroatoms bond forming reactions are an essential reactions in organic chemistry especially for sp^2 carbons.[8] In many instances, the homogeneous catalysts used for these reactions are oxidized through oxidative addition of carbon-halogen (C-X) or carbon-hydrogen (C-H) bonds. However, in certain instances further oxidation of the catalyst is required to facilitate reductive elimination. To achieve higher oxidation states for these catalysts, sacrificial oxidants like (diacetoxyiodo)benzene [$PhI(OAc)_2$] or benzoquinone are often used (often in large excess).[9,10] A heterogeneous, catalytic system that retained high reactivity under illumination would be an exciting new development for this type of catalysis since purification would be simplified through removal of a stoichiometric byproduct of the reaction.

6.3 Conclusions

This chapter is intended to examine the exciting questions that result directly from the research contained in this thesis. The basic understanding of the impact this new approach has on solar oxidation reactions is still in its infancy. As a result, there are numerous questions about what is catalytically active on the surface under illumination and how the semiconductor plays a role in facilitating the reaction. However, the most exciting aspect of the chemistry discussed herein are the applications to other oxidation reactions. The application of a metal-oxide semiconductor as a light absorber and scaffold for molecular catalysts has promise for an array of different reactions that require sacrificial oxidants, and applying this approach to other reactions will demonstrate the true impact of this approach for solar oxidative catalysis.

References

1 Young, K. J.; Martini, L. A.; Milot, R. L.; Snoeberger III, R. C.; Batista, V. S.; Schmuttenmaer, C. A.; Crabtree, R. H.; Brudvig, G. W. *Coord. Chem. Rev.* **2012**, *256*, 2503.

2 Brown, G. E. Jr.; Henrich, V. E.; Casey, W. H.; Clark, D. L.; Eggleston, C.; Felmy, A.; Goodman, D. W.; Grätzel, M.; Maciel, G.; McCarthy, M. I.; Nealson, K. H.; Sverjensky, D. A.; Toney, M. F.; Zachara, J. M. *Chem. Rev.* **1999**, *99*, 77.

3 Gao, Y.; Ding, X.; Liu, J.; Wang, L.; Lu, Z.; Li, L.; Sun, L. *J. Am. Chem. Soc.* **2013**, *135*, 4219.

4 Putans, B. A.; Bishop, L. M.; Hamers, R. J. *Chem. Mater.* **2014**, *26*, 3651.

5 Schley, N. D.; Blakemore, J. D.; Subbaiyan, N. K.; Incarvito, C. D.; D'Souza, F.; Crabtree, R. H.; Brudvig, G. W. *J. Am. Chem. Soc.* **2011**, *133*, 10473.

6 Kudo, A.; Miseki, Y. *Chem. Soc. Rev.* **2009**, *38*, 253.

7 a) Silva, A. R.; Figueiredo, J. L.; Freire, C.; de Castro, B. *Micro. Meso. Mater.* **2004**, *68*, 83; b) Mirkhani, V.; Moghadam, M.; Tangestaninejad, S.; Bahramian, B. *Appl. Catal. A.* **2006**, *311*, 43.

8 Reviews: a) Brown, J. M.; Cooley, N. A. *Chem. Rev.* **1988**, *88*, 1031; b) Hartwig, J. F. *Nature* **2008**, *455*, 314; c) Lyons, T. W.; Sanford, M. S. *Chem. Rev.* **2010**, *110*, 1147.

9 Deprez, N. R.; Sanford, M. S. *Inorg. Chem.* **2007**, *46*, 1924.

10 Hull, K. L.; Sanford, M. S. *J. Am. Chem. Soc.* **2009**, *131*, 9661.

Appendix A

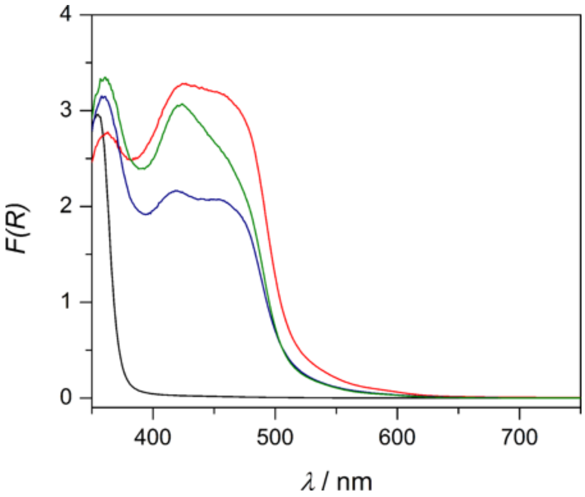

Figure A.1 Diffuse reflectance UV-Vis spectra of bare TiO_2 (black) and **Ru-COOH** (red), **Ru-PO(OC$_2$H$_5$)$_2$** (blue), and **Ru-CO(NHOH)** (green) on TiO_2

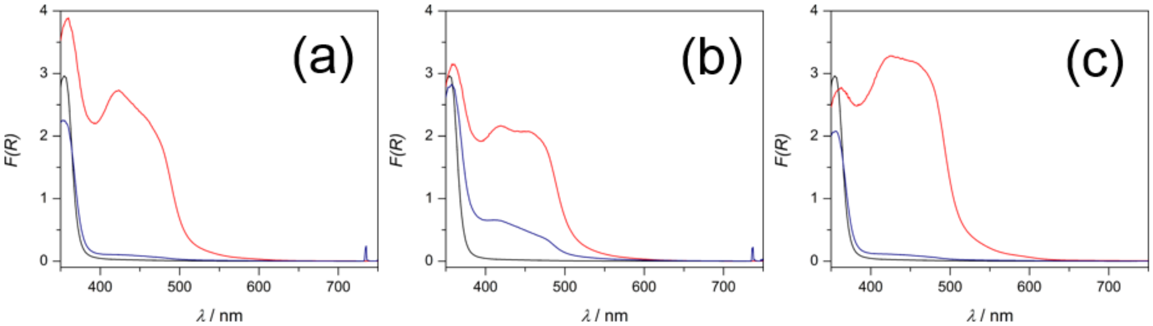

Figure A.2 Diffuse reflectnce UV-Vis spectra of bare TiO_2 (black) compared to **Ru-COOH** (a), **Ru-PO(OC$_2$H$_5$)$_2$** (b), and **Ru-CO(NHOH)** (c) before (red) and after (blue) soaking in pH 1.1 $K_xH_{(3-x)}PO_4$ for 18 hours

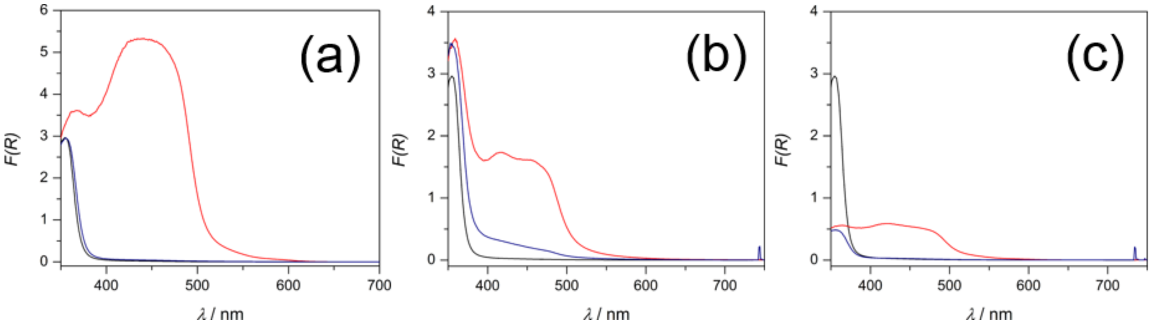

Figure A.3 Diffuse reflectnce UV-Vis spectra of bare TiO_2 (black) compared to **Ru-COOH** (a), **Ru-PO(OC_2H_5)$_2$** (b), and **Ru-CO(NHOH)** (c) before (red) and after (blue) soaking in pH 7.0 $K_xH_{(3-x)}PO_4$ for 18 hours

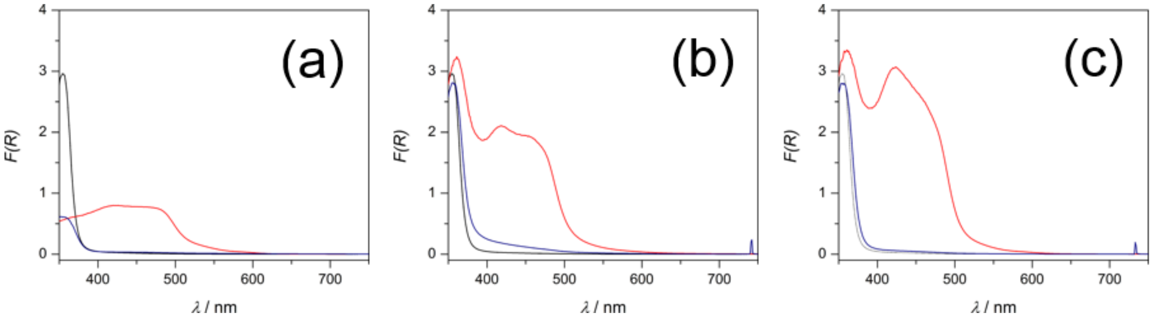

Figure A.4 Diffuse reflectnce UV-Vis spectra of bare TiO_2 (black) compared to **Ru-COOH** (a), **Ru-PO(OC_2H_5)$_2$** (b), and **Ru-CO(NHOH)** (c) before (red) and after (blue) soaking in pH 10.0 $K_xH_{(3-x)}PO_4$ for 18 hours

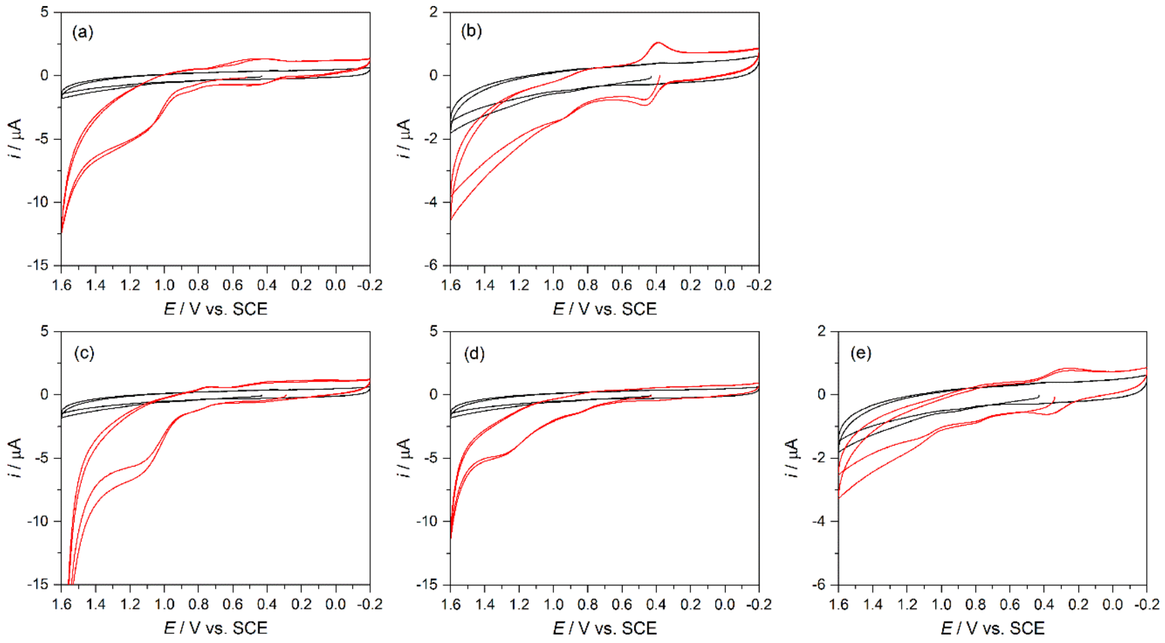

Figure A.5 Cyclic voltammetry of **Ru** (a), **Ru-P$_2$** (b), **Ru$_2$** (c), **Ru$_2$-P$_2$** (d), and **Ru$_2$-P** (e) compared to blank electrolyte of 100 mM TBAPF$_6$ in wet CH$_3$CN at 20 mV s^{-1} using GC WE, Pt CE, and SCE RE

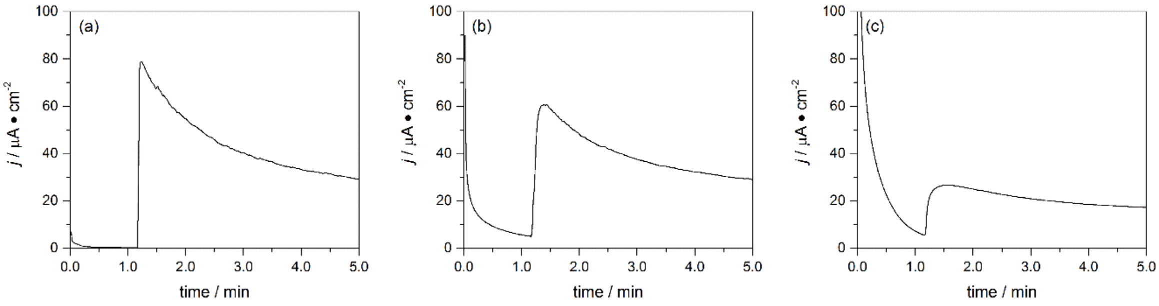

Figure A.6 *j-t* curves for bare TiO$_2$ (a), **Ru$_2$-P$_2$** on TiO$_2$ (b), and **Ru$_2$-P** on TiO$_2$ (c) in 100 mM Na$_2$SO$_4$ at pH 3 under AM 1.5G 100 mW cm^{-2} illumination held at 1.23 V vs. RHE using Pt CE and Ag/AgCl RE

Appendix B

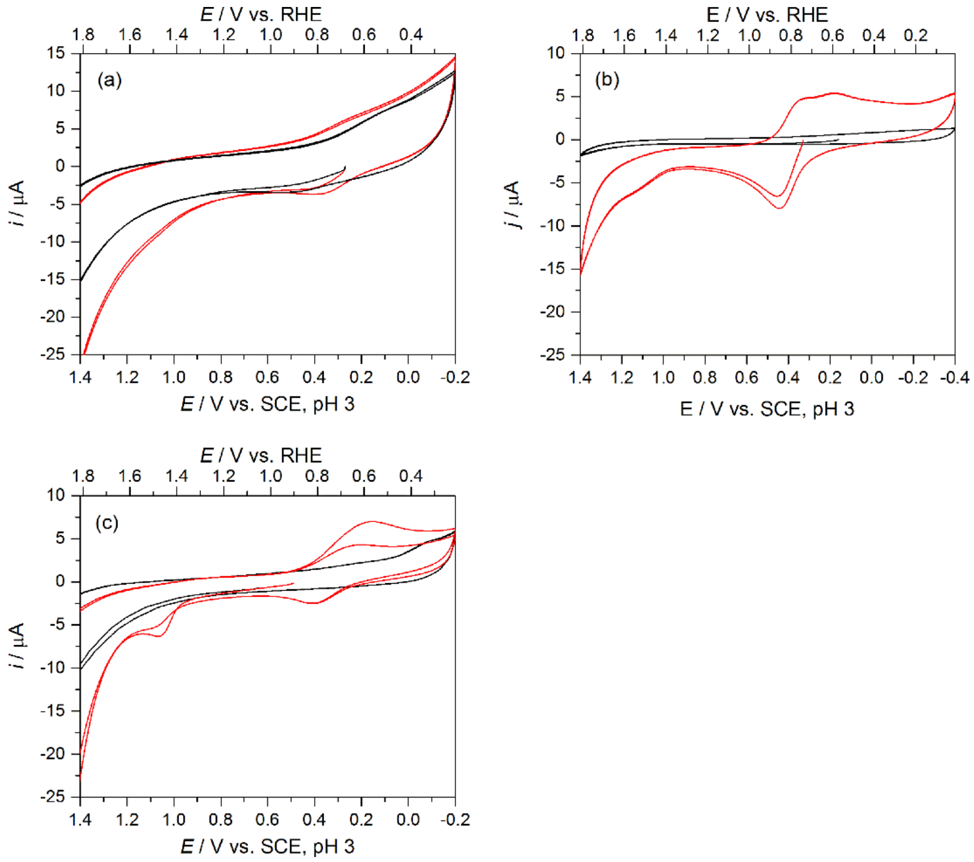

Figure B.1 Aqueous CVs of **Fe-1** (a), **Fe-2** (b), **Fe-3** (c), and **Fe-4** (d) in 100 mM Na_2SO_4 at pH 3 at 20 mV s^{-1} using GC WE, Pt CE, and SCE RE

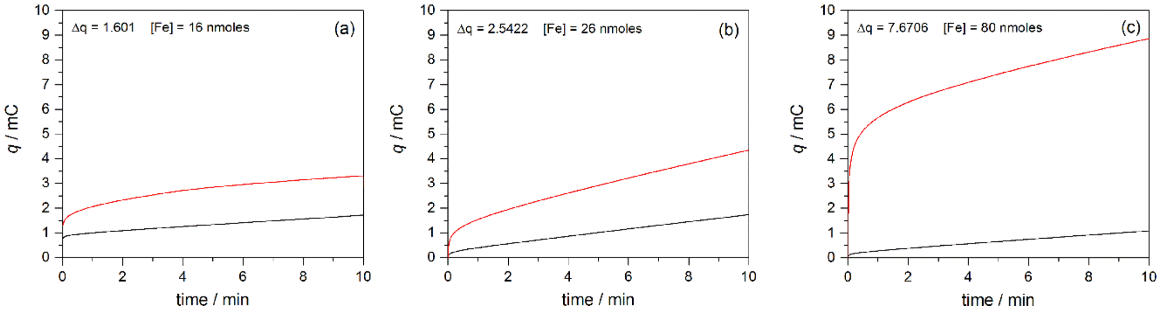

Figure B.2 Representative surface coverage measurements of **Fe-2** (a), **Fe-3** (b), and **Fe-4** (c) on WO_3 (red) compared to the same WO_3 film prior to modification (black) via bulk electrolysis in 100 mM $TBAPF_6$ with CH_3CN at 0.60 V vs. SCE for 10 minutes using Pt CE and SCE RE

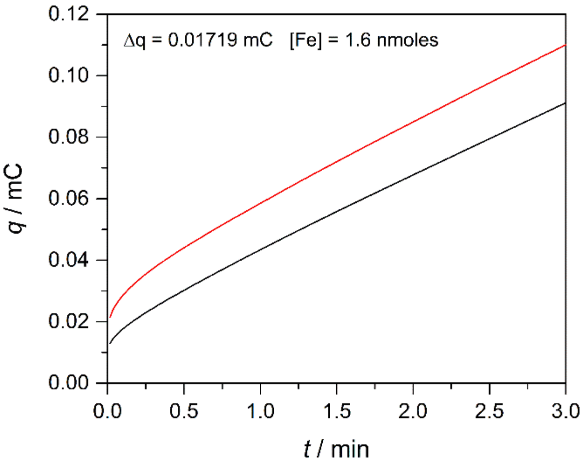

Figure B.3 Surface coverage of **Fe-2** on FTO (red) compared to bare FTO (black) via bulk electrolysis in 100 mM $TBAPF_6$ with CH_3CN at 0.60 V vs. SCE for 3 minutes using Pt CE and SCE RE

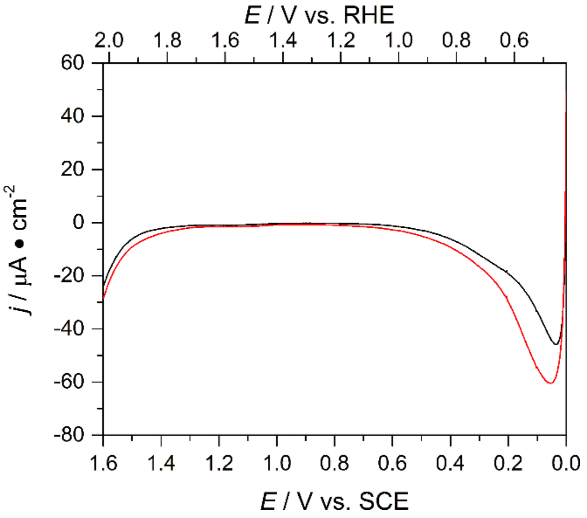

Figure B.4 Dark LSV of **Fe-2** on WO_3 (red) compared to bare WO_3 (black) for comparison in 100 mM Na_2SO_4 at pH 3 at 20 mV s^{-1} using Pt CE and SCE RE

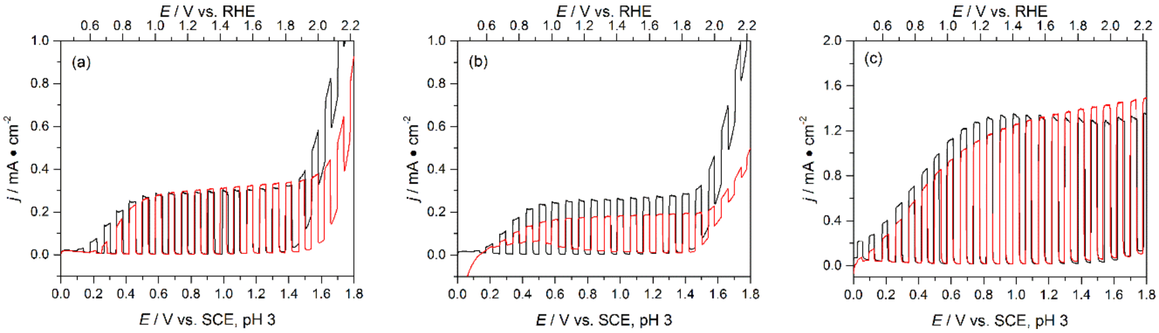

Figure B.5 Control LSVs for acetonitrile (a), $FeCl_2$ (b), and ligand **2** (c) on WO_3 (red) vs. bare WO_3 (black) in 100 mM Na_2SO_4 at pH 3 at 20 mV s^{-1} using Pt CE and SCE RE

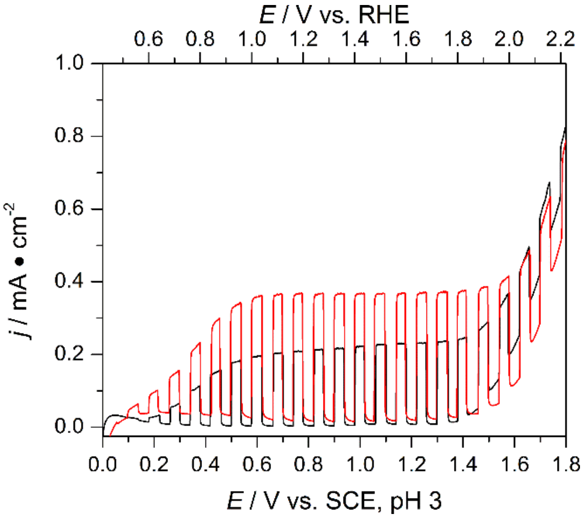

Figure B.6 LSV of 0.8 μm thick WO_3 with **Fe-2** bound (red) or not (black) in 100 mM Na_2SO_4 at pH 3 at 20 mV s^{-1} using Pt CE and SCE RE

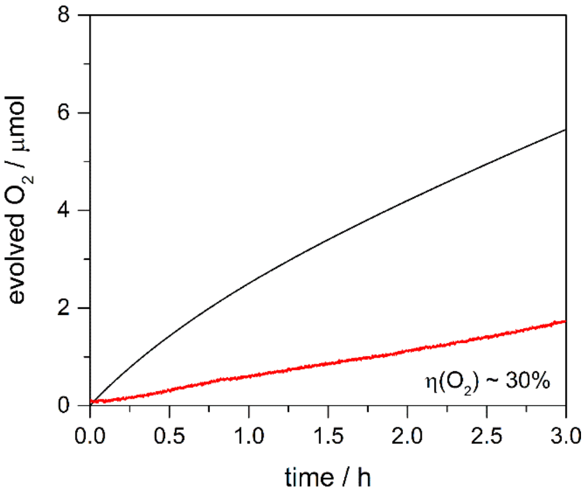

Figure B.7 Faradaic efficiency of ligand **2** bound to WO_3 in 100 mM Na_2SO_4 at pH 3 at 20 mV s^{-1} using Pt CE and SCE RE determined from the theoretical (black) and actual (red) yield of O_2

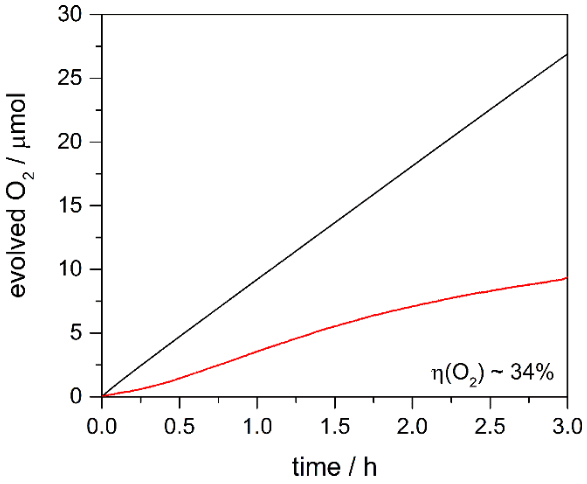

Figure B.8 Faradaic efficiency of unmodified WO_3 with **Fe-2** in solution in 100 mM Na_2SO_4 at pH 3 at 20 mV s^{-1} using Pt CE and SCE RE determined from theoretical (black) and actual (red) yield of O_2

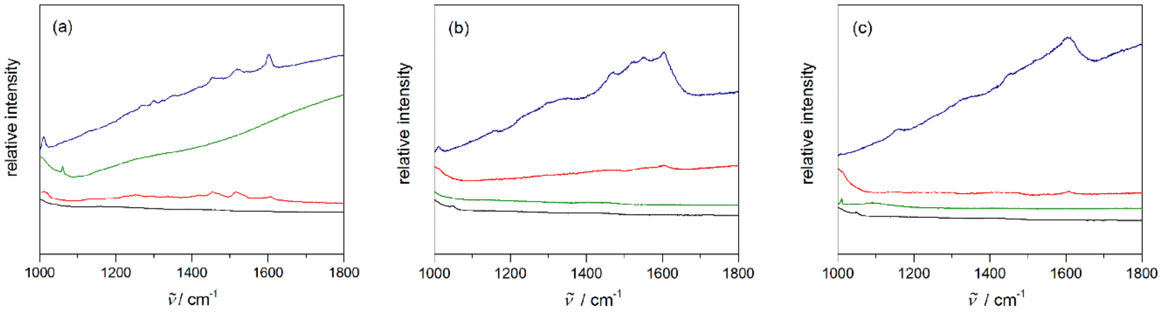

Figure B.9 Raman spectroscopy of **Fe-2** (a), **Fe-3** (b), and **Fe-4** (c) on WO_3 before (red) and after (green) PEC compared to bare WO_3 (black) or the catalyst powder (blue)

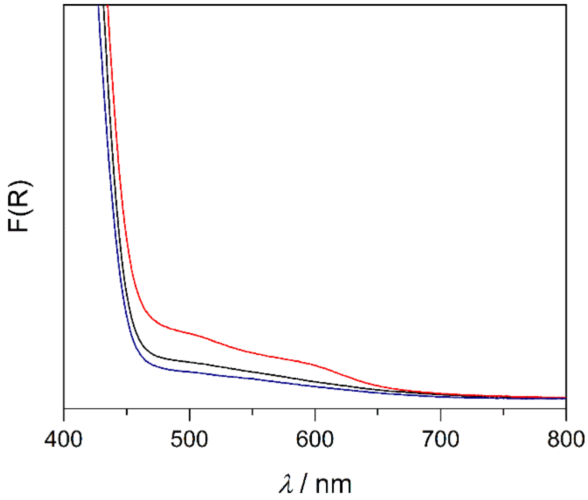

Figure B.10 Diffuse relfectance UV-Vis spectroscopy of **Fe-2** on WO_3 before (red) and after (blue) PEC compared to bare WO_3

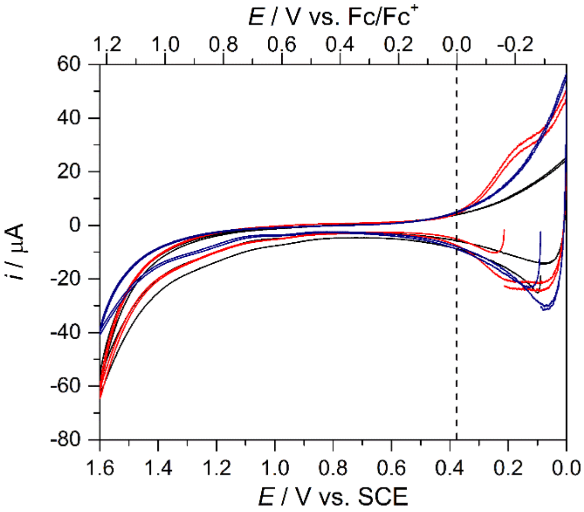

Figure B.11 CV of **Fe-2** on WO_3 before (red) and after (blue) PEC compared to bare WO_3 (black) in 100 mM $TBAPF_6$ with CH_3CN at 20 mV s^{-1} using Pt CE and SCE RE

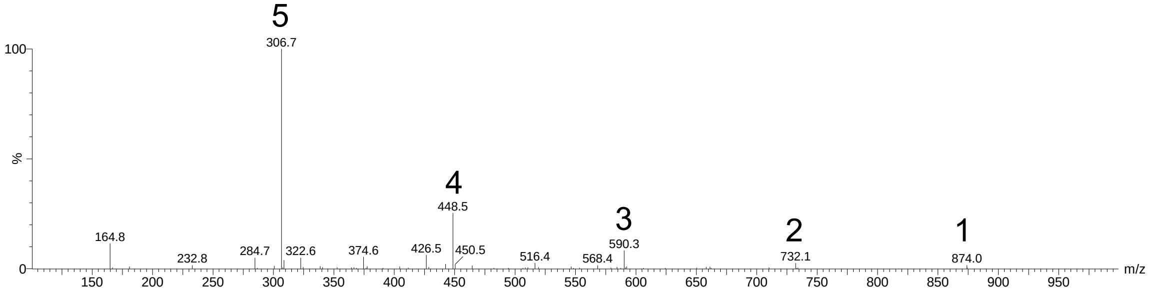

Figure B.12 ESI-MS^+ of 100 mM Na_2SO_4 pH 3 electrolyte after PEC at 1.23 V vs. RHE with **Fe-2** on WO_3

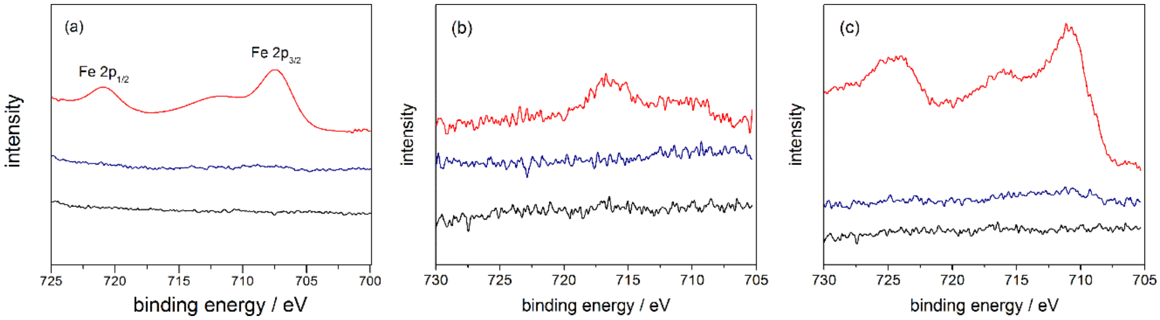

Figure B.13 XPS of **Fe-2** (a), **Fe-3** (b), and **Fe-4** (c) on WO_3 before (red) and after (blue) PEC compared to bare WO_3 (black)

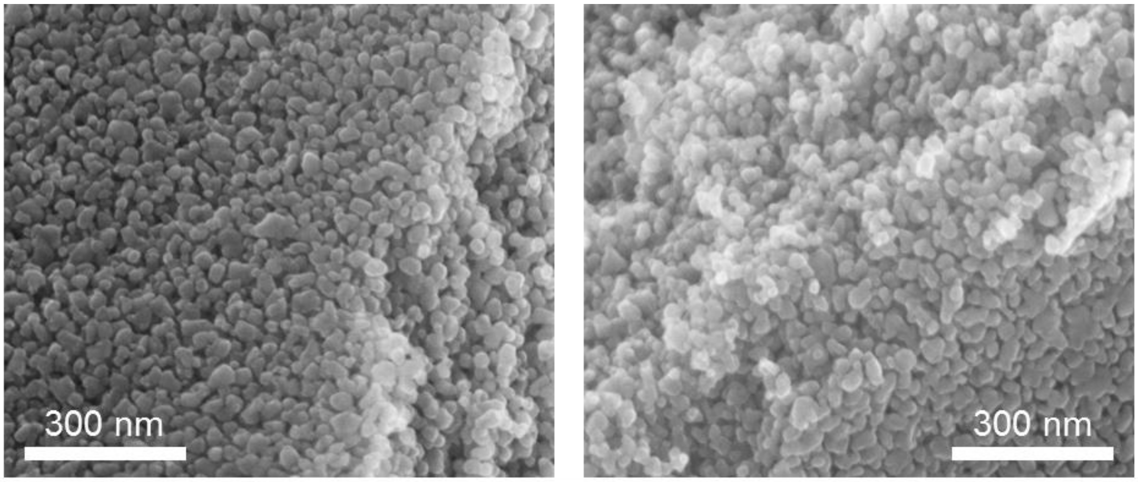

Figure B.14 Scanning electron microscopy of **Fe-2** on WO_3 before (left) and after (right) PEC

Appendix C

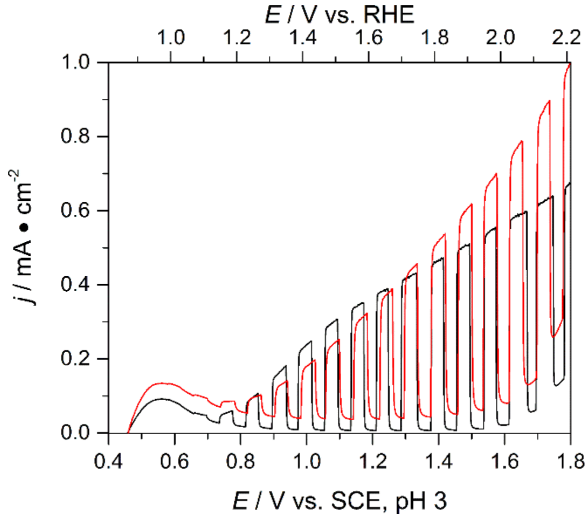

Figure C.1 Chopped light LSV of **Fe-2** on BiVO4 (red) and bare BiVO4 (black) in 100 mM Na2SO4 pH 3 under AM 1.5G, 100 mW cm^{-2} illumination at 20 mV s^{-1} using Pt CE and SCE RE

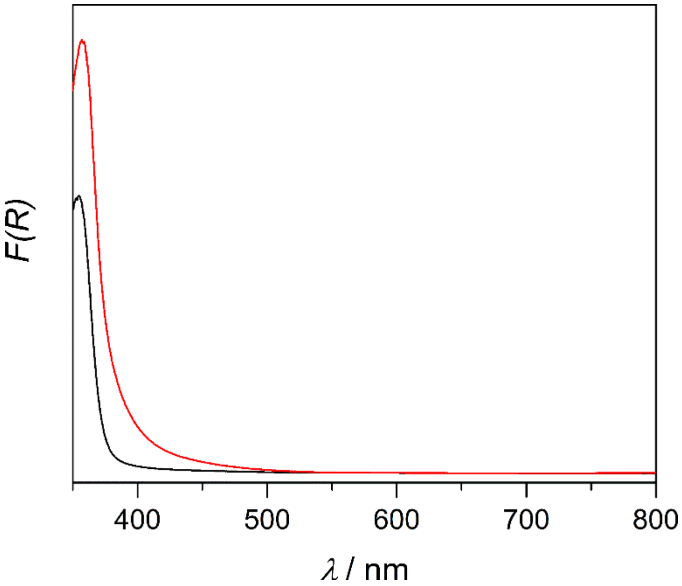

Figure C.2 Diffuse reflectance spectra of **Fe-2** on TiO_2 (red) compared to the same unmodified TiO_2 (black) electrode

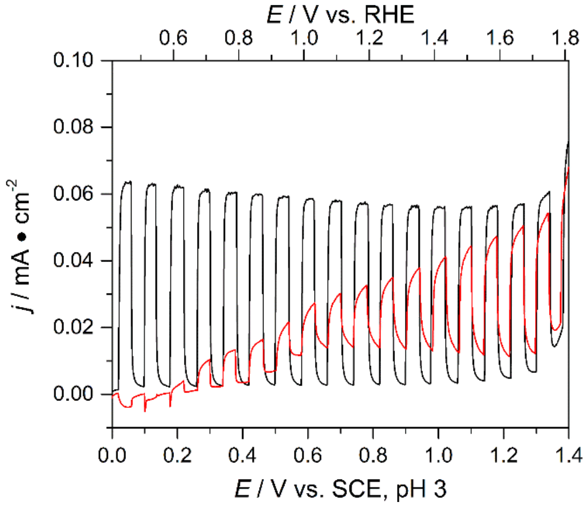

Figure C.3 Chopped light LSV of **Fe-2** on TiO2 (red) and bare TiO2 (black) in 100 mM Na2SO4 pH 3 under AM 1.5G, 100 mW cm^{-2} illumination at 20 mV s^{-1} using Pt CE and SCE RE

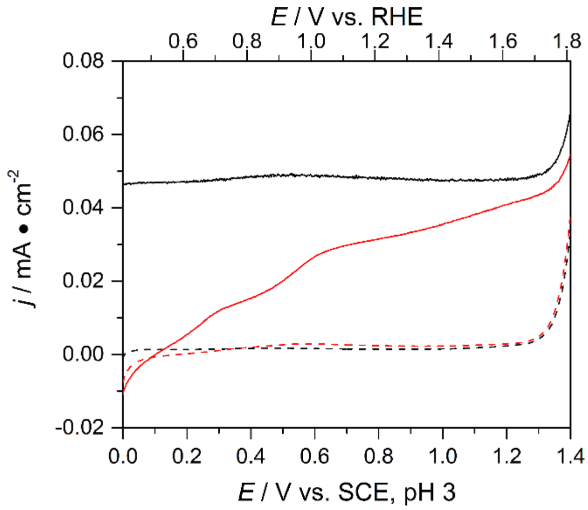

Figure C.5 Light (solid) and dark (dashed) LSV of **Fe-2** on TiO2 (red) and bare TiO2 (black) in 100 mM Na2SO4 pH 3 under AM 1.5G, 100 mW cm^{-2} illumination at 20 mV s^{-1} using Pt CE and SCE RE

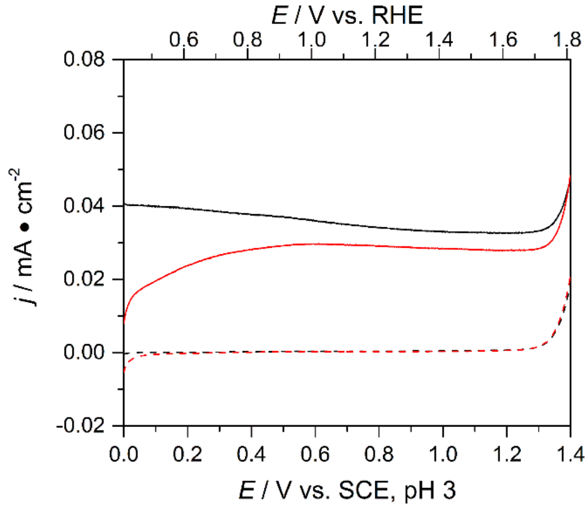

Figure C.4 Light (solid) and dark (dashed) LSV of **Fe-2** on TiO2 (red) and bare TiO2 (black) in 100 mM Na2SO4 pH 3 under AM 1.5G, 100 mW cm^{-2} illumination at 2 mV s^{-1} using Pt CE and SCE RE

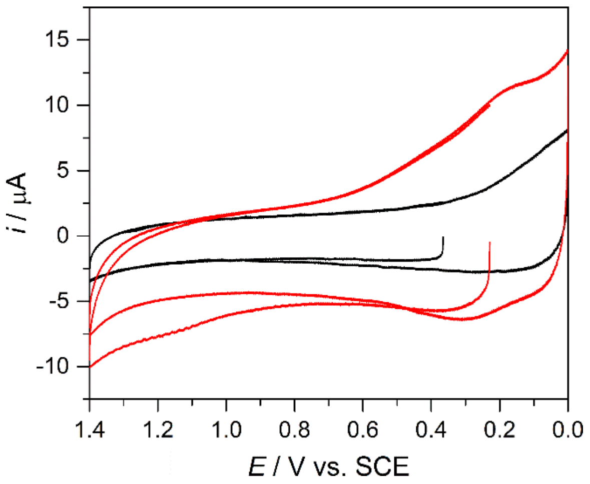

Figure C.6 Cyclic voltammetry of **Fe-2** on $CuWO_4$ (red) and bare $CuWO_4$ (black) in 100 mM $TBAPF_6$ CH_3CN at 100 mV s^{-1} using Pt CE and SCE RE

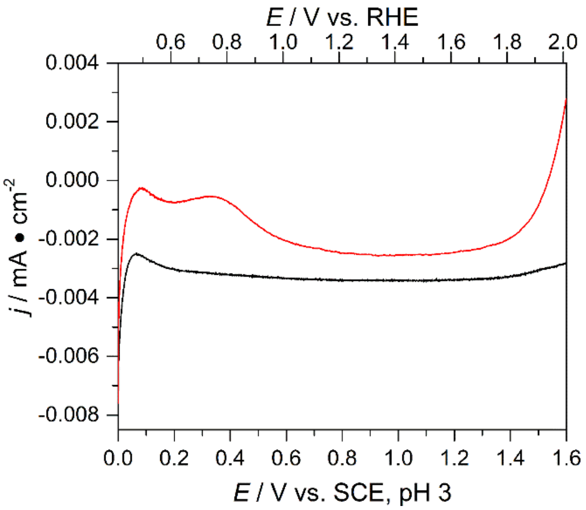

Figure C.7 Dark linear sweep voltammetry of **Fe-2** on $CuWO_4$ (red) and bare $CuWO_4$ (black) in 100 mM Na_2SO_4 pH 3 at 20 mV s^{-1} using Pt CE and SCE RE

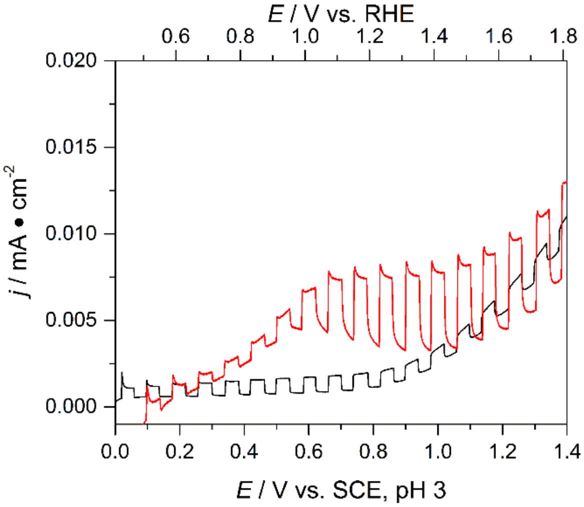

Figure C.8 Chopped light LSV of **Fe-2** on $SnWO_4$ (red) and bare $SnWO_4$ (black) in 100 mM Na_2SO_4 pH 3 under AM 1.5G, 100 mW cm^{-2} illumination at 20 mV s^{-1} using Pt CE and SCE RE

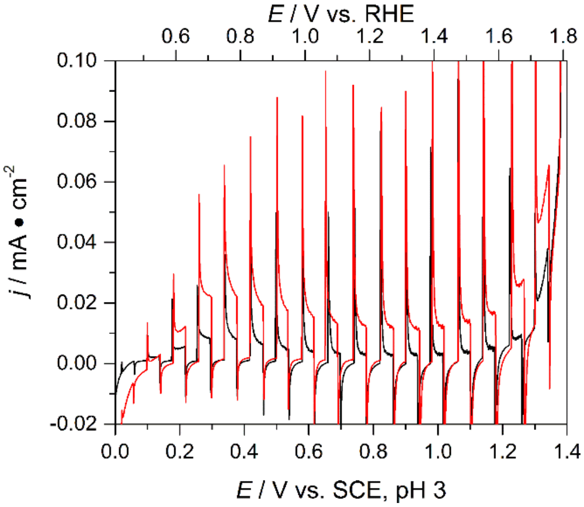

Figure C.9 Chopped light LSV of **Fe-2** on Fe_2O_3 (red) and bare Fe_2O_3 (black) in 100 mM Na_2SO_4 pH 3 under AM 1.5G, 100 mW cm^{-2} illumination at 20 mV s^{-1} using Pt CE and SCE RE

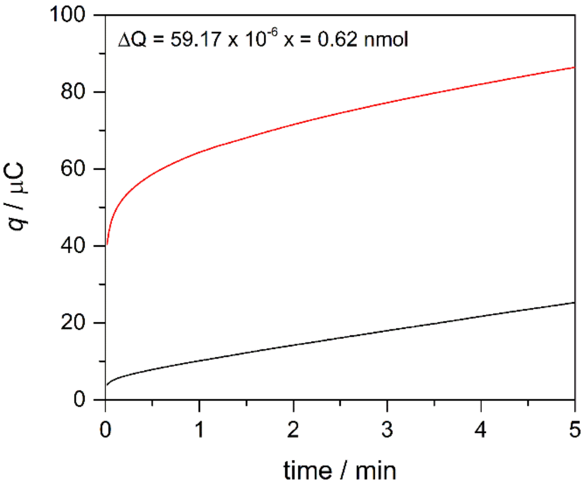

Figure C.10 Representative bulk electrolysis of **Fe-2** on $CuWO_4$ (red) and bare $CuWO_4$ (black) in 100 mM $TBAPF_6$ CH_3CN at 0.80 V using Pt CE and SCE RE

Electrode	Initial Q	After Q	ΔQ	mol e- passed	nmol Fe-2
1	1.99E-05	8.06E-05	6.07E-05	6.29E-10	0.63
2	1.87E-05	5.81E-05	3.95E-05	4.09E-10	0.41
3	1.94E-05	7.91E-05	5.98E-05	6.19E-10	0.62
				Average	0.55
				Standard deviation	0.12

Table C.1 Surface coverage calculations of **Fe-2** on $CuWO_4$

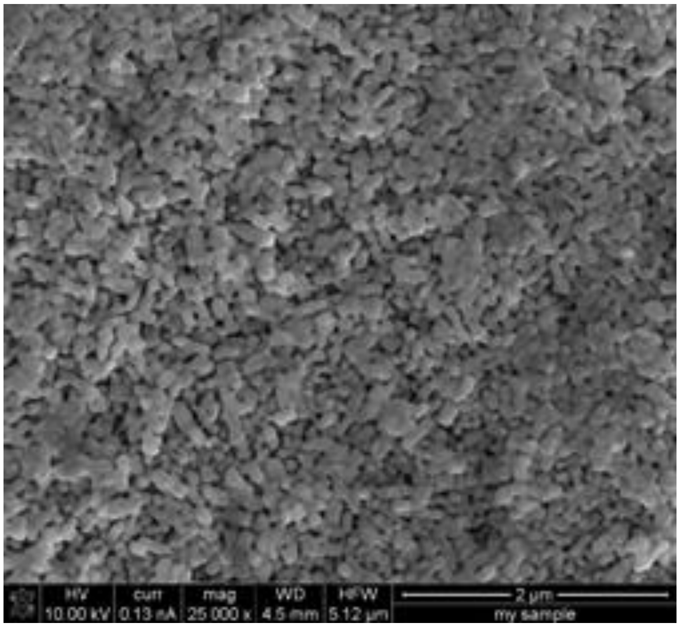

Figure C.11 Scanning electron micrograph of $CuWO_4$ prepared by spray pyrolysis taken by Charles R. Lhermitte

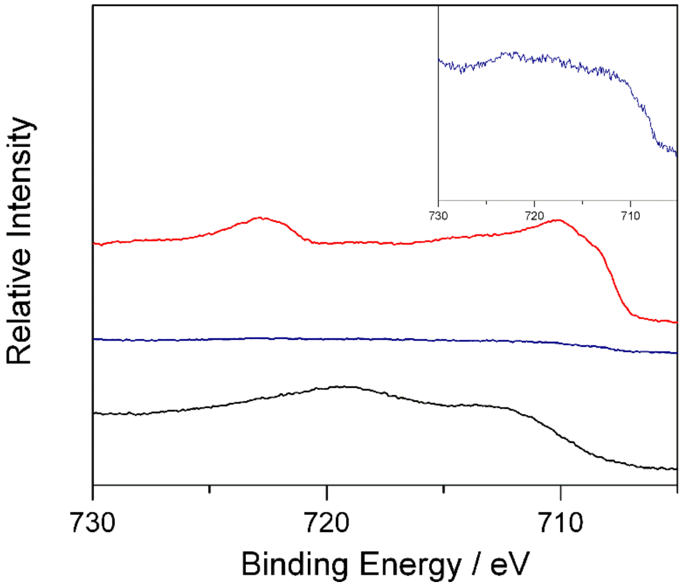

Figure C.12 X-ray photoelectron spectroscopy of **Fe-2** on $CuWO_4$ before (red) and after (blue, inset) photoelectrochemistry, compared to bare $CuWO_4$ (black)

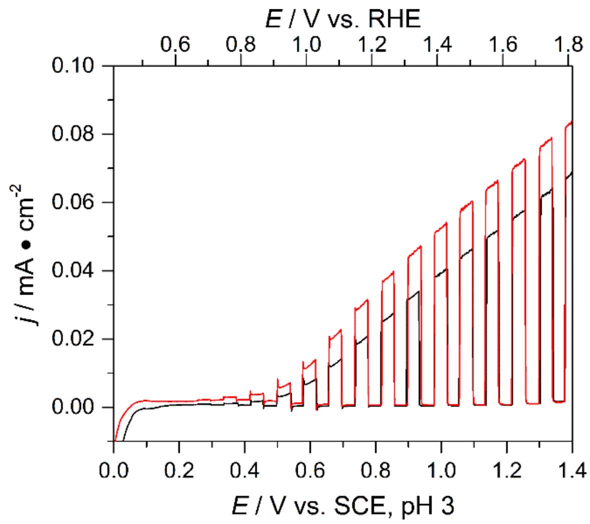

Figure C.13 Chopped light LSV of **Fe-2** on $CuWO_4$ (red) and bare $CuWO_4$ (black) prepared by an oriented sol-gel method developed by James Brancho in 100 mM Na_2SO_4 pH 3 under AM 1.5G 100 mW cm^{-2} illumination at 20 mV s^{-1} using Pt CE and SCE RE

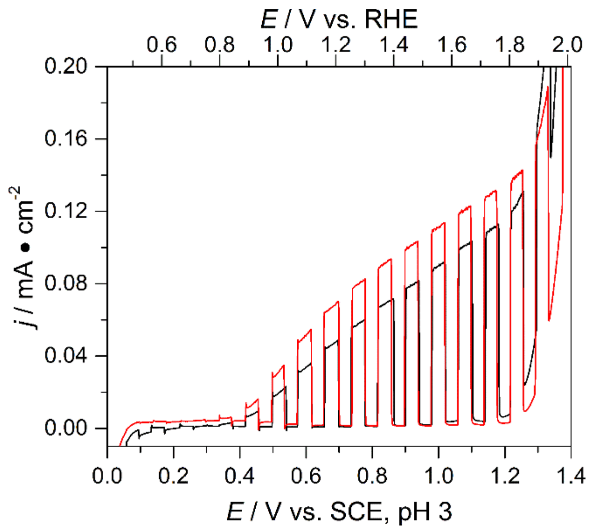

Figure C.14 Chopped light LSV of **Fe-2** on $CuWO_4$ (red) and bare $CuWO_4$ (black) prepared by sol-gel method Yourey et al. in 100 mM Na_2SO_4 pH 3 under AM 1.5G 100 mW cm^{-2} illumination at 20 mV s^{-1} using Pt CE and SCE RE

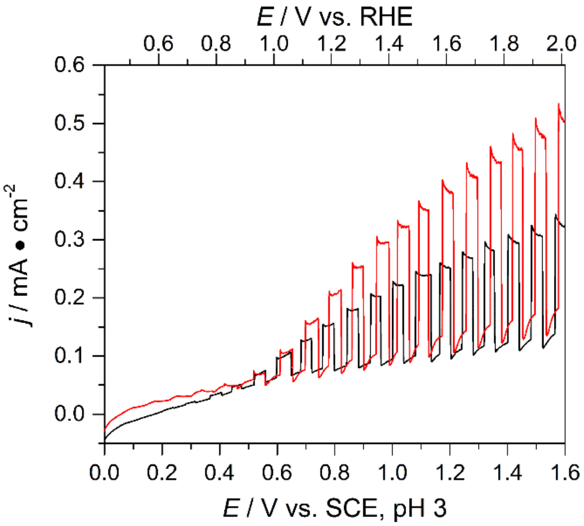

Figure C.15 Chopped light LSV of **Fe-2** on $CuWO_4$ (red) and bare $CuWO_4$ (black) single crylstal prepared by Kayla Pyper in 100 mM Na_2SO_4 pH 3 under AM 1.5G 100 mW cm^{-2} illumination at 20 mV s^{-1} using Pt CE and SCE RE

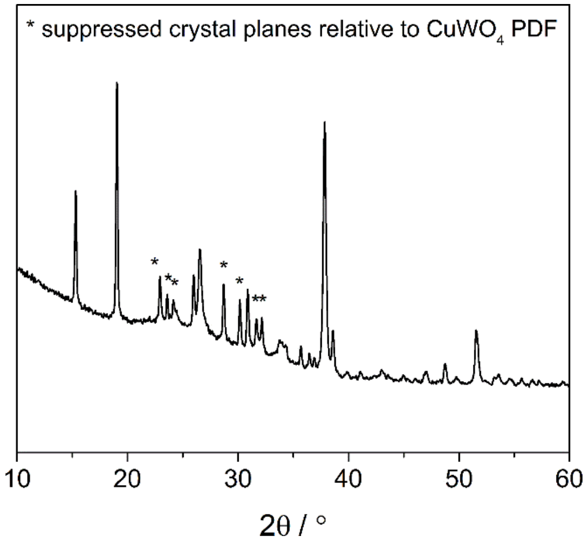

Figure C.16 X-ray diffraction of oriented $CuWO_4$ electrodes fabricated by sol-gel synthesis where the (110), $(0\bar{1}1)$, (011), $(\overline{11}1)$, (111), $(\bar{1}11)$, and $(1\bar{1}1)$ planes are suppressed at increasing 2θ, respectively prepared by James J. Brancho and Christopher Dinh

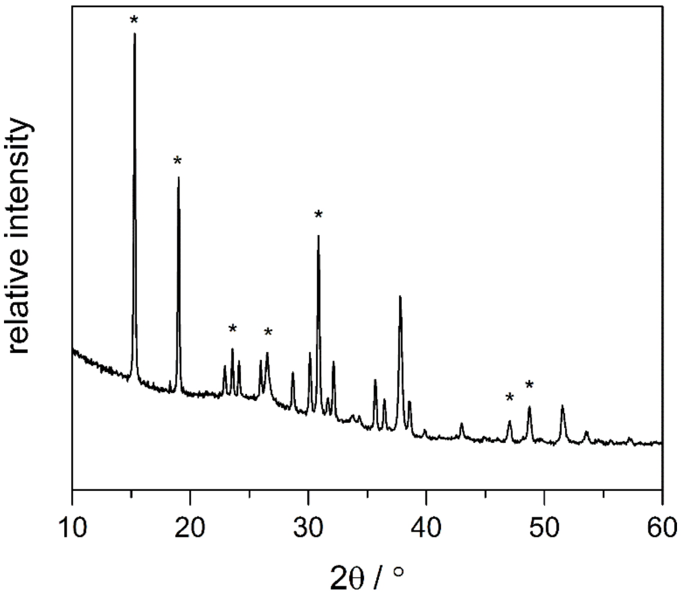

Figure C.17 X-ray diffraction of oriented $CuWO_4$ electrodes fabricated by sol-gel synthesis

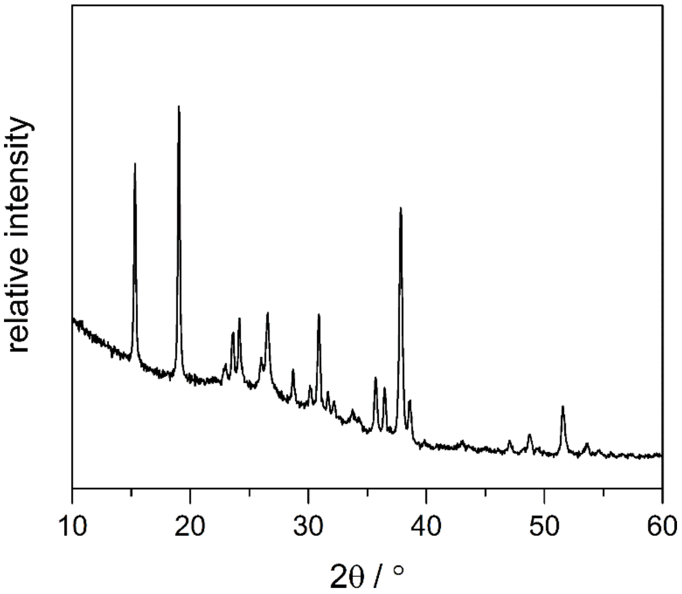

Figure C.18 X-ray diffraction of polycrystalline CuWO4 electrodes fabricated by spray pyrolysis prepared by Charles R. Lhermitte

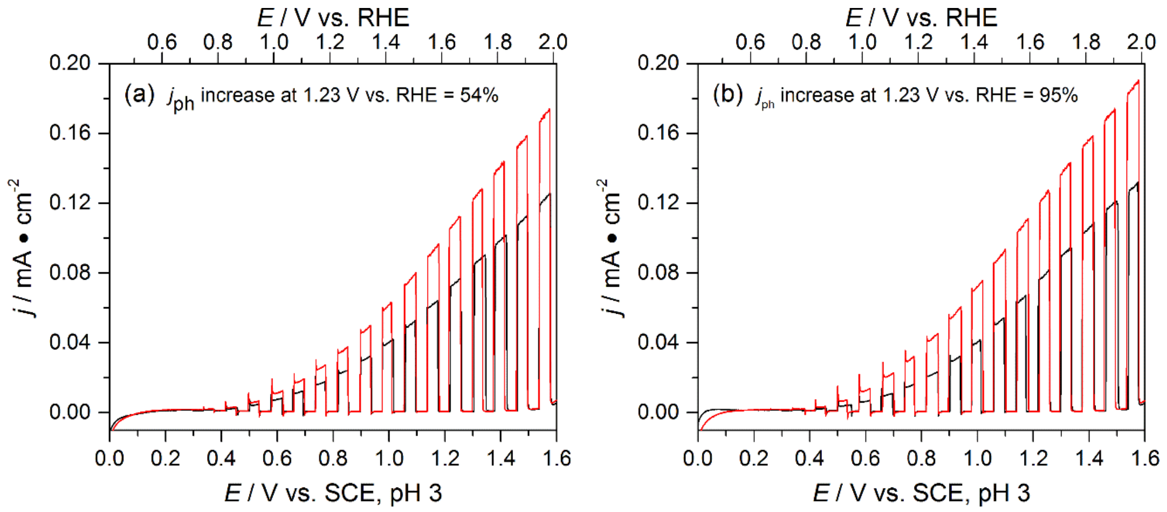

Figure C.19 Front (a) vs. back (b) chopped light illumination of **Fe-2** on $CuWO_4$ (red) or bare $CuWO_4$ (black) in pH 3 100 mM Na_2SO_4 at 20 mV s^{-1} under AM 1.5G 100 mW cm^{-2} illumination using Pt CE and SCE RE

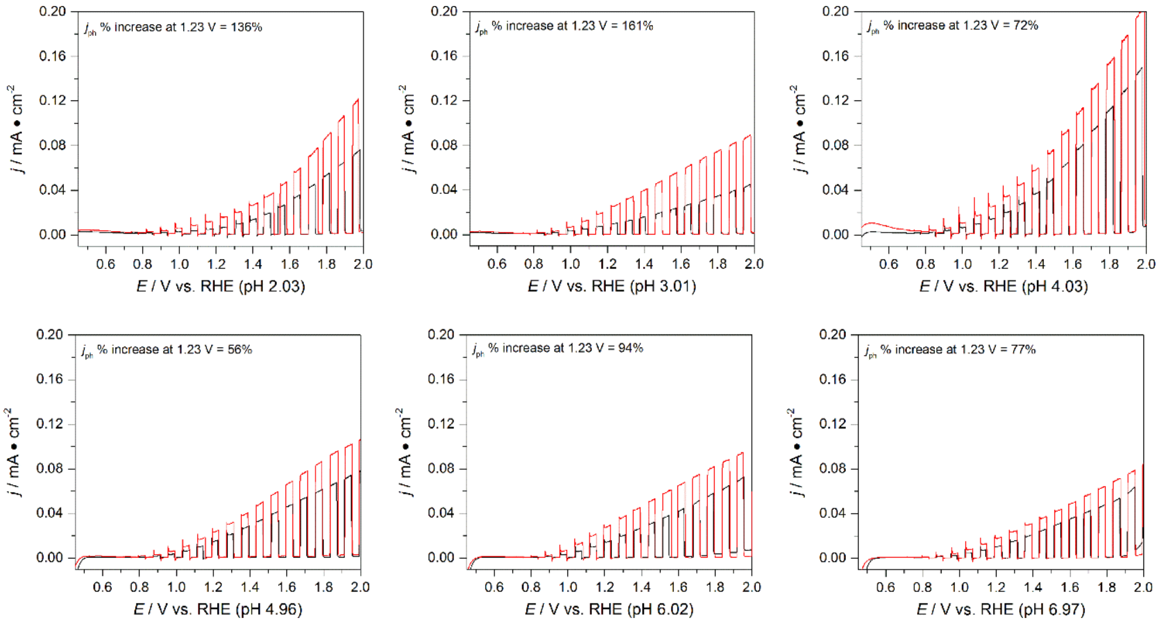

Figure C.20 Chopped light LSV of **Fe-2** on $CuWO_4$ (red) and bare $CuWO_4$ (black) at various pH in 100 mM KP_i buffer under AM 1.5G, 100 mW cm^{-2} illumination at 20 mV s^{-1} using Pt CE and SCE RE

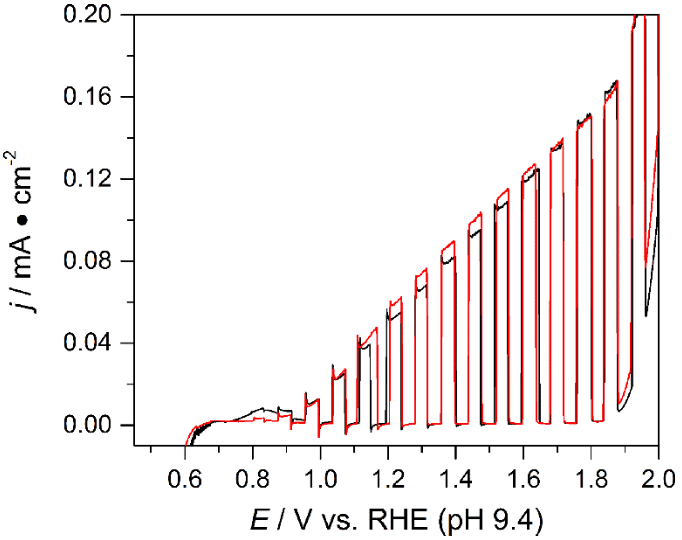

Figure C.21 Chopped light linear sweep voltammogram of **Fe-2** on $CuWO_4$ (red) and bare $CuWO_4$ in 100 mM KB_i pH 9.4 under AM 1.5G 100 mW cm^{-2} illumination at 20 mV s^{-2} using Pt CE and SCE RE

Appendix D

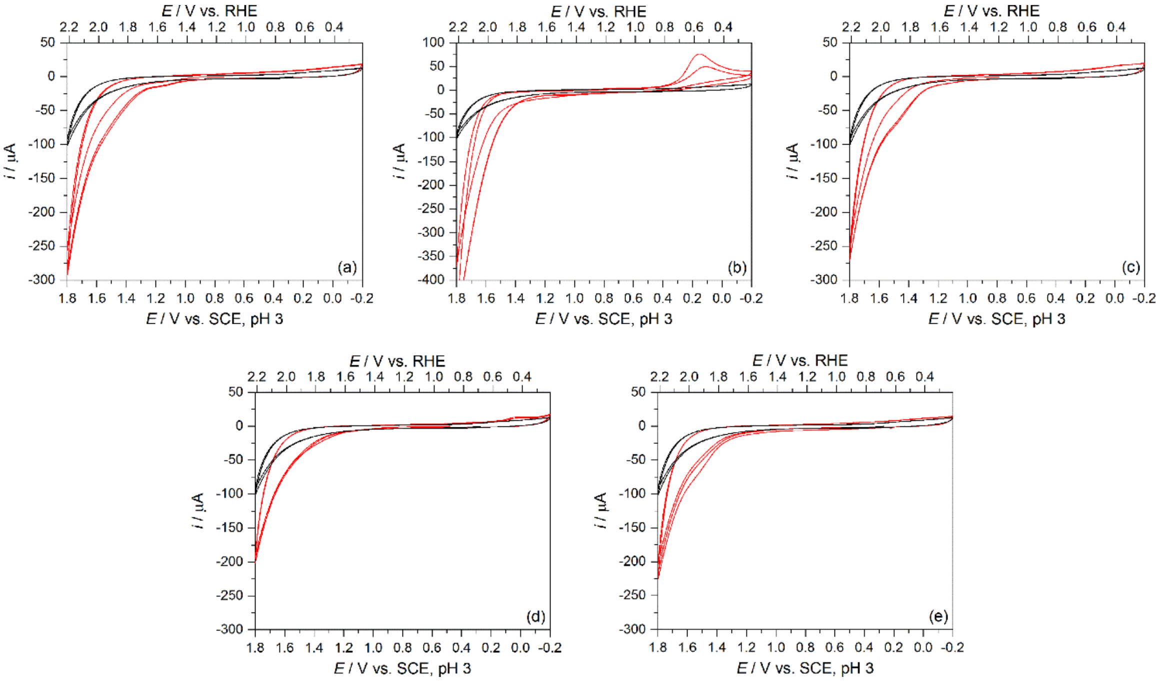

Figure C.1 Solution cyclic voltammograms for **M-3** in 100 mM Na_2SO_4 at pH 3 at 20 mV s^{-1} using GC WE, Pt CE, and SCE RE

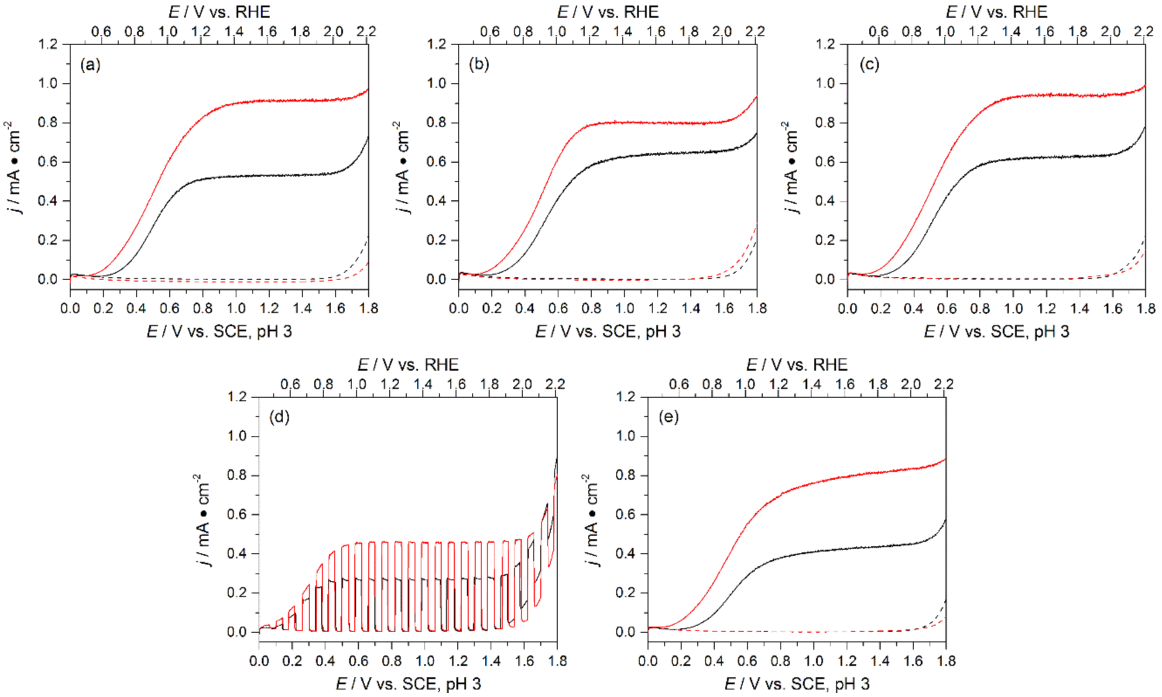

Figure D.2 Linear sweep voltammetry of **M-2** on WO$_3$ (red) compared to bare WO$_3$ (black) under illumination (solid) or in the dark (dashed) in 100 mM Na$_2$SO$_4$ pH 3 under AM 1.5G 100 mW cm^{-2} at 20 mV s^{-1} using Pt CE and SCE RE

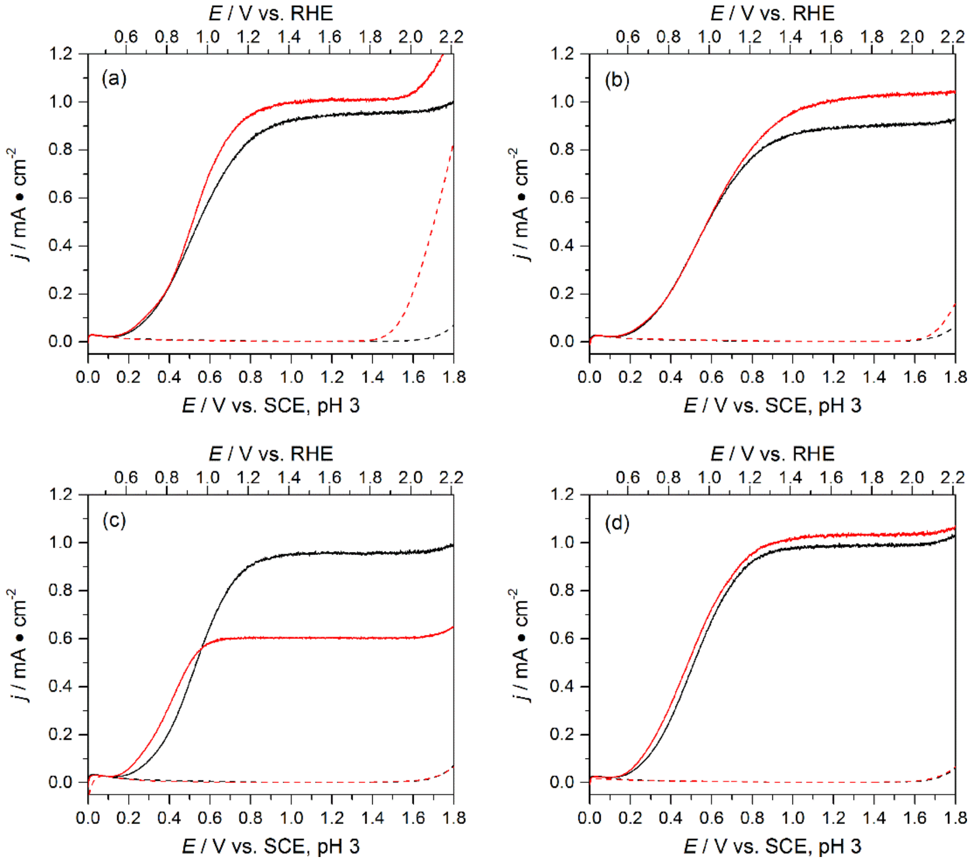

Figure D.3 Linear sweep voltammetry of $CoCl_2$ (a), $NiCl_2$ (b), $CuCl_2$ (c), or $ZnCl_2$ (d) on WO_3 (red) compared to bare WO_3 (black) under illumination (solid) or in the dark (dashed) in 100 mM Na_2SO_4 pH 3 under AM 1.5G 100 mW cm^{-2} at 20 mV s^{-1} using Pt CE and SCE RE